Barocaloric effects in the vicinity of first-order phase transitions

Junning Li

Submitted in partial fulfillment
of the requirements of the Degree of
Doctor of Philosophy

September 2021

School of Physical and Chemical Sciences
Queen Mary University of London

Abstract

Barocaloric effects refer to the adiabatic temperature change (ΔT) or isothermal entropy change (ΔS) of a solid under the application (or removal) of hydrostatic pressure, which are expected to show a great enhancement near a first-order phase transition. Materials with giant or colossal barocaloric effects hold the potential to offer eco-friendly and more efficient alternatives to solid-state heat-pump technologies for replacing hazardous gases used in traditional vapor-compression cooling and heating. However, those effects are often limited by the need for large pressures, small temperature span and by significant hysteresis. The latter feature increases the input work required to drive the cooling cycle reversibly and reduce the temperature range of operation.

In this thesis, I studied the barocaloric effect in materials undergoing order-disorder transition and showing mechanical flexibility, especially on molecular crystal and organic-inorganic hybrid perovskites. I found that a molecular crystal of C_{60} shows giant reversible barocaloric effects at very small pressure changes. I demonstrated that the high sensitivity of the transition to the applied pressure allows for giant reversible barocaloric effects over a very wide temperature range under moderate pressure changes.

Colossal barocaloric effects so far have only been reported in molecular materials with orientational disorder, for example neopentylglycol. I demonstrated that the layered hybrid organic-inorganic perovskite $(C_{10}H_{21}NH_3)_2MnCl_4$ also exhibits colossal effects, but with improved reversibility and performance. By tuning the chemical composition of the organic and inorganic parts, the research offers a path for designing hybrid perovskites with improved barocaloric behaviour.

I analysed the anisotropic lattice deformation in two-dimensional hybrid compounds and then investigated the effect of anisotropy on caloric properties. Further studies indicated a colossal caloric effect can be achieved in the compound by using uniaxial stress along the direction of the *c*-axis. The research presents a new perspective in finding excellent mechanocaloric effects in strong anisotropic materials.

Statement of originality

I, Junning Li, confirm that the research included within this thesis is my own work or that where it has been carried out in collaboration with, or supported by others, that this is duly acknowledged below, and my contribution indicated. Previously published material is also acknowledged below.

I attest that I have exercised reasonable care to ensure that the work is original and does not to the best of my knowledge break any UK law, infringe any third party's copyright or other Intellectual Property Right, or contain any confidential material.

I accept that the College has the right to use plagiarism detection software to check the electronic version of the thesis.

I confirm that this thesis has not been previously submitted for the award of a degree by this or any other university.

The copyright of this thesis rests with the author and no quotation from it or information derived from it may be published without the prior written consent of the author.

Signature: Junning Li

Date: 26/09/2021

Collaboration and copyrights:

The high-pressure experiments included within this thesis were performed at Universitat Politècnica de Catalunya under the direction of Dr. Pol Lloveras. I am very grateful that the X-ray powder diffraction experiments and related data were performed and analysed by Dr. María Barrio at Universitat Politècnica de Catalunya. Dr. Anthony Phillips and Dr. Richard Dixey in the Centre for Condensed Matter and Materials Physics at Queen Mary University of London were also involved in the X-ray data analysis. These data can be found in the Appendix parts. All the other data were analysed and plotted by myself. Data shown in Chapter 4 and 5 has been published (**Chapter 4**: Li, Junning, *et al. "Reversible barocaloric effects over a large temperature span in fullerite C_{60}."* Journal of Materials Chemistry A 8.39 (2020): 20354-20362. DOI: 10.1039/d0ta05399f; **Chapter 5**: Li, Junning, *et al. "Colossal Reversible Barocaloric Effects in Layered Hybrid Perovskite $(C_{10}H_{21}NH_3)_2MnCl_4$ under Low Pressure Near Room Temperature."* Advanced Functional Materials 31.46 (2021): 2105154. DOI: 10.1002/adfm.202105154).

Acknowledgements

It is my honour to accomplish my PhD study in the School of Physics and Astronomy (now School of Physical and Chemical Sciences) at Queen Mary University of London.

I would like to send my special thanks to Dr. Isaac Abrahams and Dr. Paul J. Saines for sparing their valuable time to review and examine my thesis. I appreciate their positive recommendation and helpful suggestions.

I would like to express my sincere thanks to my supervisor, Prof. David J. Dunstan who is a wise and amiable person. During the past four years, David was the most important person in my research career and life who gave me guidance and encouragement. Honestly, I did not do well in our project: the size effect in plasticity. But I really want to say thanks for his patience, support, and encouragement. He is a great man with wonderful personalities and a brilliant mind. We share and discuss our research progresses with a pint of beer every week in SCR bar, which was a wonderful memory in my life. I am honoured that I can be your apprentice (this is the word that David used to explain the different periods of PhD study to me).

I would like to give my heartfelt acknowledgement to Dr. Pol Lloveras who is my co-supervisor at Universitat Politècnica de Catalunya, Spain. Pol is very nice, honest, and patient with me. Although we spent most of our time through the internet, he has

never been impatient and explained every research question to me with long texts. During my stay in Barcelona, Pol taught me how to run the equipment and analysis the data. It was the first time that I had a chance to work with the world's leading group on barocaloric effect. Speaking to this group, I would also like to say thanks to Prof. Josep Tamarit, Prof. Lluís Mañosa, and Dr. Maria Barrio for their kind help in my study and stay in Barcelona. What I have learned from you means a lot to me.

I would like to say thanks to Dr. Yiwei Sun for his kind help and practical advice in my study and future career. I would also like to thank Dr. Anthony Phillips, Dr. Ken Scott, and Dr. Richard Dixey for their help in my experiment and data analysis. I would like to acknowledge members of our group and office. I thank to Dr. Dominic Carter, Dr. Dabiao Liu, Dr. Guanqun Cai, Haowei Zhang, Dr. Fei Xie, Dr. Linfeng Li, Fei Peng, Shurong Yuan, Dr. Mark Wilkinson, Dr. Lei Wang and Dr. Zhichao Weng for their help in my study and daily life. It was really a pleasure time to study and play with them.

My great appreciation should be given to my father, mother and brother for their support and encouragement. I love you. A big and warm welcome to my niece or nephew who will come to the world soon. I love you so much. I wish to express my gratitude to my girlfriend, Xiao Liu who is now studying communication design at the Glasgow School of Art. It is lucky for me that I can finish my PhD study with your company. I feel happy and comfortable to have you with me every day. Thanks for your smile, support, and cooking. By the way, I have no doubts that you will be a great graphic designer. I love you from my deep heart.

Finally, I wish a wonderful life for all of you.

Contents

List of Abbreviations

2D	Two-dimensional
3D	Three-dimensional
AMP	Active Magnetic Regeneration
BC	Barocaloric
c	Heat capacity
CRP	Coefficient of Refrigeration Performance
DSC	Differential Scanning Calorimetry
E	Electric field
eC	Elastocaloric
EC	Electrocaloric
F	Helmoltz free energy
fcc	Face-centered cubic structure
G	Gibbs free energy, or gauche conformation
H	Magnetic field, or Enthalpy
HOIPs	Hybrid Organic-Inorganic Perovskites
HPDTA	High-Pressure Differential Thermal Analysis
IR	Infrared
k	Optical mode in Raman analysis
LAM	Longitudinal acoustic mode
m	Mass
MC	Magnetocaloric
mC	Mechanocaloric
p	Pressure

Q	Heat
R	Thermal resistance of a medium
RC	Refrigerant capacity
S	Entropy
sc	Primitive cubic structure
T	Temperature, or trans conformation
T_t	Phase transition temperature
t	Time
TC	Twistocaloric
U	Internal energy
V	Volume, or Voltage
W	Work
XRPD	X-Ray Powder Diffraction
α	Thermal expansion
ΔH	Enthalpy change at the first-order transition (latent heat)
ΔS	Isothermal entropy change
ΔS_{rev}	Reversible isothermal entropy change
ΔS_t	Transition entropy change
ΔT	Adiabatic temperature change
ΔT_{rev}	Reversible adiabatic temperature change
ΔV_t	Volume change at the first-order transition
ε	Strain
η	Efficiency
θ	Scattering angle in XRD measuring
ρ	Density
σ	Stress

Chapter 1

Introduction

Refrigeration plays a significant role in space cooling, food storage and transportation, industrial freezers, cryogenics and so on. Today, about 5 billion refrigeration, air-conditioning and heat pump systems are in operation, and these account for about 20% of global electricity consumption which is estimated to more than double by 2050 [1]. Vapor-compression technology using hydrofluorocarbons is employed in the vast majority of those systems. However, the energy efficiencies of vapor-compression cooling systems for household applications are relatively low, with an average of 20% based on the Carnot cycle [2]. Although the energy efficiencies are high for large-scale appliances or highly refined systems, they tend to approach their theoretical efficiency limit [3]. Another major issue is the environmental impact of CO_2 emissions originating from the electricity production and direct leakage of fluorinated refrigerants, which contribute 10% of the total greenhouse gas emission [4]. The hydrofluorocarbon fluids have global warming potential up to thousands of times greater than that of CO_2 [4]. Hence, there has been a search for high-efficiency alternative cooling technology which is desired to be economical and environmentally friendly.

In the past few decades, alternative cooling methods based on solid-state caloric effects have received great research attention due to their higher cooling efficiencies and the use of non-harmful materials [5-11]. In principle, solid-state caloric effects are defined as the adiabatic temperature or isothermal entropy changes of solid-state materials through the application of external fields. One can technically achieve cooling and heating by employing the temperature and entropy changes in controlled cycles. Up to now, several caloric effects have been widely investigated, which include the magnetocaloric effect induced by a magnetic field, or the electrocaloric effect obtained by applying an electric field, or the mechanocaloric effect with the stimulus of mechanical force or the multicaloric effect realized through the application of two or more fields. Importantly, enhanced caloric effects can be found at first-order phase transitions due to the field-driven transition latent heat [5]. In achieving magnetocaloric and electrocaloric effects, one needs to change the magnetization and polarization states of specific materials through the application of magnetic or electric fields respectively. Therefore, these effects so far have only been reported in magnetic and ferroelectric materials respectively [5]. In contrast, mechanically driven caloric effects [7-10] have been investigated in many materials, for example metal alloys, polymers, inorganic compounds, and inorganic-organic hybrids. Depending on the different types of external stress, mechanocaloric effects can be classified as uniaxial strain-driven or stress-driven (elastocaloric) effects, hydrostatic pressure-driven (barocaloric) effects and shear strain-driven (twistocaloric) effects. However, in practice, the elastocaloric and twistocaloric effects show specific requirements on the shape of the materials which

must be bulk, wire or thin film. By contrast, barocaloric effects have been extensively studied in numerous materials, in powder or bulk forms [9].

As for barocaloric materials, remarkable effects were first reported in pressure-driven magnetic or martensitic phase transitions in magnetostructural alloys [12-16] mainly thanks to the previous studies on magnetocaloric and elastocaloric effects in these materials. Recently, intensive studies have been performed on materials displaying strong order–disorder phase transitions. Compared to traditional magnetic materials, the disordering process can lead to enhanced entropy and temperature changes, and therefore improved barocaloric behaviour [10]. Giant barocaloric effects have been discovered in inorganic ferroelectrics [17,18] and organic-inorganic hybrid perovskites [19-21] showing orientational disorder transitions, and in solid electrolytes [22,23] with occupational disorder transitions. As a kind of material showing very strong molecular orientational disorder, barocaloric effects in plastic crystals[1] or molecular crystals were subsequently investigated. The results indicated that plastic crystals shown the largest caloric effects among all caloric materials so far [24,25]. For instance, the colossal[2] barocaloric effects in commercially available samples of the plastic crystal neopentylglycol, 2,2-dymethyl-1,3-propanediol, are comparable to current standard commercial hydrofluorocarbon refrigerant R134a [26].

[1]Plastic crystals refer to a kind of orientation- or conformation-disordered material. The term "plastic" refers to the mechanical softness property of these materials.

[2]Before colossal barocaloric effects were found, barocaloric effects with entropy changes of dozens of joules per kilogram per Kelvin were called giant effects. Therefore, colossal effects refer to hundreds of joules per kilogram per Kelvin.

However, some/many of these materials exhibit considerable transition hysteresis which can dramatically reduce the operation temperature range [27]. In practice, a large thermal hysteresis requires a large pressure to drive a reversible thermal change and entropy change, which means it needs more input work and therefore decreases the cooling efficiency as well [27-29]. While some strategies have been made in tailoring hysteresis in specific cases [30,31], solid-state caloric material actually showing a relatively small thermal hysteresis are sought and favoured for practical cooling.

Therefore, the main research questions that motivated this PhD work are:

1) Barocaloric effects in plastic crystals provide researchers with a way to explore effects in orientational order-disorder transitions but this is accompanied by a large thermal hysteresis. It is of great interest to find molecular crystals with small hysteresis.
2) Colossal barocaloric effects so far have only been reported in plastic crystals. Are there any other materials showing colossal barocaloric effects? Can we find a kind of material with colossal effects but displaying different phase transition types?

To answer these questions, I have designed and performed the following experiments during my PhD research studies.

1.1 Outline of the thesis

Chapter 2, *Fundamentals of barocaloric effects*, firstly present a brief summary of the history of solid-state caloric effects and their cooling prototypes. Then, the following

parts introduce a physical analysis of barocaloric effects and phase transitions. The impact of thermal hysteresis is discussed. The measurement methods and parameters for barocaloric characterization are finally summarized.

Chapter 3, *Experimental methods*, shows the thermal characterization and data analysis methods mainly used in this thesis at ambient and high pressure. The key issue for this chapter is the establishment of quasidirect method based on the heat flux measured at different pressures.

Chapter 4, *Barocaloric effects in fullerite C_{60}*, introduces the history and structure of C_{60} firstly. Then, a motivation based on Question 1 is well described. By analyzing its structural and thermodynamic properties at atmospheric pressure and high pressure, barocaloric performances of C_{60} crystal are well described.

Chapter 5, *Barocaloric effects in the layered hybrid perovskite $(C_{10}H_{21}NH_3)_2MnCl_4$*, analyses the advantages of the hybrid organic-inorganic compounds as barocaloric materials and presents the main research idea related to Question 2. Then, barocaloric effects of this material and its phase transition properties are well studied through the use of thermodynamic data at atmospheric pressure and high pressure.

Chapter 6, *Comparison and future prospects*, summarizes and compares the barocaloric properties of different compounds by introducing the Coefficient of Refrigeration Performance. Then this chapter presents the possible ways to find excellent barocaloric effects in similar layered materials.

Chapter 7, *The effect of anisotropy on caloric properties in two-dimensional hybrid organic-inorganic perovskite*, exhibits extended research on layered hybrid perovskites. In doing the barocaloric analysis of $(C_{10}H_{21}NH_3)_2MnCl_4$, a strong anisotropy effect in

the *c*-axis is observed and then a colossal elastocaloric is theoretically obtained. The evaluation of this effect is discussed, and an experimental proposal is followed.

Chapter 8, *Conclusion and perspectives*, summarizes the main conclusion of this thesis and provides perspectives for further studies.

Chapter 2

Fundamentals of barocaloric effects

In this chapter, I present a broad introduction on solid-state caloric effects which includes the achievements in the history of caloric effects, a comprehensive comparison of different caloric cooling methods, and their current refrigeration prototypes. Then, I will focus on the barocaloric effect and its fundamentals. From the thermodynamic point of view, the physical description of the barocaloric effect and its relationship with a phase transition is presented. Importantly, the influence of thermal hysteresis is also discussed through the analysis of *S*-*T* diagrams. Finally, I will introduce the measurement methods of barocaloric effects and the parameters to characterize these effects.

2.1 Solid-state caloric effects

2.1.1 Brief introduction to caloric effects

Figure 2.1 shows the timeline of the history of solid-state caloric effects, and briefly summarizes the important events from 1805 to 2020. For better illustration, representative works on caloric effects and their cooling prototypes are presented. The definition

of solid-state caloric effects has been generally introduced in the introduction part. Basically, these effects refer to the capability of changing the thermal or thermodynamic state of a solid-state material by doing work. The first experimental observation of caloric effects with documentation was the elastocaloric effect in India rubber, which was reported by natural philosopher John Gough in 1805 [32]. A thermodynamic interpretation about this effect was introduced by Lord Kelvin in his article *On the Thermoelastic, Thermomagnetic, and Pyroelectric Properties of Matter* in 1855 [33]. In this paper, he not only considered the thermodynamics of the elastocaloric effect but also predicted magnetocaloric and electrocaloric effects driven by magnetic and electric fields, respectively. Elastocaloric effects in some metals and dry woods were then published by James Prescot Joule in 1859 which led him to think about the relations between heat and mechanical work [34]. The discovery of magnetocaloric effect is controversial, and has been re-examined and argued by Anders Smith [35]. It is believed that the magnetocaloric effect was firstly discovered in nickel by Pierre Weiss and Auguste Piccard in 1917 [36] rather than by Emil Warburg in 1881 [37]. In 1930, the electrocaloric effect was firstly found in Rochelle salt, $KNaC_4H_4O_6{\cdot}4H_2O$ by P. Kobeko and J. Kurtschatov [38]. As for the barocaloric effect, it was first defined and experimentally examined by Alex Müller in $Pr_{1-x}La_xNiO_3$ compounds in 1998 [39]. The last and also the youngest member of caloric effects called the twistocaloric effect was first reported by Wang Run in natural rubber, polyethylene and nickel-titanium fibers in 2019 [40]. In addition to the above effects, the concept of multicaloric effects was theoretically described by Melvin Vopson in multiferroic the material $NdCrTiO_5$ [41], in which adiabatic temperature and isothermal entropy changes can be achieved

by applying electric or magnetic fields. This concept was later extended to any materials that exhibit caloric responses under two or more external fields [42].

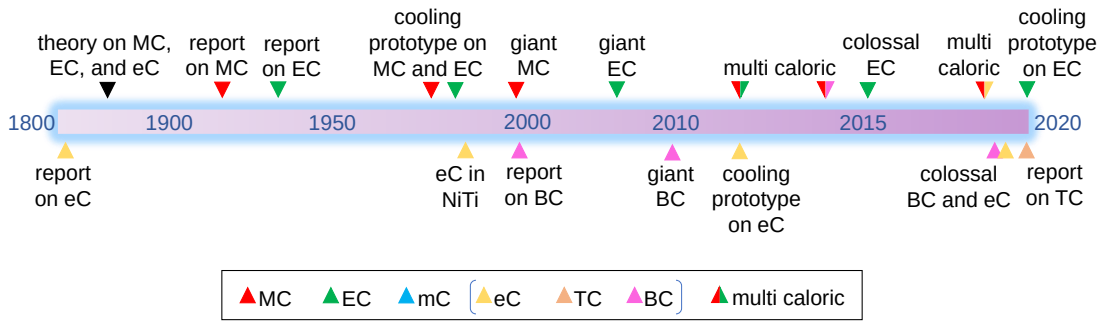

Figure 2.1. A simple timeline of events in the history of solid-state caloric effects from 1805 to 2020. MC: magnetocaloric effect, EC: electrocaloric effect, mC: mechanocaloric effect, eC: elastocaloric effect, TC: twistocaloric effect, and BC: barocaloric effect.

In Table 2.1, I have listed solid-state caloric materials that show excellent caloric effects under different external fields. In general, by comparing the adiabatic temperature and isothermal entropy changes, the magnetocaloric and electrocaloric are smaller than mechanocaloric effects. This is because their caloric responses highly rely on the changes of magnetic and polar states under applied fields. For example, under a magnetic field change of 2 T, $LaFe_{11.74}Co_{0.13}Si_{1.13}$ shows giant reversible entropy and temperature changes of 20 J $K^{-1}kg^{-1}$ and 6 K, respectively [45]. Magnetocaloric materials, for example $Gd_3Ga_5O_{12}$, have higher performance at cryogenic temperatures, where use of higher applied magnetic fields becomes more practical [6]. Although a large effect can be achieved under a higher field, it is hard to apply a magnetic field larger than 2 T practically. However, the magnetocaloric effect has been the most studi-

ed of the caloric effects over the last few decades. In practice, magnetocaloric cooling methods have been examined within more than 60 prototypes which show high efficiencies and little noise [6]. And they have shown great success in cryogenic applications [6]. In addition, the successful study and application of the magnetocaloric effect also provide a reference for other caloric effects, which includes the study of their thermodynamics and exploring of cooling prototypes.

The electrocaloric effect in ferroelectrics has attracted great research attention since a giant effect (ΔT_{ad} = 12 K) was found in $PbZr_{0.95}Ti_{0.05}O_3$ thin films in 2006 [48]. Two years later, a large effect of 12 K was reported in PVDF-based organic ferroelectrics [49]. After that, giant or even colossal electrocaloric effects have been intensively reported in inorganic, organic and organic-inorganic composites in the form of thin films [61]. These outstanding findings make electrocaloric films promising candidates for practical on-chip cooling and heating. Very recently, researchers have created two electrocaloric refrigeration prototypes [62,63] based on $PbSc_{0.5}Ta_{0.5}O_3$ multi-layered ceramics after a large temperature change of 5.5 K was recorded [51]. This could lead to the realization of electrocaloric refrigeration in large devices.

Elastocaloric effects with very large temperature changes have been identified in shape-memory alloys, crosslinked elastomeric polymers, and ferroelectrics [64-66]. These materials are considered to be entropy-elastic compounds, in which elastic deformation is highly related to the change in the lattice structure of the material [66]. In particular, shape-memory alloys have been intensively investigated since a temperature change of 14 K was first measured in $Ni_{50.7}Ti_{49.3}$ alloys in 2004 [67]. Thanks to the

excellent caloric effects reported in these alloys, cooling prototypes based on elastocaloric effects have been widely studied and proposed for practical use [5]. Recently, a colossal elastocaloric effect with a temperature change of 31.5 K has been reported in bulk polycrystalline $(Ni_{50}Mn_{31.5}Ti_{18.5})_{99.8}B_{0.2}$ [55], which make the elastocaloric cooling more prominent among solid-state caloric effects. As a new member of the caloric family, the twistocaloric effect or torsiocaloric effect, which is cooling of a fiber on changing the twist of a wire or fiber, was demonstrated in $Ni_{48.9}Ti_{51.1}$ wire with a temperature change of 17 K [40]. However, it is to be noted that thermal effects in twisted wires are nonhomogeneous which means there is a thermal gradient from the surface to the centre. Thus, to achieve large cooling efficiency, a specific design should be employed.

Despite the significant progress on solid-state caloric effects, many challenges and questions still remain. For example, magnetocaloric materials contain rare-earth elements which are expensive and inappropriate for large-scale, long-term commercial projects [6]. Normally, the magnetic fields created by permanent magnets are rather low, with a maximum value of 2 T [7]. Although organic ferroelectrics and their composites show excellent properties, their low thermal conductivities and thin-film form are unsuitable for more efficient and large-scale cooling [68]. Excellent electrocaloric effects have been obtained in bulk materials, but most of them are lead-based which are harmful to humans and the environment. Another issue for electrocaloric materials is the electric breakdown under high fields. Elastocaloric effects are mainly investigated in shape memory alloys and elastomeric polymers [66]. The biggest problem in these materials is their mechanical fatigue under intensive loading and unloading. Act-

ually, fatigue is also a big challenge for all caloric materials, especially for materials with first-order phase transitions. It is to be noted that low temperature magnetocalorics are likely an exception to this as their more gradual transformations from paramagnets to field correlated ferromagnets likely reduces this significantly compared to the first-order phase transition needed for other caloric materials, including higher temperature magnetocaloric materials. An effective and durable cooling device requires a continuously high performance after millions of cycles under high external fields [9]. Barocaloric cooling can avoid the mechanical or electrical breakdown in caloric materials by using material in the form of powder [9].

Finally, as it has been summarized in Refs. 9 and 10, the barocaloric effect has been investigated in many materials within various phase transitions. Interestingly, one can see that about 50% of these materials were discovered in the last three years. Obviously, this indicates the great potential and fast growth of barocaloric studies.

Table 2.1. Caloric properties of representative materials.

Caloric effects	T_t[a] (K)	$\|\Delta T_{ad}\|$[b] (K)	$\|\Delta S_{iso}\|$[c] (J K^{-1} kg^{-1})	ΔT_{hyst}[d] (K)	Applied Fields[e]	Refs.
MC effects					T	
Gd	292	4.7	5.2	*non-*[f]	2	43
$Gd_5Si_2Ge_2$	262	4.9	18.4	5	2	44
$LaFe_{11.74}Co_{0.13}Si_{1.13}$	197	6.7	20.3	1	2	45
$Fe_{49}Rh_{51}$	317	6.2	13.2	7.1	2	46
$Ni_{50.2}Mn_{35.0}In_{14.8}$	301	1.2	15	3.6	2	47
EC effects					kV cm^{-1}	
$PbZr_{0.95}Ti_{0.05}O_3$	495	12	8	*non-*	480	48
P(*VDF-TrFE*)	343	12	55	*non-*	2090	49
$BaTiO_3$	402	0.9	2.2	2	12	50
$PbSc_{0.5}Ta_{0.5}O_3$	290	5.5	6	4	290	51
Polymer composites[g]	303	16.5	70	*non-*	750	52
eC effects					MPa	
$Ni_{48.9}Ti_{51.1}$	330	25	35	1	900	53
$Ti_{50}Ni_{44}Cu_5Al_1$	300	25	53.5	9	600	54
$(Ni_{50}Mn_{31.5}Ti_{18.5})_{99.8}B_{0.2}$	308	31.5	45	25	700	55
Polyurethane[h]	282	5	60	--[i]	8	56
Natural rubber	283[j]	12	44	--	1	57
BC effects					MPa	
$Ni_{50}Mn_{31.5}Ti_{18.5}$	243	8	74	18	400	58
$(NH_4)_2SO_4$	219	8	60	6	100	17
AgI	390	18	60	25	250	20
[*TPrA*]Mn[*dca*]$_3$[k]	330	5	37	1	7	23
$(CH_3)_2C(CH_2OH)_2$	315	8	420	10	200	24, 25
Fe_3(*bntrz*)$_6$(*tcnset*)$_6$[l]	318	35	120	1	260	59
TC effects					MPa	
$Ni_{48.9}Ti_{51.1}$	268	17	35.1	5	650	40

[a] T_t refers to the phase transition temperature without external fields. [b] $|\Delta T_{ad}|$ indicates the absolute value of adiabatic temperature changes. [c] $|\Delta S_{iso}|$ represents the absolute value of isothermal entropy change. [d] ΔT_{hyst} means the thermal hysteresis of the phase transitions. [e] Applied fields includes applied magnetic and electric fields as well as applied pressure depending on the specific solid-state caloric effects. [f] "*non-*" stands for non-hysteresis. In other words, those materials that undergo second-order phase transitions. [g] Polymer composites: P(VDF-TrFE-CFE) polymers mixed with $BaZr_{0.21}Ti_{0.79}O_3$ nanofibers embedded with $BiFeO_3$ nanoparticles. [h] refers to thermoplastic polyurethane. [i] "--" means no data records. [j] this is the temperature for caloric tests, not the transition temperature. [k] *TPrA*: tetrapropylammonium, *dca*: dicyanamide. [l] *bntrz*: 4-(benzyl)-1,2,4-triazole, *tcnset*: 1,1,3,3-tetracyano-2-thioethylepropenide.

2.1.2 Thermodynamic cooling cycles and prototypes

Thermodynamic cooling cycle plays a key role in both theoretical and experimental studies of the refrigeration performances in caloric based prototypes. Generally, a cooling prototype includes not only the caloric materials and field generator but also the heat exchange and transfer system. With these components, a complete cooling cycle can be realized through the prototype [69,70]. In Figure 2.2, I schematically show two ideal thermodynamic refrigeration cycles (Carnot and Brayton cycles) in terms of entropy (S) vs temperature (T) plots [69,70].

The Carnot cycle includes two isentropic (adiabatic) processes and two isothermal steps [see Figure 2.2 (a)]. Practically, a Carnot refrigeration cycle shows a low cooling capacity and is usually used in the low temperature range, which limits its application in cooling devices [70]. Therefore, this type of cycle is more preferred in a theoretical study when comparing with the other refrigeration cycles [69]. In contrast, Brayton cycles have been employed in many real devices, and consist of two isentropic processes and two isofield steps [see Figure 2.2 (b)]. Thermodynamically, Brayton cooling cycles can be described as follows: stage A to B, adiabatic application of an external field and consequent heating of the caloric material; stage B to C, cooling of caloric material under a constant field; stage C to D, adiabatic removal of an external stimulus and consequent cooling of the caloric material; stage D to A, heating of the caloric material under a constant field.

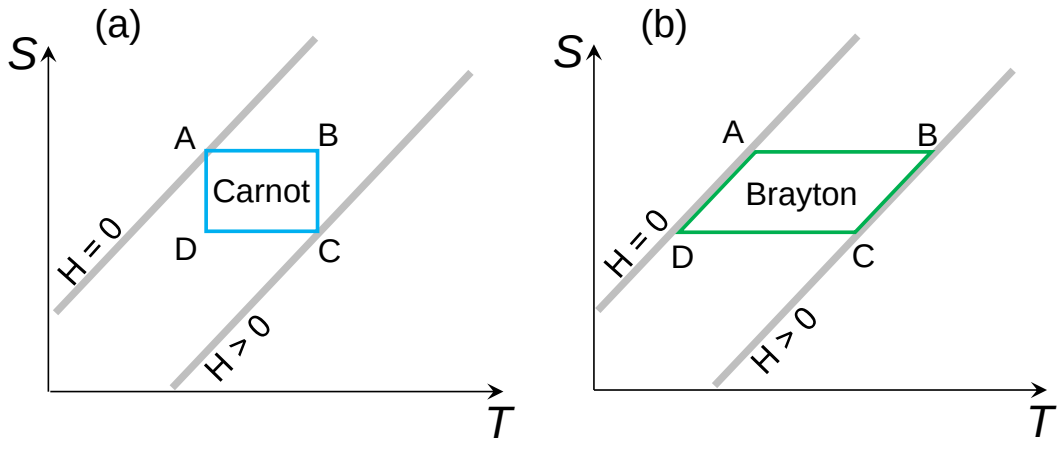

Figure 2.2. The schematics of (a) Carnot and (b) Brayton refrigeration cycles in *S*-*T* diagrams. The isofield entropy are plotted in grey colour. *H* refers to the magnetic field.

Cooling prototypes based on solid-state caloric effects have been well summarized in Ref. 71. In order to illustrate the refrigeration procedures and principles, a magnetocaloric cooling prototype, active magnetic regeneration (AMR) was introduced as a study case. Figure 2.3 presents a Brayton-type refrigeration cycle in a modified AMR which was designed by Arnold in 2014 [72]. During the adiabatic application of magnetic field ($H > 0$), the magnetocaloric material shows a temperature increase thanks to the conventional magnetocaloric effect. Then, the working fluid leaves the heat source heat exchanger (blue part) and exchanges heat with magnetocaloric material (cooling of the material). After that, the working fluid enters the heat sink heat exchanger (orange part) and transfers the heat to the external environment. When the fluid is cooled by the environment, it will leave the heat sink heat exchanger and exchange heat with the magnetocaloric material again. However, the material now shows a temperature

reduction due to the removal of the magnetic field and then the fluid is cooled (heating of the material). This cooled fluid can be used as a cooling source.

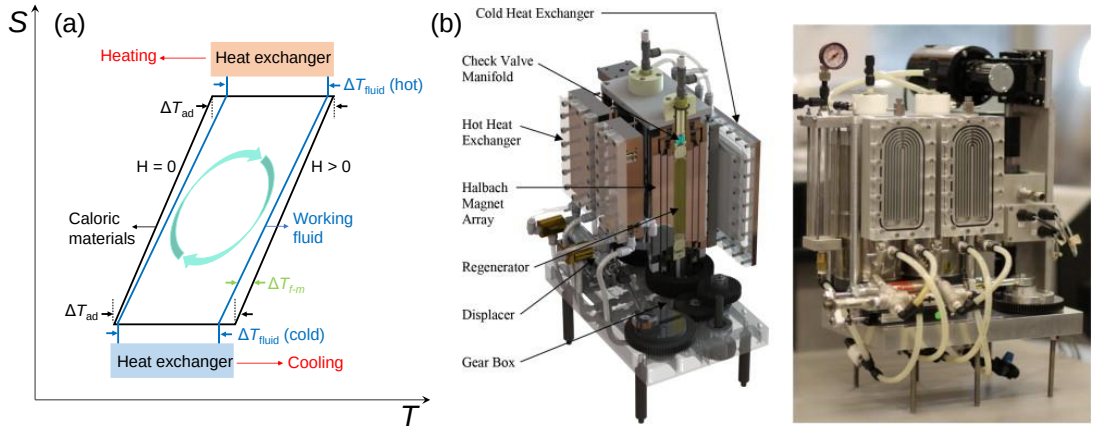

Figure 2.3. (a) A schematic Brayton cooling cycle of an active magnetic regeneration (AMR) in a *S*-*T* diagram and (b) Picture of a modified AMR device (reproduced from Ref. 72).

It is to be noted that the above discussions are mainly described under ideal conditions. In addition to the Carnot and Brayton cycles, regenerative cycles like Ericsson, Stirling, and hybrid Brayton-Ericsson have also been introduced and used in cooling prototypes [69]. These are only mentioned here and will not be discussed further.

2.2 Thermodynamics of barocaloric effects

In general, according to the first law of thermodynamics, the differential change of internal energy dU in a crystal can be expressed as

$$dU = dW + dQ, \tag{2.1}$$

where dW is the work, and $dQ = TdS$ in a reversible process. Here, T is the temperature and S is the entropy of the system.

As for a system under the influence of hydrostatic pressure p and volume V [72, 73], where the magnetic (H), electric (E) fields are constants, Equation (2.1) can be written as

$$dU\ (S,V)_{(H,E)} = -pdV + TdS. \tag{2.2}$$

In practice, thermodynamic changes are induced by controlling temperature and hydrostatic pressure [74]. Therefore, by using Legendre transforms, the Helmholtz and Gibbs free energies can be expressed as $F = U - TS$ and $G = F - (-pV) = U - TS + pV$, respectively.

Then, the differential change of Gibbs free energy associated with differential changes of temperature T and pressure p is given by

$$dG = -SdT + Vdp, \tag{2.3}$$

and, the entropy S and volume V are expressed as

$$S = -\left(\frac{\partial G}{\partial T}\right)_p, \tag{2.4}$$

$$V = \left(\frac{\partial G}{\partial p}\right)_T. \tag{2.5}$$

Through Equation (2.4), we can firstly define the heat capacity c at constant pressure p as

$$-\left(\frac{\partial^2 G}{\partial T^2}\right)_p = \left(\frac{\partial S}{\partial T}\right)_p = \frac{c}{T}. \tag{2.6}$$

Similarly, using Equations (2.4) and (2.5), the Maxwell relation can be derived in terms of (S, T) and (V, p)

$$-\left(\frac{\partial^2 G}{\partial p \partial T}\right)_{(H,E)} = -\left(\frac{\partial V}{\partial T}\right)_p = \left(\frac{\partial S}{\partial p}\right)_T. \quad (2.7)$$

As for barocaloric effects, the pressure-induced isothermal change of entropy can be obtained from integration of the appropriate Maxwell Equation (2.7),

$$\Delta S(T, 0 \rightarrow p) = S(T, p) - S(T, 0) = -\int_0^p \left(\frac{\partial V}{\partial T}\right)_p dp. \quad (2.8)$$

Under adiabatic condition, *S* is constant. Considering Equations (2.6) and (2.7), integration of $dS = 0 = \frac{C}{T} dT - \left(\frac{\partial V}{\partial T}\right)_p dp$, yields,

$$\Delta T(0 \rightarrow p) = T(S, p) - T(S, 0) = \int_0^p \frac{T}{C}\left(\frac{\partial V}{\partial T}\right)_p dp. \quad (2.9)$$

From Equations (2.8) and (2.9), we can see that an enhanced barocaloric effect can be found in materials with a strong temperature-induced volume change. It is to be noted that the value of temperature dependence of the volume is large near the phase transition. Actually, this is the main reason why remarkable barocaloric effects are observed in the vicinity of phase transitions [5,7,69,70]. To illustrate this, phase transitions are classified into first-order and second-order transitions considering the order of the differential of the Gibbs free enthalpy ($G = U - TS + pV$) model. This classification of the phase transitions is due to Paul Ehrenfest [73]. In first-order phase transitions [Figure 2.4 (a)], there is a kink in the free enthalpy of the system at the transition point which is under equilibrium conditions. The kink in free enthalpy corresponds to a discontinuity in its first derivatives at the transition point (See Figure 2.4(b)). For second-order phase transitions, the first-order derivative of the free enthalpy is continuous, and the second-order derivative of the enthalpy is discontinuous. The latent heat is the main feature of first-order transitions. In the case of second-order

transitions, there is no latent heat and therefore no sharp change in the entropy at the transition. However, the slope of the curve changes abruptly.

It is worth noting that these features are related, because the discontinuity in the derivative of G arises due to the existence of different branches, one for each phase, and these branches exist beyond the stable regimes as metastable minima of G. This metastability is the origin for the hysteresis. All these features are lacking in the case of second-order phase transitions.

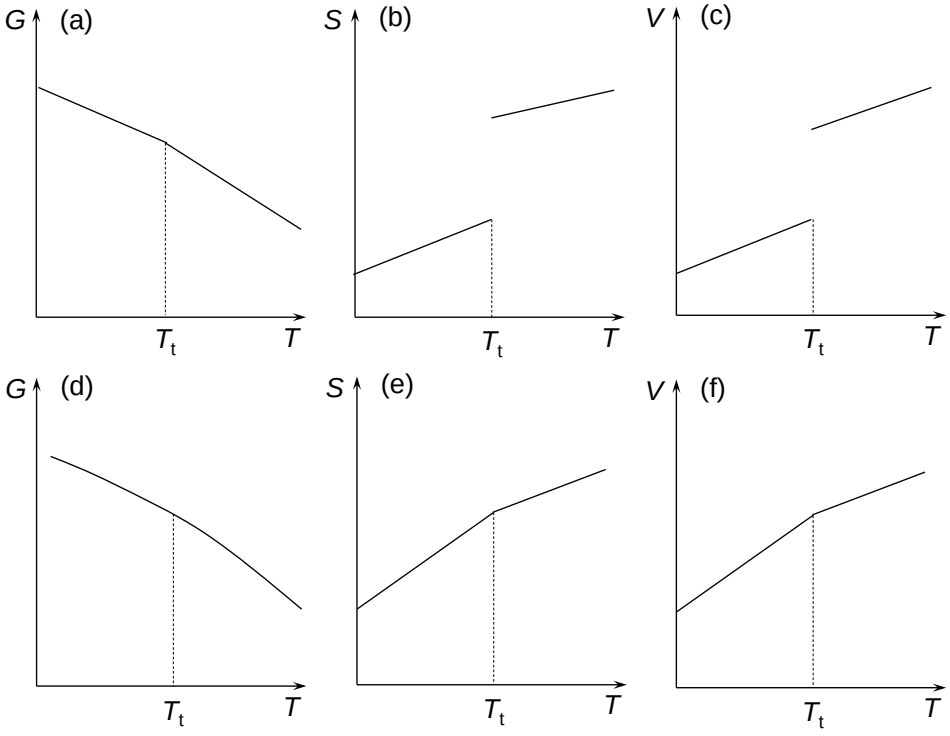

Figure 2.4. Sketches of thermodynamic properties in first-order (top panels) and second-order (bottom panels) phase transitions. The temperature dependence of the Gibbs free energy (a) and (d), the entropy (b) and (e), and the volume (c) and (f) at constant pressure. T_t corresponds to the phase transition temperature and indicates a change in the slope.

As can be seen from Figure 2.4, barocaloric effects near first-order phase transitions are much larger than the effects in second-order transitions. This is because the volume change with temperature in first-order transitions is anomalous (discontinuous), whereas this change is continuous with temperature when a second-order transition occurs [70,73]. So far, giant and colossal barocaloric effects have only been reported in materials with strong first-order phase transitions. However, the thermal hysteresis arises due to the discontinuous nature of first-order phase transitions which is detrimental for the barocaloric effect and will be discussed in detail in section 2.4.

2.3 Barocaloric effects in first-order phase transitions

Thermodynamic analysis based on Maxwell relations has been widely accepted and employed in dealing with caloric effects. However, there have been some arguments regarding the application of Maxwell relations to first-order phase transitions. This controversy has been discussed in magnetocaloric effects by A. Giguère in 1999 [75] and then followed by comments and replies from J. R. Sun and M. Földeàki in 2000 [76,77], in which they argued that the entropy change cannot be calculated from the Maxwell relations because the first-order phase transition is not a continuous one. It is also suggested that the Clausius-Clapeyron equation [78] can offer a better way to calculate the entropy change in first-order transitions. And this has been well studied by A. Planes and his co-workers in Refs. 74 and 79.

The variation of Gibbs free energy across a first-order phase transition as a function of temperature and pressure is shown schematically in Figure 2.5 (a). For phases I and

II that are far away from the transition, their Gibbs free energies are G_I and G_{II} respectively. The dashed curve indicates the phase coexistence in the first-order phase transition. In particular, considering a transition between phase I to II, a critical point corresponding to the coexistence of two phases can be observed at constant temperature and pressure [see Figure 2.5 (b)]. It is to be noted that the Gibbs energy of phases I and II must be equal ($G_I = G_{II}$) at this critical point to make sure that the mixed system is in an energy stable state. In addition, one can obtain the *T*-*p* diagram by projecting the phase coexistence curve on the *p*-*T* plane.

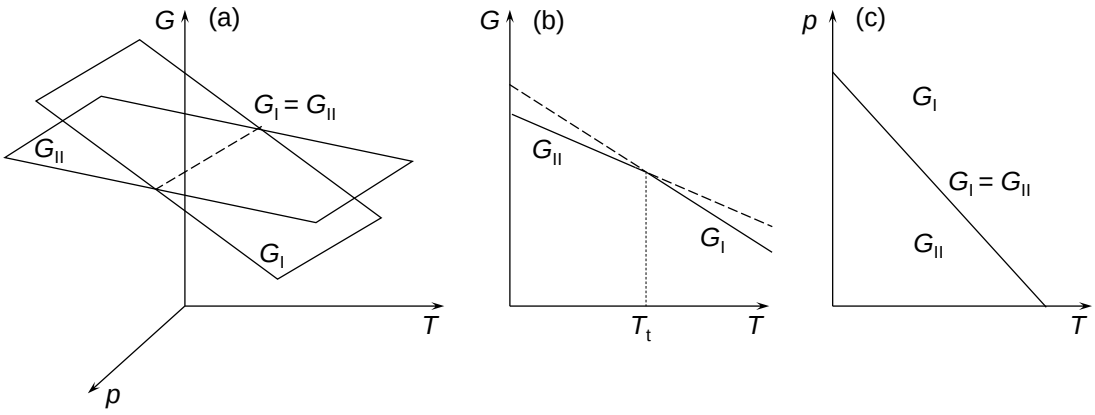

Figure 2.5. Sketches of thermodynamic properties in first-order phase transition. (a) Gibbs free energy as a function of temperature and pressure for phase I and II. The dashed line indicates the coexistence of two phases. (b) Projection of (a) at constant pressure. Solid line indicates the system favoured energy stable state as a function of temperature. T_t corresponds to the phase transition temperature and indicates a change in the slope. (c) Projection of the dashed curve [where $G_I = G_{II}$ in (a)] in *p*-*T* plane.

In Figure 2.6, I schematically show two phase coexistence states in *p*-*T* phase diagram. As these mixed systems are in equilibrium states, we have $G_{\mathrm{I}}^{1} = G_{\mathrm{II}}^{1}$ and $G_{\mathrm{I}}^{2} = G_{\mathrm{II}}^{2}$. Meanwhile, the differential change of Gibbs free energy associated with differential changes of temperature *T* and pressure *p* can be defined as $dG = -SdT + Vdp$ [see Equation (2.3)]. From state 1 to 2, one then can have the following equations in terms of differential steps.

$$dG_{\mathrm{I}} = -S_{\mathrm{I}}dT + V_{\mathrm{I}}dp, \tag{2.10}$$

and

$$dG_{\mathrm{II}} = -S_{\mathrm{II}}dT + V_{\mathrm{II}}dp. \tag{2.11}$$

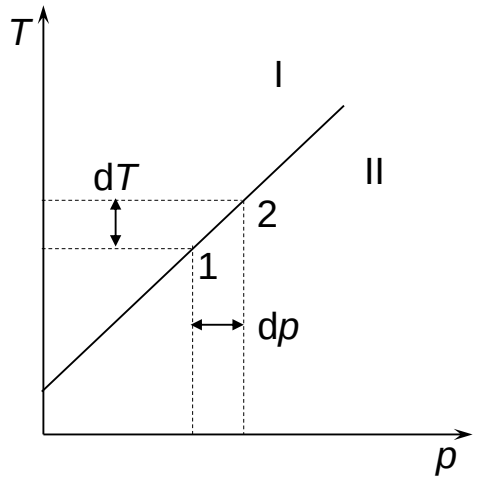

Figure 2.6. Schematic illustration of the *p*-*T* phase diagram. 1 and 2 refer to the phase coexistence states.

Considering that the change of state 1 to state 2 is achieved under an extremely small change of pressure or temperature, we then conclude that the coexistence of the two phases is still stable which means the mixed system moves along the coexistence line

in the phase diagram. As a result, we have $dG_{\mathrm{I}} = dG_{\mathrm{II}}$. Therefore, the Clausius-Clapeyron equation can be expressed as

$$-S_{\mathrm{I}}dT + V_{\mathrm{I}}dp = -S_{\mathrm{II}}dT + V_{\mathrm{II}}dp, \tag{2.12}$$

or

$$\frac{dT}{dp} = \frac{\Delta V_{\mathrm{t}}}{\Delta S_{\mathrm{t}}}, \tag{2.13}$$

where $\Delta V_{\mathrm{t}} = V_{\mathrm{I}} - V_{\mathrm{II}}$, and $\Delta S_{\mathrm{t}} = S_{\mathrm{I}} - S_{\mathrm{II}}$ represent the volume and entropy change across the phase transition respectively, and $\frac{dT}{dp}$ refers to the slope of the coexistence curve. It is clear that the Maxwell relation gives one the thermodynamic expression to calculate the caloric effects for homogeneous systems whereas the Clausius-Clapeyron equation gives the entropy change associated with a first-order phase transition, and it is expected to be usually the major contribution to the caloric effects associated with the transition.

Based on the Maxwell relation and Clausius–Clapeyron equation, two kinds of baro-caloric effects are introduced: the conventional barocaloric effect for $\Delta V_{\mathrm{t}} > 0$ at the endothermic transition, and the inverse barocaloric effect for $\Delta V_{\mathrm{t}} < 0$ at the endothermic transition. In our study, we only focus on the conventional barocaloric effect. Thus, if there is no specific clarification, the barocaloric effect in our research refers to a con-ventional one.

2.4 Impact of thermal hysteresis on barocaloric effects

A first-order phase transition naturally includes thermal hysteresis which is believed to

be detrimental for the cooling applications. Figure 2.7 schematically shows the entropy (*S*) change of the system as a function temperature (*T*) in a first-order phase transition under atmospheric and high pressures, respectively.

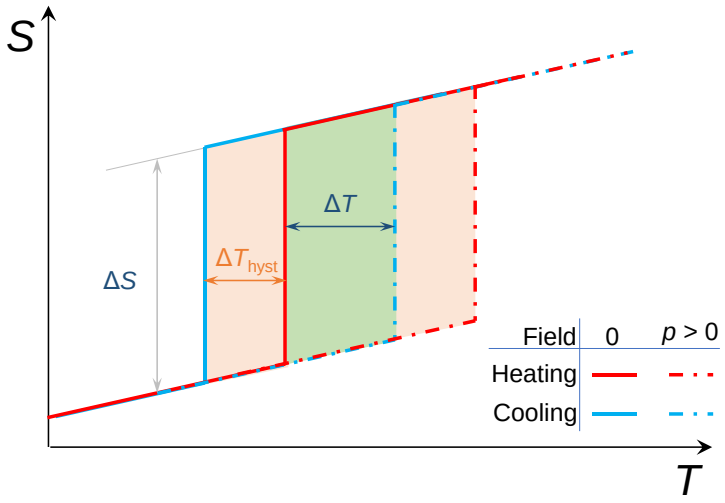

Figure 2.7. The temperature (*T*) dependence of entropy (*S*) curves under constant pressures in a first-order phase transition. The orange parts between the heating and cooling curves show the thermal hysteresis of the first-order transition. The green part presents the reversible transition area under a full phase transition when applying or removing the external pressure.

The sharp increase in the entropy indicates a first-order transition of the system. Both heating and cooling *S*-*T* diagrams are plotted to exhibit the thermal hysteresis which is in orange colour. Assuming that the heat capacity of low-temperature and high-temperature phases and thermal hysteresis are constant under external pressures, we then have the *S*-*T* curves under high pressures. The green part shows a pressure-driven fully reversible phase transition [23], in which a reversible barocaloric cooling is proposed.

In a system without hysteresis, the operation temperature range will include the orange and green parts. Clearly, a large hysteresis can dramatically reduce the temperature range of operation.

More importantly, T. Hess and co-workers suggested that thermal hysteresis has a significant influence on the efficiency of a caloric cooling system [29]. They firstly introduced a Carnot-like refrigeration cycle under the consideration of dissipative losses due to hysteresis. Then, an extra input work ($\Delta W = \Delta T_{\mathrm{hyst}} \Delta S_{\mathrm{iso}}$.) corresponding to the hysteretic process was needed by comparing with a pure Carnot cycle. The impact of hysteresis on efficiency can be verified by introducing the second-law efficiency in an idealized system and this gives

$$\eta \approx \frac{1}{1+4\frac{\Delta T_{\mathrm{hyst}}}{\Delta T_{\mathrm{ad}}}}. \tag{2.14}$$

Based on the above equation, it has been shown that barocaloric materials with a $\Delta T_{\mathrm{hyst}}/\Delta T_{\mathrm{ad}}$ ratio lower than 0.05 will have idealized efficiencies ($\eta > 0.8$) that can be competitive with those of conventional vapor compression-based systems ($\eta \approx 0.85$) [29,80].

In recent years, many efforts have been undertaken to find new materials with low thermal hysteresis [9]. Meanwhile, it is exciting to see that some design strategies have been reported and shown great potential in reducing thermal hysteresis. In shape memory alloys, tuning crystalline symmetry and geometric compatibilities is the most effective method [81]. By adjusting alloy composition, E. Stern-Taulats and co-workers successfully optimized the barocaloric effects in a series of low-hysteresis Ni−Mn−In magnetic alloys [31]. In spin-crossover complexes, a superior barocaloric effect with a

negligible hysteresis has been reported by managing the cooperativity of the spin transition and the rapid structural response to the pressure [59]. A giant reversible barocaloric effect with a tuneable thermal hysteresis has been found in hexagonal $Ni_{1-x}Fe_xS$ by adapting its Fe content [82].

2.5 Measurements of barocaloric effects

2.5.1 Indirect methods

Thermodynamically, indirect calculation of barocaloric effects can be obtained through the Maxwell relations and Clausius-Clapeyron equations [60].

For the Maxwell relation-based method, isothermal entropy changes ΔS are obtained through Equation (2.8) by measuring the volume change under different pressures at different temperatures. As for adiabatic temperature changes ΔT, one may also need to measure specific heat capacity c under different pressures and temperatures as required in Equation (2.9). However, measuring the temperature and pressure dependence of c allows one to estimate the barocaloric effect through a quasidirect method which can avoid the testing of volume and will be discussed later. In practice, values of ΔT were calculated by using $\Delta T \approx -(T\Delta S)/c$ in the limit $\Delta T << T$. The value of c was assumed to be constant under transition and pressures. Experimentally, measuring the volume change under pressure is quite difficult since it is difficult to directly record the volume change of materials in irregular or powder form. Although it has been shown that the volume change can be measured by performing X-ray diffraction or Neutron diffraction under pressures [17], there is no need to do the calculation in this way.

For the Clausius-Clapeyron method, the values of isothermal entropy change ΔS can be obtained through Equation (2.13). Notice that this method is only valid for first-order phase transitions. Also, it fails to include the caloric contribution away from the phase transition. Since $\Delta S = \Delta V(\mathrm{d}p/\mathrm{d}T)$, one can calculate ΔS by measuring the pressure dependence of the phase transition temperature, T_t. Normally, this also gives the information of the T_t-p phase diagram. To plot the phase diagram, one can test the temperature dependence of the volume at different pressures or record the heat-capacity or heat-flux data under various pressures. As for $\mathrm{d}T/\mathrm{d}p$ deduced from the T-p phase diagram, it is important to characterize the sensitivity of phase transition to pressure, which is defined as the barocaloric tunability or barocaloric coefficient in some articles [19, 21]. Generally, a large $\mathrm{d}T/\mathrm{d}p$ value indicates a large entropy change and a reversible barocaloric effect under low pressure [9].

Both Maxwell and Clausius-Clapeyron methods are of great importance in theoretical and experimental studies. Practically, the Maxwell method is used to determine the additional caloric effects that arise from the low or high temperature phases. The Clausius-Clapeyron method is widely used to characterize the phase transition properties under pressure and provides a generalized way to compare barocaloric effects in different materials.

2.5.2 Quasidirect methods

So far, the most used method in calculating barocaloric effects is the quasidirect method through heat-flux data [60]. The basis of heat-flux method involves the construction of

the *S*-*T* diagram by using the temperature dependence of heat flow d*Q*/|d*T*| at constant pressure. Then, Δ*S* can be obtained as follows

$$\Delta S = S(T_1, p) - S(T_0, 0) = \int_{T_0}^{T_1} \frac{1}{T'} \left(c(T', p) + \left| \frac{dQ(T', p)}{dT'} \right| \right) dT', \quad (2.15)$$

where $T_0 < T_1$, $p > 0$ and $T_0 < T' < T_1$. The value of Δ*T* can be calculated using $\Delta T \approx -(T\Delta S)/c$ [17, 20]. A similar method based on heat-capacity data has been used in magnetocaloric and electrocaloric studies, but it has never been reported in barocaloric studies. In this method, d*Q*/|d*T*| was replaced by heat capacity *c* under constant pressure in Equation (2.15). Here, we only introduce the heat-flux method, and a further explanation on the details is presented in Chapter 3.

2.5.3 Direct methods

In recent years, the direct measurement of Δ*T* and Δ*S* have been reported in some papers [20, 83, 84]. Δ*S* was directly obtained by measuring calorimetric curves in isothermal conditions (relatively slow measurements in contact with a thermal bath) under the application and removal of external hydrostatic pressure [20].

The temperature change was measured by a thermocouple placed in a press device. In practice, the adiabatic temperature change must be performed very fast to minimize the heat exchange and thus reach nearly adiabatic conditions [84].

The Direct method also examined and confirmed the validation of indirect and quasidirect methods. With all these methods, barocaloric effects can be presented in a more convincing way.

2.6 Parameters to characterize barocaloric effects

Initially, we have isothermal entropy change ΔS and adiabatic temperature ΔT to characterize barocaloric effects in target materials. For practical refrigeration application, refrigerant capacity (*RC*) [6] and coefficient of refrigeration performance (*CRP*) [7, 85] are introduced to compare the cooling ability or efficiency of caloric materials.

RC value can be calculated by the following equation

$$RC = \Delta S_{max} \delta T_{FWHM}, \tag{2.16}$$

where δT_{FWHM} is the peak width in temperature at half of the maximum ΔS peak. In practice, *RC* refers to the amount of heat that can be transferred between cold and hot reservoirs in a cooling cycle. However, this parameter does not consider the input work that is needed to drive the corresponding cycle.

CRP can be obtained as follows

$$CRP = \left|\frac{\Delta T_{rev} \Delta S}{W}\right|, \tag{2.16}$$

where ΔT_{rev} is the reversible adiabatic temperature change. For barocaloric materials, W is estimated as $W \cong -\frac{1}{2} p \Delta V$, with ΔV being the volume change at the phase transition. *CRP* takes into account the work needed to fully drive a barocaloric cooling cycle.

In addition to the above parameters, some specific features of barocaloric materials should be considered. For example, materials with high thermal conductivity and large density are desired. Also, cheap, safe, and easily synthesised/manufactured materials are preferred.

Chapter 3

Experimental methods

In our experiment, differential scanning calorimetry (DSC) and temperature-dependent X-ray powder diffraction (XRPD) results suggested that there was a pre-transitional regime near the first-order phase transition in all our samples, which refers to a regime close to the transition where the behaviour changes slightly with respect to the behaviour observed further from the transition [17]. Since our high-pressure calorimetry did not capture this pre-transition, we believed that this regime has no contribution to the change of the latent heat in the first-order phase transition. But what is important for our purposes here is that the heat capacity in this regime will depend on pressure, which is essential for barocaloric calculations. Therefore, it is important to distinguish this pre-transition effect in the heat flow and specific heat capacity *c* data measured from DSC.

I first show the determination of transition temperature, latent heat and entropy change in the first-order phase transition. Then, the heat-flux data under constant pressure were measured through high-pressure differential analysis. The *c* data obtained under ambient pressure were collected through DSC and then the method to construct

high-pressure *c* data will be presented. With these data, I finally show the calculation of barocaloric effects through quasidirect heat-flux method.

3.1 Differential scanning calorimetry

In this thesis, thermal data at atmospheric pressure was measured by using a Q100 DSC from TA Instruments at Universitat Politècnica de Catalunya (Barcelona, Spain). A few milligrams of the sample were hermetically encapsulated into Aluminum capsule holders.

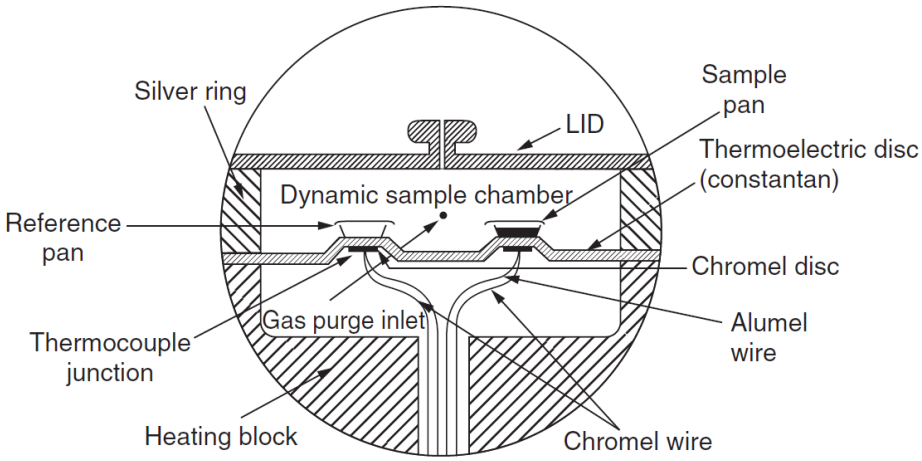

Figure 3.1. Cross section of a *DSC* cell from TA instruments. (Reproduced from Ref. 86)

As shown in Figure 3.1, the heat-flux DSC cell includes holders, sensors, and the heater system [86]. The reference and sample pans are placed on the thermoelectric disc which can transfer the heat in a very fast way and therefore control the heat precisely. Under the disc, two temperature sensors are connected through the

thermocouple junctions. Then, a temperature difference can be detected between sample and reference thanks to the heat capacity or the phase transition of the sample. In the meantime, a purge gas or inert gas flowing through the cell permits a more efficient heat transfer between the disc and the pan by eliminating the hot spots. The heater system consists of a furnace and a temperature sensor, which can control the heating and cooling rate to a constant value. Finally, the differential behaviour of the sample and reference can be promptly recorded by the whole system.

Data collection and analysis:

Heat-flux DSC measures the difference between the heat flows from the sample and reference as a function of temperature or time and this difference arises greatly when a sample absorbs or releases heat due to thermal effects such as phase transition. The consequent heat flow is determined by the thermal equivalent of Ohm's law:

$$\dot{Q} = \frac{\Delta T_{\mathrm{s-r}}}{R}, \tag{3.1}$$

where $\dot{Q}$ is the heat flow rate, $\Delta T_{\mathrm{s\text{-}r}}$ is the temperature difference between the sample and the reference, and R is the thermal resistance of the thermoelectric disk.

Figure 3.2 shows the steps to determine the transition temperature, latent heat and entropy change properties by using DSC data in $(C_{10}H_{21}NH_3)_2MnCl_4$ crystals as a case study. Figure 3.2 (a) and (b) show the endothermic peak recorded upon heating in the first-order phase transition. Baselines of these heat flow curves were obtained by doing a linear fitting for the heat flow data away from the phase transition (peak). In general, transition enthalpy changes, ΔH_{t}, and transition entropy changes, ΔS_{t}, can be obtained

from the integration of peaks in dQ/|dT| and in (1/T)dQ/|dT|, respectively, after baseline subtraction between temperatures T_1 and T_2 suitably chosen below and above the pressure-dependent first-order transition range. For a phase transition with pre-transitional regime, we carefully chose T_1 and T_2 based on the following discussion.

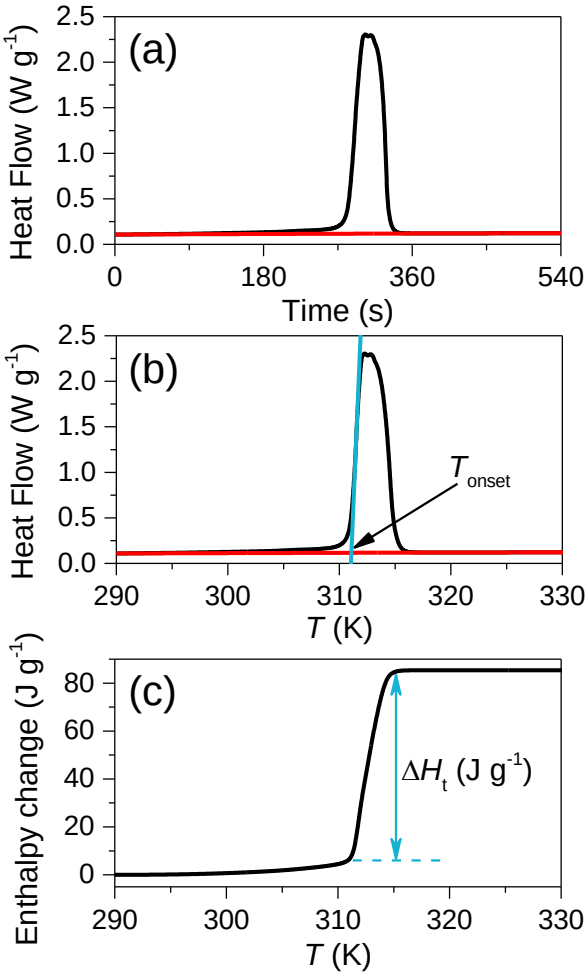

Figure 3.2. DSC data analysis. (a) Heat flow vs time. Red line is the baseline obtained from linear fitting. (b) Heat flow vs temperature. The phase transition temperature T_{onset} is the intersection point of blue and red lines. Blue line is the tangent line at the maximum slope point of the peak. (c) The total enthalpy change obtained from (b) by integrating the curves.

Figure 3.2 (b) shows the determination of the onset temperature (T_{onset}) of the phase transition. To determine the T_{onset}, one needs to draw a tangent line at the maximum slope point of the endothermic peak. Then, T_{onset} was defined as the temperature value of the intersection point of the tangent line and baseline line. Here, we see T_{onset} as the transition starting point or phase transition temperature [17]. However, the staring temperature T_1 in integration may start below T_{onset}, which will be discussed later. In the same way, we can find the transition ending point. These defined temperature ranges agreed well with the temperature dependence of volume data obtained from the temperature-dependent XRPD (details can be found in Chapters 4 and 5). With the newly defined order transition temperature range, we now processed to choose the integration temperature range. We firstly plot the total entropy or enthalpy change from integration of peak in Figure 3.2 (b). With the result shown in Figure 3.2 (c), we can easily identify the entropy change arising in the pre-transitional region and the entropy change associated with the first-order phase transition. Considering this turning point, we carefully selected the starting temperature T_1 ($T_{onset} > T_1$) and the finishing temperature T_2 for integration. In addition, we can also define the temperature range for pre-transition and first-order transition respectively. Finally, the enthalpy and entropy changes were obtained through the integration of the endothermic peak within reasonable temperature range.

The baseline chosen for integration in the low-temperature interval may be a source of significant uncertainty due to a smooth tail below the transition peak corresponding to the pre-transitional regime. In some cases, this tail is observed to extend more than 50 K below the first-order transition peak, and may depend on the temperature rate of

measurement [17]. Therefore, we also pay attention to the relations between heat flow and temperature rates as shown in Figure 3.3. Measurements of heat flow dQ/|dT| at atmospheric pressure performed using the commercial DSC Q100 at different temperature rates from 1 to 10 K min^{-1} show that both endothermic and exothermic T_{onset} are basically rate-independent and therefore hysteresis is also rate-independent within the temperature rates used in the investigations. Endothermic and exothermic transition temperature peaks are slightly shifted to higher and lower temperatures, respectively, due to the fact that the temperature is measured at an empty aluminum capsule. In our experiment, heating and cooling ramps were performed at ±2 K min^{-1}.

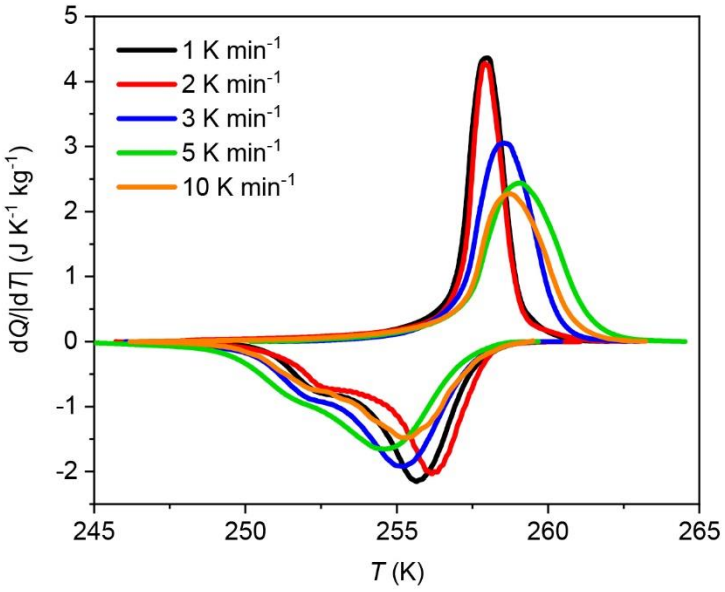

Figure 3.3. Heat flow in temperature measured by commercial Q100 (TA Instruments) across the endothermic (positive) and exothermic (negative) transitions at different temperature rates, after baseline subtraction.

3.2 High-pressure differential thermal analysis

A high-pressure differential thermal analysis (HPDTA) system in the Departament de Física at Universitat Politècnica de Catalunya was used in the experiment. Figure 3.4 schematically shows the components in HPDTA system [73].

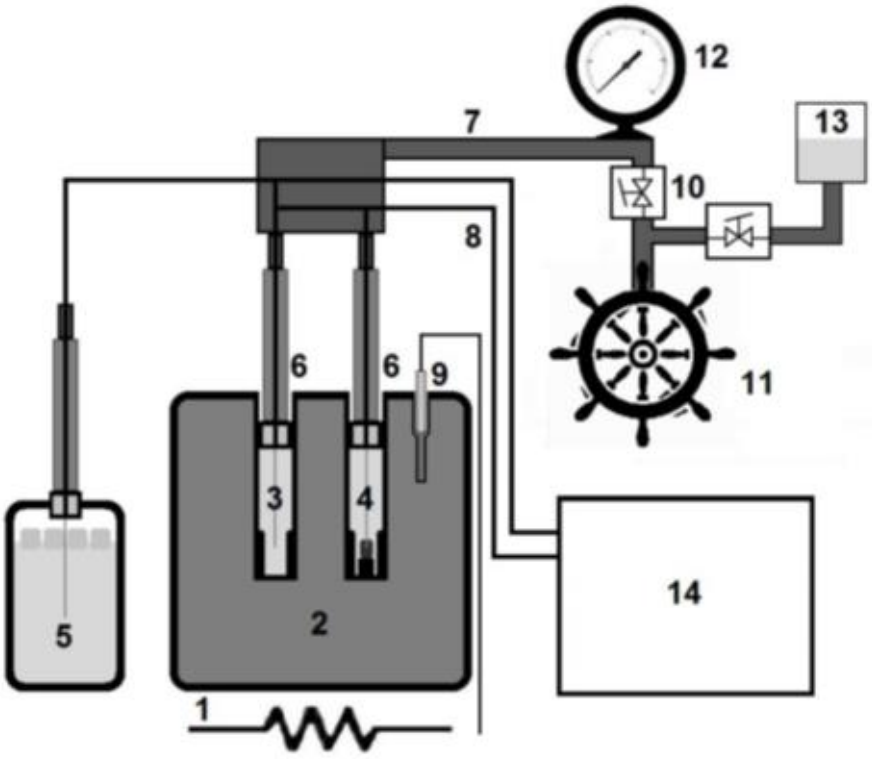

Figure 3.4. A schematic diagram of high-pressure differential thermal analysis system. 1: Resistive heater, 2: Calorimetric block, 3: Reference enclosure with a thermocouple connection, 4: Sample enclosure with a thermocouple connection, 5: Ice container with a thermocouple connection, 6: High pressure Bridgman seals, 7: Capillaries for the high pressure liquid conduction, 8: Thermocouple wires, 9: Pt-100 thermometer for the resistor temperature control software, 10: Valves, 11: Pressure pump, 12: Manganin manometer, 13: High pressure liquid reservoir, and 14: Data acquisition system. (Reproduced from Ref. 27)

HPDTA was performed by using two different bespoke variable-pressure calorimeters, and they were named calorimeter A and calorimeter B. The operation pressure range for calorimeter A is from atmospheric pressure to 0.3 GPa, and Bridgman thermocouples were used as thermal sensors. The operation pressure range for calorimeter B is from atmospheric pressure to 0.6 GPa, and Peltier modules were used as thermal sensors. In calorimeter A, the working temperature range is from room temperature to 473 K. The heating ramps were performed at 2 K min^{-1} using a resistive heater, and cooling ramps were performed on average at around 1 K min^{-1} with an air stream system. The slower cooling (as opposed to the heating rate) of calorimeter A is because this relies on air cooling and is thus also not precisely controlled. In calorimeter B, the temperature was controlled by a thermal jacket connected to an external thermal bath from Lauda Proline 1290, within the range 200 - 393 K, with temperature rate on heating of 2 K min^{-1} and on cooling of −2 K min^{-1}.

Powdered samples of about 200 mg of mass were mixed with inert perfluorinated liquid bought from Galden Bioblock Scientist. After carefully removing the air in the sample and fluid, the mixtures were encapsulated inside tin capsules that were attached to the thermal sensors. The pressure transmitting fluid used here was DW-Term M90.200.02 (Huber) and the pressure was measured through the use of a high-pressure transducer module HP made by Honeywell. This module was attached to the high-pressure circuit which allows the measurement of pressures with a precision of < 0.001 GPa. To verify that the inert fluid was chemically inactive and did not modify the thermodynamic properties of the phase transition, preliminary DSC measurements were

carried out with a sample-inert fluid mixture at atmospheric pressure on the commercial differential scanning calorimeter.

Data collection and analysis:

Figure 3.5 (a) and (b) show the heat flow data recorded by the HPDTA system against time and temperature respectively. The HPDTA system did not record a pre-transitional tail [see T_{onset} in Figure 3.5 (b)] because the use of pressure and a pressure transmitting liquid introduces a larger signal to noise ratio as compared to commercial setup that only operates at atmospheric pressure and uses gas as environment. We can associate the integrated values entirely with the first-order transition. Therefore, in a general way, ΔH_t and ΔS_t, can be obtained from the integration of peaks in $dQ/|dT|$ and in $(1/T)dQ/|dT|$, respectively, after baseline subtraction between temperatures T_1 and T_2 suitably chosen below and above the pressure-dependent first-order transition range. As mentioned before, $T_{onset} > T_1$.

For better illustration, here we chose heat flow curves upon heating at 0 and 1 kbar as a case study. In our HPDTA, the outputs of the calorimetric signal are voltage [73] which must be transferred to heat flow units. But one still can determine the pressure dependence of phase transition temperature from Figure 3.5 (b). The results are shown in Figure 3.5 (c). We knew from the previous studies that the pressure-transmitting fluid is inert and does not modify the thermodynamic properties of the material. Also, DSC values have considerably smaller error than the calorimetric values obtained in the high-pressure cell. Therefore, we can simply do the calibration by using the entha-

lpy change and entropy change of the data obtained from DSC at normal pressure.

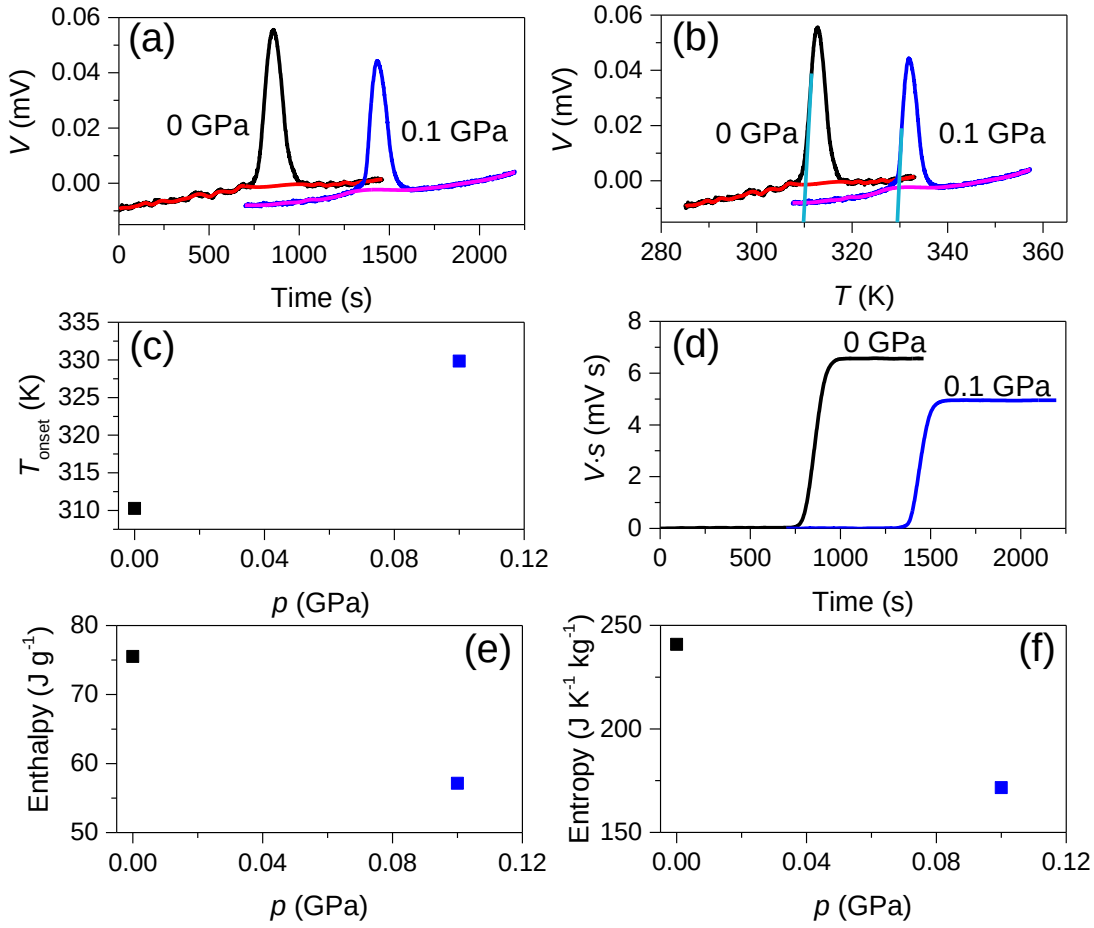

Figure 3.5. (a) and (b) Heat flow data obtained from HPDTA at 0 and 0.1 GPa. (c) phase transition temperature as a function of pressure. (d) integrated curves at 0 and 0.1 GPa. (e) and (f) Rescaled enthalpy and entropy changes as a function of pressure.

Firstly, we obtained the value of enthalpy change by integrating curves in Figure 3.5 (a) after subtracting the baseline [see Figure 3.5 (d)] and then we can scale all the high-pressure data with a multiplying factor that was obtained by the DSC data divided by

the intercept of the corresponding linear fit. Therefore, the intercept of the scaled linear fits will be precisely the DSC values and consequently all the scaled data will be in heat flow units.

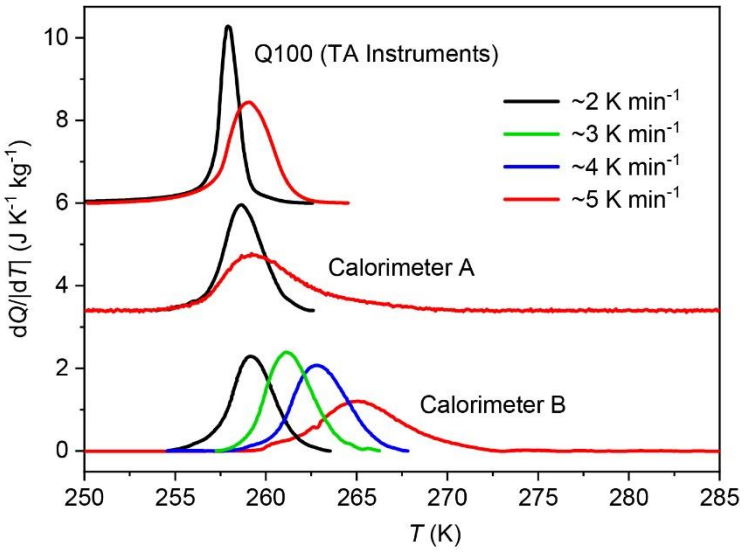

Figure 3.6. Heat flow in temperature measured by the three different calorimeters at atmospheric pressure and at different temperature rates, after baseline subtraction. Peaks have been shifted vertically for clarity.

Figure 3.6 shows a comparison of heat flow measurements performed across the endothermic transition using the three different calorimeters at different temperature rates. It can be seen that in calorimeters Q100 and A, the T_{onset} is basically independent of temperature rates whereas in calorimeter B it does depend on temperature rates. This artifact arises because the thermocouple measuring temperature in calorimeter B is placed at a certain distance from the sample and closer to the thermal jacket of the high-pressure cell. This introduces a delay between the measured temperature and sample

temperature such that, given the same remaining experimental conditions, the higher temperature rates, the larger the difference between the two quantities. Our variable-pressure measurements on heating used for the calculations of the barocaloric effect were performed at the highest rate allowed by the thermal bath (5 K min^{-1}). While this rate introduces a larger uncertainty in temperature, it gives rise to a smoother baseline, which leads to a lower uncertainty in the determination of the transition entropy changes. With respect to cooling ramps, maximum absolute temperature rates allowed by the thermal bath are much lower (2 K min^{-1}) than heating ramps, which introduces much smaller errors in the exothermic transition temperatures measured by calorimeter B than those corresponding to the endothermic ones. Variations in the barocaloric response originating in this fact are within the error reported in the main text (Chapter 4 and 5) and therefore do not affect the results nor conclusions of the present study.

3.3 Heat capacity at different pressures

Measurements of specific heat capacity *c* were performed at atmospheric pressure in a commercial DSC (TA Q2000) using a standard method [86]. The used reference was sapphire (crystalline Al_2O_3). The heating and cooling rate were 5 K min^{-1}.

As discussed at the beginning of this chapter, the heat capacity in the pre-transition regime depends on the pressure. The pressure-dependence of *c* is given by the following thermodynamic relations:

$$\left(\frac{\partial c}{\partial p}\right)_T = -T\left(\frac{\partial^2 V}{\partial T^2}\right)_p, \tag{3.2}$$

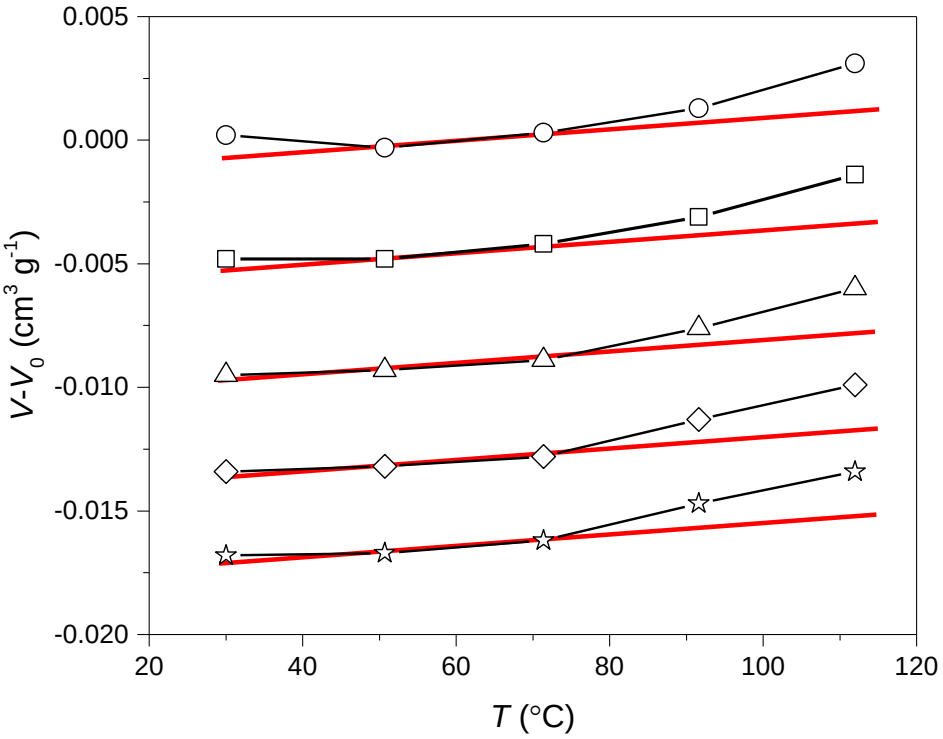

Figure 3.7. Black symbols and lines: Temperature- and pressure-dependent specific volume (reproduced from Ref. 87). From top to bottom, literature data is measured at 10, 50, 100, 150 and 200 MPa. Red straight lines have the slope $(\frac{\partial V_{\mathrm{fcc}}}{\partial T})_{p_{\mathrm{atm}}}$ as obtained by our x-ray diffraction measurements at atmospheric pressure.

Above equation indicates the dependence of $V(T)$ in pressure is important for the construction of the heat capacity. Therefore, a more detailed explanation for the construction of the temperature- and pressure-dependent heat capacity is introduced here by considering Equation (3.2). The data of C_{60} are used as a case study. First, in Figure 3.7 we reproduce temperature- and pressure-dependent volume data from the face-centered-cubic (fcc) phase provided by Ref. [87] (black lines and symbols). By using these data, we firstly evaluated the right-hand side of Equation (3.2). On top of these data,

we have plotted red straight lines with the slope $(\frac{\partial V_{\mathrm{fcc}}}{\partial T})_{p_{\mathrm{atm}}}$ as determined from our XRPD measurements at atmospheric pressure (p_{atm}) in the temperature range 265-360 K. The good agreement between the two sets of data in the temperature range of interest allows us to reasonably assume that

$$(\frac{\partial V_{\mathrm{fcc}}}{\partial T})_{p} \approx (\frac{\partial V_{\mathrm{fcc}}}{\partial T})_{p_{\mathrm{atm}}}. \tag{3.3}$$

The $V(T)$ data obtained from our x-ray measurements reveal different behaviour in four temperature intervals: For $T \in (150, 250)$ K and $T \in (265, 360)$ K, $V(T)$ is linear; for $T \in (250, 260)$ K, $V(T)$ is nonlinear; and around the transition $V(T)$ is nearly discontinuous (See Figure 3.8). Then, given the assumption in Equation (3.3), we can construct a $V(T)$ plot at a higher pressure p such that all the mentioned regimes are shifted to higher temperatures by an amount given by $\frac{dT}{dp}(p - p_{atm})$ [as represented by the black arrow between the peaks in heat flow at two different pressures displayed in Figure 3.9 (a)]. Here $\frac{dT}{dp}$ is the transition temperature shift determined experimentally [see example in Figure 3.5 (c)]. The resulting qualitative $V(T)$ curves at two different pressures are shown in Figure 3.9 (b), where dashed lines separate linear and nonlinear $V(T)$ regions.

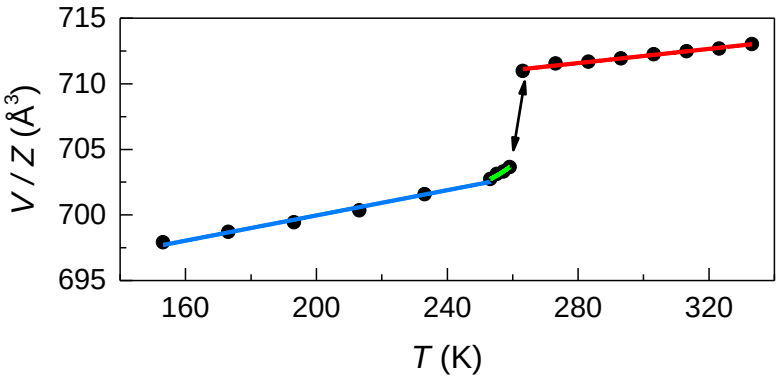

Figure 3.8. Temperature-dependent unit cell volume per formula unit of C_{60} showing the different behaviours over different temperature ranges.

Equation (3.2) can be used to establish the dependence of the heat capacity on pressure, from literature data [88]. Therefore, in the temperature intervals where $V(T)$ is linear, c is independent of pressure whereas in the temperature intervals where $V(T)$ is not linear, c depends on pressure [see Figure 3.9 (c)]. In the latter region, $V(T)$ appears to be concave, which means that $\left(\frac{\partial^2 V}{\partial T^2}\right)_p > 0$. This means that, according to Equation 3.2, c decreases when increasing pressure and the decrease is larger at higher temperature. This feature can be seen qualitatively in the region $T_1 < T < T_2$ in Figure 3.9(c).

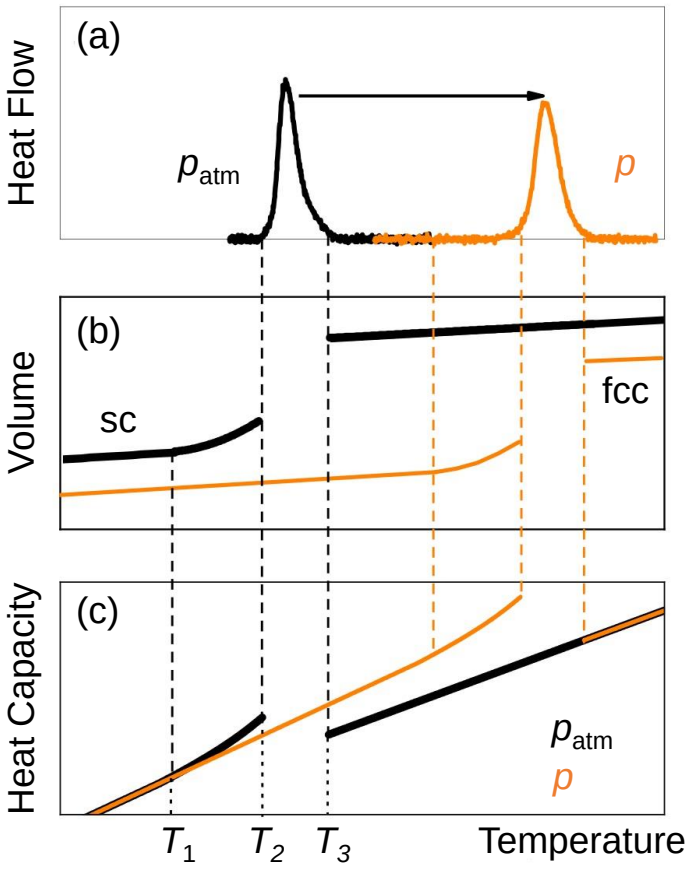

Figure 3.9. Qualitative plots for the construction of the heat capacity. (a) Temperature-dependent transition heat flow measured at p_{atm} and p, after baseline subtraction. (b) Temperature-dependent volume at two different pressures, p_{atm} and p, assuming that in each phase $(\frac{\partial V_{fcc}}{\partial T})_{p} \approx (\frac{\partial V_{fcc}}{\partial T})_{p_{atm}}$. (c) Temperature-dependent heat capacity at p_{atm} and p, constructed from data in panels (a) and (b).

3.4 Quasidirect method

Characterization of reversible caloric effects is an essential step in barocaloric study. As it discussed in Chapter 2, direct and quasidirect measurements are more reliable

methods in the evaluation of BC effects compared with indirect methods using thermodynamic Maxwell relations. There is no doubt that direct methods can naturally characterize reversible effects as they can dynamically record the thermal effect in changing pressures. In contrast, quasidirect measurements are achieved by increasing or decreasing the temperature at constant hydrostatic pressures, which means that additional calculation is required to convert these data. Moreover, the characterization of hysteretic effects in first-order phase transitions is essential for the determination of reversible barocaloric effects. In doing this, one needs to transform these as-measured isobaric thermal-driven data to isothermal pressure-driven data through the use of specific calculations. It is to be noted that quasidirect methods are now well established by comparing the experimental data from direct and quasi-direct meathods. Reversible isothermal entropy changes ΔS_{rev} can be evaluated from the overlap between isothermal entropy changes ΔS obtained upon first application and removal of pressure, and the ΔS can be obtained from the entropy (S) - temperature (T) curves determined from isobaric measurements [27]. This is the method that has been used in this thesis to study BC effects, which includes two main steps: (i) construction of the entropy curves, (ii) subtraction of entropy curves.

3.4.1 Construction of the entropy curves

Using specific heat data at atmospheric pressure, specific volume data at atmospheric pressure, and $dQ/|dT|$ at constant pressure, we can calculate $S'(T,p) = S(T,p) - S(T_0, p_{atm})$ through the following equation:

$$S'(T,p)=\begin{cases} S(T_0,p)+\int_{T_0}^{T}\frac{c_{\mathrm{II}}(T',p)}{T'}dT' & T_0\le T\le T_1(p) \\ S(T_1,p)+\int_{T_1}^{T}\frac{1}{T'}\left(c_{\mathrm{II-I}}(T',p)+\left|\frac{dQ(T',p)}{dT'}\right|\right)dT' & T_1(p)\le T\le T_2(p), \\ S(T_2,p)+\int_{T_2}^{T}\frac{c_{\mathrm{I}}(T',p)}{T'}dT' & T\ge T_2(p) \end{cases} \quad (3.4)$$

where $S(T_0,p)$ is a pressure-dependent entropy at a reference temperature T_0 chosen below the transition temperature at pressure p. And $T_1(p)$ and $T_2(p)$ are pressure-dependent temperatures limiting the phase transition. Then, $dQ(T,p)/|dT|$ is the pressure-dependent heat flow value associated with the latent heat of the first-order phase transition, and measured by our pressure-dependent calorimetry. $c_{\mathrm{II}}(T,p)$ and $c_{\mathrm{I}}(T,p)$ are the heat capacities of low-temperature and high-temperature phases, respectively. And $c_{\mathrm{II\text{-}I}}(T,p)=[1-x(T,p)]c_{\mathrm{II}}(T,p)+x(T,p)c_{\mathrm{I}}(T,p)$ represents the specific heat capacity within the phase transition region, where $x(T,p)$ is the fraction of the system in the high-temperature phase and can be calculated as

$$x(T,p)=\frac{\int_{T_1}^{T}\frac{1}{T'}\frac{dQ(T',p)}{dT'}dT'}{\int_{T_1}^{T_2}\frac{1}{T'}\frac{dQ(T',p)}{dT'}dT'},\ T_1(p)\le T\le T_2(p). \quad (3.5)$$

Notice that the methods of calculating the $c(T,p)$ throughout all the pressure-dependent temperature intervals were presented in Section 3.3 using C_{60} as a case study.

The fact that at T_0, $\left(\frac{\partial V}{\partial T}\right)_{p_{\mathrm{atm}}}\neq 0$ indicates that the reference entropy must depend on pressure due to the Maxwell relation

$$S(T_0,p)=S(T_0,p_{atm})-\int_{p_{atm}}^{p}\left(\frac{\partial V}{\partial T}\right)_{p'}dp', \quad (3.6)$$

where $S(T_0,p_{atm})=\int_0^{T_0}\frac{c(p_{atm})}{T}dT$. Assuming the condition in Equation (3.3), we can write $\Delta S_+(T_0,p)=S(T_0,p)-S(T_0,p_{atm})\approx\left(\frac{\partial V}{\partial T}\right)_{p_{\mathrm{atm}}}(p-p_{\mathrm{atm}})$, where $\left(\frac{\partial V}{\partial T}\right)_{p_{\mathrm{atm}}}=$

3.7×10^{-8} m^{-3} kg^{-1} K^{-1} can be calculated by using data in $V(T)$ from our XRPD measurements. This can be understood as a signature that at temperatures well below the pressure independent regime, c must depend on pressure, because $S(T_0, p)$ could also be calculated directly as $S(T_0, p) = \int_0^{T_0} \frac{c(p)}{T} dT$ if c was available at pressure p.

Combining all these elements in Equation (3.4), we can finally construct the temperature-dependent isobaric entropy curves at different pressures. It is worth noting that the additional entropy changes above the transition, ΔS_+, can be obtained in the procedure for constructing the entropy curves. At the same time, this ΔS_+ can be calculated through the Maxwell relation by using $\left(\frac{\partial V}{\partial T}\right)_{p_{\mathrm{atm}}} = \left(\frac{\partial S}{\partial p}\right)_T$ above the phase transition. The magnitudes for this quantity obtained by using these two methods independently are in agreement within error, which confirms the validity of the constructed entropy curves. For example, under pressure change of 0.22 GPa, the calculated ΔS_+ from Maxwell relation is about 8 ± 1 J K^{-1} kg^{-1}, and the value obtained from entropy curves is 6 ± 1 J K^{-1} kg^{-1}.

3.4.2 Conventional barocaloric effects

We schematically constructed the entropy–temperature curves in Figure 3.10 (a) and (b). For conventional BC effects ($dT/dp > 0$), transitions on decompression (compression) are endothermic (exothermic) and therefore, ΔS and ΔT on first decompression (compression) must be computed from isobaric entropy functions on heating (cooling). Isothermal entropy changes are computed by subtracting $S(T, p)$ curves following isothermal paths: $\Delta S(T, 0 \rightarrow p) = S(T, p) - S(T, 0)$. In turn, adiabatic temperature changes

are computed by subtracting the entropy–temperature curves following adiabatic paths: $\Delta T(T_s, 0 \rightarrow p) = T(S, p) - T(S, 0)$, where ΔT is more appropriately plotted as a function of the starting temperature T_s because the system temperature changes along the adiabatic path. More importantly, this feature entails that the reversible ΔT usable in cooling devices that work in sequential compression–decompression cycles, are given by $|\Delta T_{rev}(S, 0 \leftrightarrow p)| = |T_C(S, p) - T_H(S, 0)|$, where T_C and T_H refer to the temperature within cooling and heating respectively [see left-right green arrow in Figure 3.10 (b)]. In turn, ΔS_{rev} can be determined as the overlapping between $\Delta S(T, 0 \rightarrow p)$ and $\Delta S(T, p \rightarrow 0)$ [see green arrow in Figure 3.10 (a)].

Another important feature for BC effects is the required minimum pressure, p_{rev}. To achieve nonzero ΔT_{rev}, the p_{rev} is generally given by the value at which the exothermic transition temperature equals the endothermic transition temperature at atmospheric pressure. In fact, the p_{rev} to obtain non-zero ΔS_{rev} is lower than the value estimated from the above method, which has been well presented and discussed in Ref. 27. This will be shown and discussed in Chapters 4 and 5.

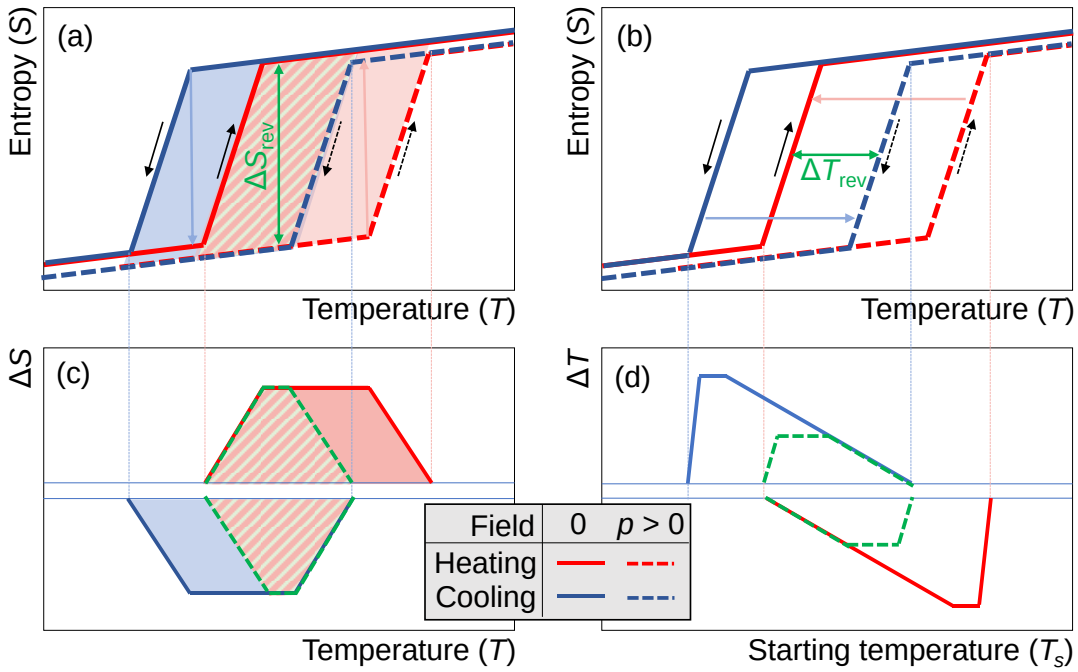

Figure 3.10. Schematic isobaric entropy–temperature curves and conventional BC effects to evaluate reversibility. (a) and (b) Isobaric entropy curves at atmospheric pressure 0 (solid line), and high-pressure $p > 0$ (dotted line) respectively. The red and blue colours represent heating and cooling (as indicated by the black arrows), respectively. (a) The blue vertical downward arrow indicates the thermodynamic path used to calculate irreversible isothermal entropy changes ΔS on compression. Red vertical upward arrow for decompression. (b) The horizontal rightward arrow displays the thermodynamic paths used to calculate irreversible adiabatic temperature changes ΔT on compression. Leftward for decompression. The left-right green arrow exhibits the thermodynamic path used to calculate reversible ΔT. (c) Irreversible ΔS obtained under a pressure increase of $p - 0$ (blue, solid) and under a decrease of $0 - p$ (red, solid). The area with green slash lines represents the reversible ΔS obtained from overlapping the curves obtained upon increasing and decreasing the field. (d) Irreversible ΔT obtained under a pressure increase of $p - 0$ (blue, solid) and under a decrease of $0 - p$ (red, solid). The area within the green dashed lines indicates the reversible ΔT. (Reproduced from Ref. 27)

Chapter 4

Barocaloric effects in fullerite C_{60}

This chapter introduces the features that suggested fullerite crystals as promising barocaloric candidates, and then details its phase transitions and barocaloric properties through experimental studies. The result of the study demonstrates that C_{60} exhibits outstanding barocaloric properties. In particular, a large transition entropy change and a small transition hysteresis result in a giant reversible barocaloric effect in C_{60}. This giant effect can be obtained at very small pressure changes thanks to the high sensitivity of the transition to the applied pressure. Furthermore, at moderate pressure changes, giant reversible barocaloric effects are obtained over a very wide temperature range, which indicates its great barocaloric tunability and thus expands the operational temperatures around room temperature.

4.1 Buckminsterfullerene C_{60} and its crystal form

In 1985, the structure of C_{60} molecule was reported by Kroto and co-workers, who recognized it as a football-like structure or Buckminsterfullerene [89]. Accordingly,

the C_{60} molecule has a truncated icosahedral structure which shows a polyhedron with 60 vertices and 32 faces, 12 of which are pentagonal and 20 hexagonal [see Figure 4.1 (a)] [90]. Solid C_{60} with perfect quality can be prepared from C_{60} vapor by using a sublimation-condensation method [91]. After that, the bond lengths, crystal structure of solid C_{60} and its transition were intensively studied through the use of NMR [92], X-ray diffraction [93] and Raman spectroscopy [94]. It was known that solid C_{60} forms a face-centred-cubic (fcc) structure with a space group of $Fm\bar{3}m$ at room temperature [see Figure 4.1 (b)], in which the molecules are randomly rotating between various orientations, forming a "plastic crystal". The successful synthesis and characterization of C_{60} and the family of fullerenes has stimulated a variety of studies on the fullerene-based solids' chemical and physical properties including, but not limited to the polymerization and dimerization of C_{60} [95], electric and magnetic properties [96], mechanical response [97], thermal conductivity [98] and superconductivity [99].

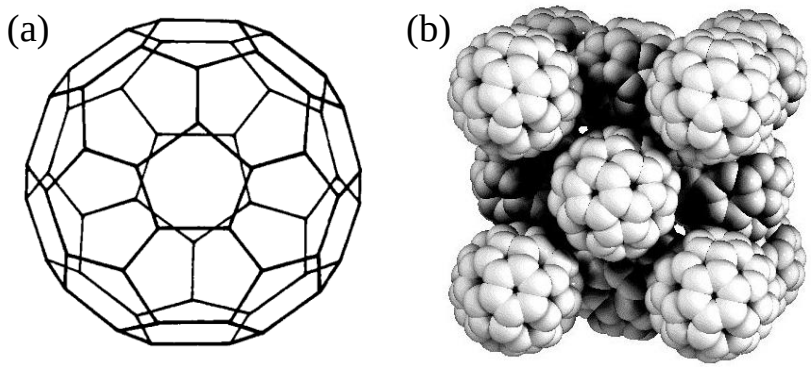

Figure 4.1. The illustration of (a) the C_{60} buckminsterfullerene molecule and (b) the crystal structure of C_{60} solid at room temperature. (Reproduced from Ref. 90)

In addition, the vast majority of research on solid C_{60} has been done on the phase transition and its dynamic properties. For instance, Heiney and co-workers [100] demonstrated that the room temperature fcc structure undergoes a first order transition to a primitive cubic (sc) structure with a space group of $Pa\bar{3}$ below 255 K by using synchrotron X-ray powder diffraction and differential scanning calorimetry measurements. The latent heat of the phase transition is 6.7 J g^{-1}. In the conventional unit cell of an fcc lattice, the interaction between neighbouring C_{60} molecules is dominated by the spherically symmetric component which reveals that the orientational dynamics of molecules have a pronounced effect on the dynamics of the crystal. Furthermore, Samara and co-workers investigated the influence of pressure on the phase transition and corresponding molecular orientational ordering properties in solid C_{60} [101]. They found that external pressure can greatly change the transition temperature which increases with pressure at a rate of about 104 K GPa^{-1}. Additionally, the applied pressure can make a more ordered low-temperature sc phase by reducing the orientational fluctuations of C_{60} molecules (see Figure 4.2). Interestingly and importantly, their experimental results indicate that there are two ordering transitions near 249 K under higher pressure, which corresponds to two orientational configurations of the molecules in the sc phase. Similarly but more obviously, in Fischer and co-workers' research, they reported two ordering transitions in high-purity powder and single crystal C_{60} under ambient pressure through the use of modulated differential scanning calorimetry. Also, the results show that the hysteresis and latent heat of the fcc-to-sc phase transition highly rely on the purity of the sample. In addition to the order-disorder phase transition occurring near 255 K, two extra interesting phase transitions have also been discovered

at around 90 K and 530 K [102, 103], However, there has been little work published on these transitions.

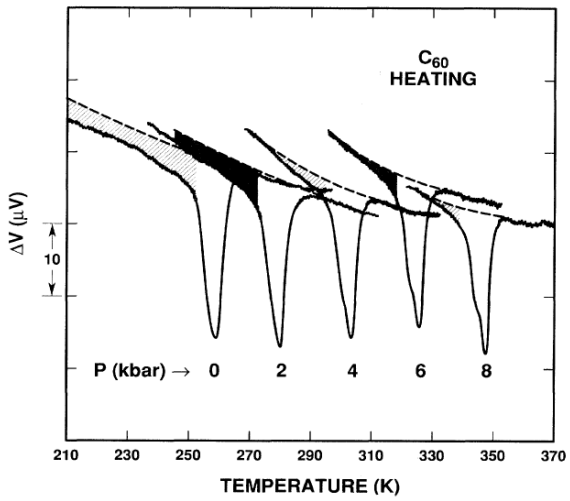

Figure 4.2. Differential-thermal-analysis (heating) scans of solid C_{60} at different pressures showing the behaviour in the vicinity of the sc-fcc transition. (Reproduced from Ref. 101)

Overall, solid C_{60} and its phase transition properties has been widely studied by using various tools under both ambient and high pressures. It is known that the transition dynamics of the fcc-to-sc first-order phase transition are related to the orientational dynamics of the C_{60} molecules and there is a large latent heat of this phase transition which is sensitive to the purity of the sample and also the external pressure.

4.2 Motivation

Carbon materials such as graphite [104], diamond [105], graphene [106,107], carbon nanotubes [108,109] and fullerenes [110] have shown superior mechanical, electrical,

thermal and optical properties for practical applications. Interestingly, these materials have also been considered for caloric purposes. For example, theoretical studies have been performed on the electrocaloric (EC), elastocaloric (eC) and barocaloric (BC) effects in graphene [111-113], and the eC effect in carbon nanotubes [111]. However, experimental studies are still lacking for these compounds. Here, I selected fullerite C_{60}, the molecular crystal of C_{60} (buckminsterfullerene) as a promising BC candidate because it undergoes an order–disorder transition towards a plastic crystal phase near room temperature. As mentioned in the introduction, materials undergoing transitions involving a strong order–disorder change are attracting increasing interest because the disordering process may lead to large entropy changes and therefore may show better BC performance.

In the fcc phase, the orientational disorder in C_{60} is prototypical because the quasi-spherical molecular shape permits a quasi-free rotation as suggested by NMR [92] and X-ray [93] experiments and the unique excellent agreement with the Pauling–Fowler model [114]. At a temperature of $T \sim 257$ K, fullerite C_{60} undergoes a first-order phase transition on cooling across which, in addition to a volume reduction, the molecular orientations order partially, reducing significantly the number of possible orientations. As a consequence, the four sites that are equivalent in the fcc phase become distinguishable in the low-temperature phase, reducing the fcc symmetry to a sc lattice. This symmetry breaking can be seen in the unit cells for both sc and fcc phases. Interestingly, the orientational disordering across the phase transition is a source for a giant transition entropy change ΔS_t of ~25–50 J K^{-1} kg^{-1} [94,100-102,115-117]. This

value is lower than the colossal values reported for other plastic crystals because on the one hand the elemental rotating units are heavy rigid molecules and on the other hand in the sc phase the ordering is not complete. However, some research works demonstrated that fullerite C_{60} shows a small transition hysteresis and a high sensitivity of the transition to the applied pressure which allows us to obtain giant reversible BC effects at very small pressure changes [100]. Therefore, I performed a detailed BC study on fullerite C_{60}.

4.3 Structural and thermodynamic properties of C_{60} at atmospheric pressure

Crystalline powder of C_{60} (99.5 wt% purity) was purchased from Sigma-Aldrich and used as such. We studied the structural properties of C_{60} under different temperature at ambient pressure by using temperature-dependent X-ray powder diffraction (XRPD).

The results at atmospheric pressure confirmed the expected sc phase ($Pa\bar{3}$, with Z = 4 formula units per unit cell) at low temperatures, which transforms to the fcc phase ($Fm\bar{3}m$, Z = 4) around $T \sim 260$ K [see Figure 4.3 (a) and (b)]. Figure 4.3 (c) shows the temperature evolution of the unit cell volume per formula unit $V(T)/Z$ which is determined by means of Rietveld analysis according to the recorded XRPD patterns (see Figure A1 in Appendix A). The finite volume change at the first-order phase transition (indicated with a double arrow in the figure) corresponds to a large relative increase on heating of $\Delta V_t/V_{sc} \sim 1\%$. Both above and well below ($T < 250$ K) the transition, $V(T)$ shows a linear behaviour as indicated by the red and blue linear fits, respectively,

whereas below but close to the first-order transition (250–260 K), $V(T)$ shows a non-linear behaviour as indicated by the second-order polynomial fit (green line). In view of previous studies [115-117], this nonlinear $V(T)$ regime can be associated with a pre-transitional regime.

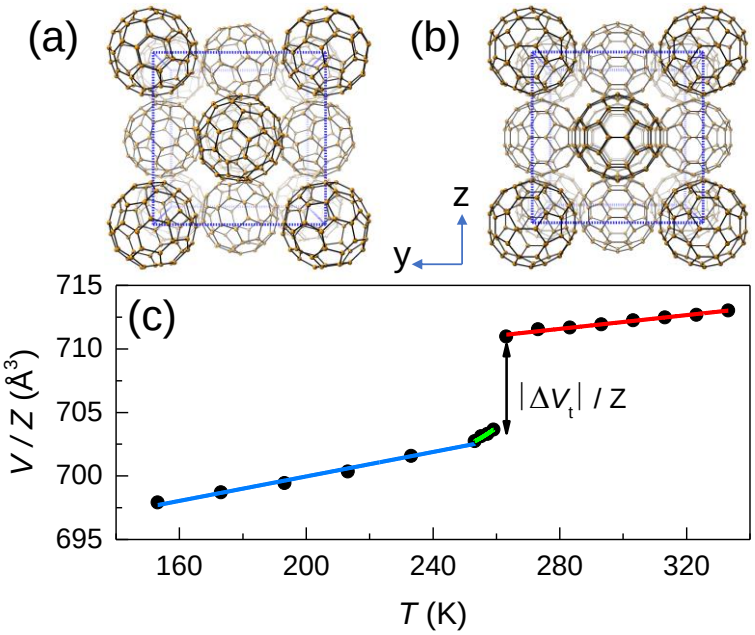

Figure 4.3. First-order phase transition in C_{60} at atmospheric pressure. (a) and (b) Unit cells of the low-temperature primitive cubic phase ($Pa\bar{3}$) and the high-temperature face-centred cubic phase ($Fm\bar{3}m$) respectively, generated from literature data. (c) Temperature-dependent unit cell volume per formula unit on heating. Error bars are smaller than the symbol size. The finite volume change per formula unit across the phase transition, $|\Delta V_t|/Z$, is indicated with a double arrow. Red and blue lines are linear fits to V(T) data above and well below the transition, respectively. The green line is a second-order polynomial fit to V(T) data at the pre-transitional regime.

At atmospheric pressure, the heat flow $dQ/|dT|$ converted from the differential scanning calorimetry (DSC) curve reveals that C_{60} undergoes a phase transition at 259 K on heating and 256 K on cooling, respectively, exhibiting a small hysteresis of 3 K [see Figure 4.4 (a)]. Integration of the calorimetric peaks yields a large latent of $\Delta H(p_{atm})$ = 6.9 ± 0.5 J g^{-1} on heating and $|\Delta H(p_{atm})|$ = 7.6 ± 0.5 J g^{-1} on cooling. In addition, integration of $(1/T)$ $(dQ/|dT|)$ allows the evaluation of entropy changes of this first-order phase transition, which are $\Delta S_t(p_{atm})$ = 26 ± 2 J K^{-1} kg^{-1} on heating and $|\Delta S_t(p_{atm})|$ = 27 ± 2 J K^{-1} kg^{-1} on cooling. These values are in overall agreement with previous values reported in the literature on powdered samples whereas single crystals usually give larger results, which are ascribed to the purity and crystallinity of the samples. On the other hand, in this compound the baseline chosen for integration in the low-temperature interval may be a source of significant uncertainty due to a smooth tail below the transition peak corresponding to the pre-transitional regime. In some studies, this tail is observed to extend more than 100 K below the first-order peak [115]. As our high-pressure calorimetry does not capture such a pre-transitional tail, we can associate the integrated values entirely with the first-order transition. Importantly, two exothermic peaks were observed on cooling [see Figure 4.4(b)]. This behaviour has been previously reported in the literature [116] and has been ascribed to the likely existence in the sc phase of two quasidegenerate orientational configurations that originate due to lattice impurities. The fact that this feature is visible only on cooling is probably due to hysteresis.

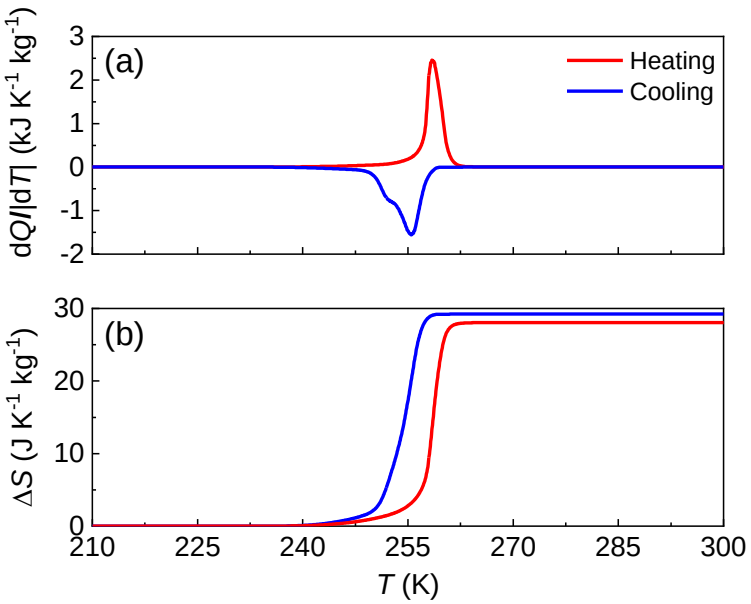

Figure 4.4. (a) Heat flow dQ/|dT| after baseline subtraction, on heating and cooling across the first-order phase transition. (b) Resulting entropy change with respect to the low-temperature phase, revealing the entropy changes for the first-order transition.

For C_{60}, the entropy change across the first-order phase transition ΔS_t originates from the volume change ΔS_V and from the partial ordering of the orientation of C_{60} molecules, ΔS_c, such that $\Delta S_t = \Delta S_V + \Delta S_c$. As for ΔS_V, it can be calculated taking into account that the entropy S is related to the Helmholtz free energy F *via* the thermodynamic relation $S = -(\partial F/\partial T)_V$. Considering the high-temperature phase as the unstrained phase, the volume-related entropy change $\Delta S_V = S_V(\text{fcc}) - S_V(\text{sc}) = -S_V(\text{sc}) = (\partial F_V(\text{sc})/\partial T)_V$. For a cubic system experiencing a pure dilatation, F_V can be expressed up to the harmonic approximation as

$$F_V = \frac{K}{2\rho}\left(\varepsilon_{xx} + \varepsilon_{yy} + \varepsilon_{zz}\right)^2 = \frac{K}{2\rho}\left(\frac{\Delta V_t}{V}\right)^2$$

where ε_{ii} are the diagonal terms of the Lagrangian strain tensor, $K = (C_{11} + 2C_{12})/3$ is the bulk modulus, with C_{ij} being the components of the stiffness tensor, $\Delta V_t/V$ is the relative volume change at the transition and ρ is the density. Therefore, ΔS_V can be expressed as

$$\Delta S_V = -\left(\frac{\partial F_V(sc)}{\partial T}\right)_V = -\frac{1}{2\rho}\left(\frac{\Delta V_t}{V}\right)^2\left(\frac{\partial K}{\partial T}\right)_V$$

Using $(\partial K/\partial T)_V = -0.04 \pm 0.02$ GPa K^{-1} from temperature-dependent elastic constants available in the literature [118] and $\rho = 1.70 \times 10^3$ kg m^{-3}, we obtain $\Delta S_V = 1.0 \pm 0.5$ J K^{-1} kg^{-1}, which is much smaller than the total transition entropy change. Interestingly, this indicates that the major contribution to the total transition entropy change comes from the partial ordering of molecular orientation, $\Delta S_c \sim 26$ J K^{-1} kg^{-1}. Then, we can estimate the ratio between the number of configurations achievable in the fcc phase (N_1) and in the sc phase (N_2) as $N_1/N_2 = \exp(MR^{-1}\Delta S_c) \sim 9.5$.

4.4 High-pressure thermodynamic properties and barocaloric effects

Through the use of high-pressure differential thermal analysers, isobaric temperature-dependent calorimetric signals under various pressures have been recorded. The raw experimental data along with the chosen baseline are shown in Figure B1 in Appendix B. Data including all the transition temperatures and entropy changes under various pressures are shown in Figure 4.5 (b) and (c). However, for better illustration, we only present and analyse part of the data for the BC study [see Figure 4.5 (a)].

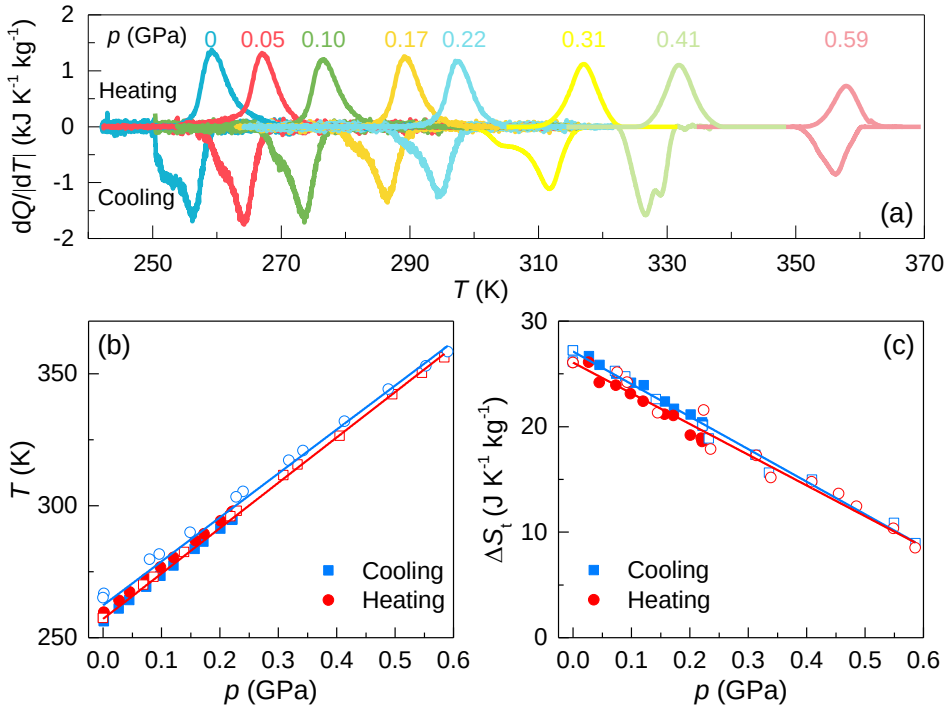

Figure 4.5. (a) Temperature-dependent isobaric heat flow dQ/|dT| at different pressures, after baseline subtraction. Selected curves shown below and above 0.3 GPa have been performed using calorimeters A and B, respectively. (b) Peak temperature and (c) entropy change across the phase transition ΔS_t as a function of pressure determined from both heating and cooling heat flow curves shown in panel (a). Solid and empty symbols stand for values obtained using calorimeters A and B, respectively. The lines are linear fits to data.

In Figure 4.5 (a), the peaks in dQ/|dT| associated with the first-order transition, which are positive for the sc → fcc transitions on heating (*i.e.* endothermic) and negative for the fcc → sc transitions on cooling (*i.e.* exothermic). We found that the difference between the endothermic and exothermic peak temperatures is small which suggests good reversibility for the BC effects. We also found that the isobaric calorimetric peaks shift to high temperatures with increasing pressure, which is shown in Fig. 4.5 (a). This is

qualitatively consistent with the positive ΔV_t on heating as established by the Clausius–Clapeyron equation $dT/dp = \Delta V_t/\Delta S_t$. Then we show the dependence of the peak temperatures with pressure in Fig. 5b. C_{60} shows constant $dT/dp = 167 \pm 3$ K GPa^{-1} on heating and $dT/dp = 172 \pm 2$ K GPa^{-1} on cooling within the pressure range under study, which are in agreement with literature values [101]. It is worth mentioning that the use of He as a pressure-transmitting medium in some studies gave rise to a much smaller dT/dp , which was associated with the easy penetration of He into the lattice. The large values for dT/dp in C_{60} in our study anticipate a reversible BC effect under low pressure and a giant working temperature span for BC cooling. The details will be discussed in the following section.

In Fig. 4.5 (c), we show the dependence of the entropy change with pressure from the integration of peaks in (1/T)(dQ/dT) at different pressures after baseline subtraction. We found that the transition entropy change decreases with pressure notably within the pressure range under study, as $d|\Delta S_t|/dp = -30 \pm 1$ J K^{-1} kg^{-1} GPa^{-1}, averaging over heating and cooling ramps. The reason for the decrease in entropy change with increasing pressure can be understood as follows: by including the value of $d|\Delta S_t|/dp$ in the Clausius–Clapeyron equation and taking into account that dT/dp does not depend on pressure, it can be derived that the first-order transition volume change also decreases with pressure as $d|\Delta V_t|/dp = (dT/dp)(d\Delta S_t/dp) = (-5.3 \pm 1.0) \times 10^{-6}$ m^3 kg^{-1} GPa^{-1}. The above results indicate a weakening of the first-order character of the transition when the pressure increases. This pressure-induced effect has also been observed and investigated by Lundin and co-workers [119]. Considering our results as well as those from previous work, it is worth mentioning here that C_{60} in our study does not undergo

polymerization nor amorphization processes. In present study, the temperature and pressure ranges used are much lower than the required temperature and pressure for the observation of the irreversible or polymerization processes in C_{60} solid. In addition, pressure values for our measurements have not been chosen to be monotonically increasing but nearly random just to ensure that the observed transitions at different pressures are thermodynamically reversible and do not depend on history.

For the calculation of the BC effects, the quasi-direct method including the construction of pressure-dependent heat capacity and temperature-dependent entropy curves were used as described in the Experimental methods section in Chapter 3. Figure 4.6 (a) shows the pressure-dependent heat capacity constructed from literature data at atmospheric pressure. The temperature-dependent isobaric entropy curves at different pressures are plotted in Figure 4.6 (b) and (c) for heating [$S_H(T, p)$] and cooling [$S_C(T, p)$], respectively, with respect to the reference entropy $S(T_0, p_{atm})$. Here, T_0 is selected as 150 K (see also in section 3.3, Chapter 3).

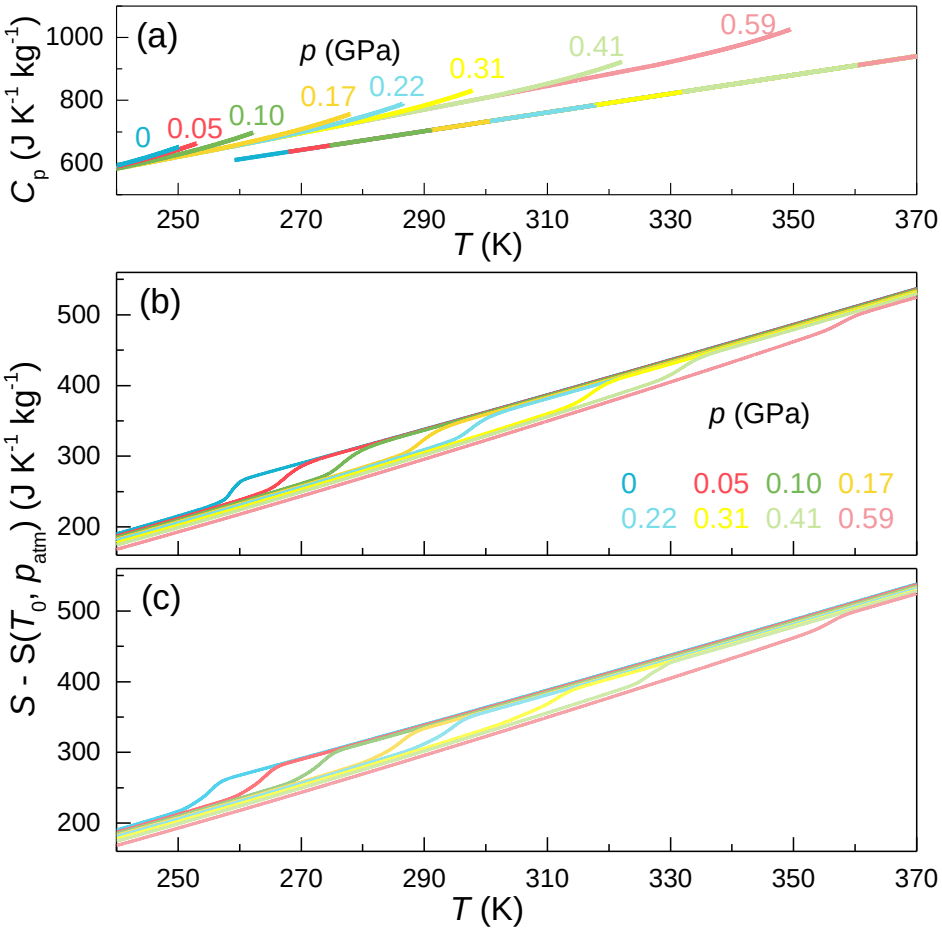

Figure 4.6. (a) Pressure-dependent heat capacity constructed from literature data at atmospheric pressure. For more details see the text. (b and c) Temperature-dependent isobaric entropy curves at different pressures on (b) heating and (c) cooling.

In particular, each corresponding plot includes $\Delta S_+(p)$ at 150 K and $p \sim 0$, as explained in Chapter 3. Notice that $\Delta S_+(p)$ was evaluated below the transition temperature at atmospheric pressure to avoid the forbidden possibility of the transition temperature rising to the temperature at which $\Delta S_+(p)$ was evaluated at high pressure. From Figure 4.6 (b) and (c), we can see that the entropy change associated with the

transition $\Delta S_0(p)$ combines with the same-sign additional entropy change $\Delta S_+(p)$ away from the transition, yielding total isothermal entropy change ΔS.

We now proceed to calculate the BC effects from the entropy–temperature curves determined in Figure 4.6 (b) and (c). Isothermal entropy changes are computed by subtracting $S(T, p)$ curves at different pressures following isothermal paths: $\Delta S(T, p_i \rightarrow p_f) = S(T, p_f) - S(T, p_i)$. Hereafter, the lower pressure is taken as atmospheric pressure p_i and the higher pressure as p_f, and therefore $|\Delta p| = |p_f - p_i| \simeq |p|$ for the high pressure values used here. In turn, adiabatic temperature changes are computed by subtracting the entropy–temperature curves following adiabatic paths: $\Delta T(T_s, p_i \rightarrow p_f) = T(S, p_f) - T(S, p_i)$, where ΔT is more appropriately plotted as a function of the starting temperature T_s. Since for a material with $dT/dp > 0$ decompressions are endothermic processes and compressions are exothermic processes, changes on first decompression are computed from entropy curves on heating whereas changes on first compression are computed from entropy curves on cooling. The corresponding results for ΔS and ΔT are shown in Figure 4.7 (a) and (b), respectively. It is worth pointing out here that from the entropy curves we can state that at low pressures the main contribution to ΔS originates from the transition entropy change ΔS_t. At high pressures ΔS_t decreases noticeably but additional entropy changes outside the transition ΔS_+ become very significant, reaching about ~50% of ΔS under a pressure change of $p = 0.59$ GPa.

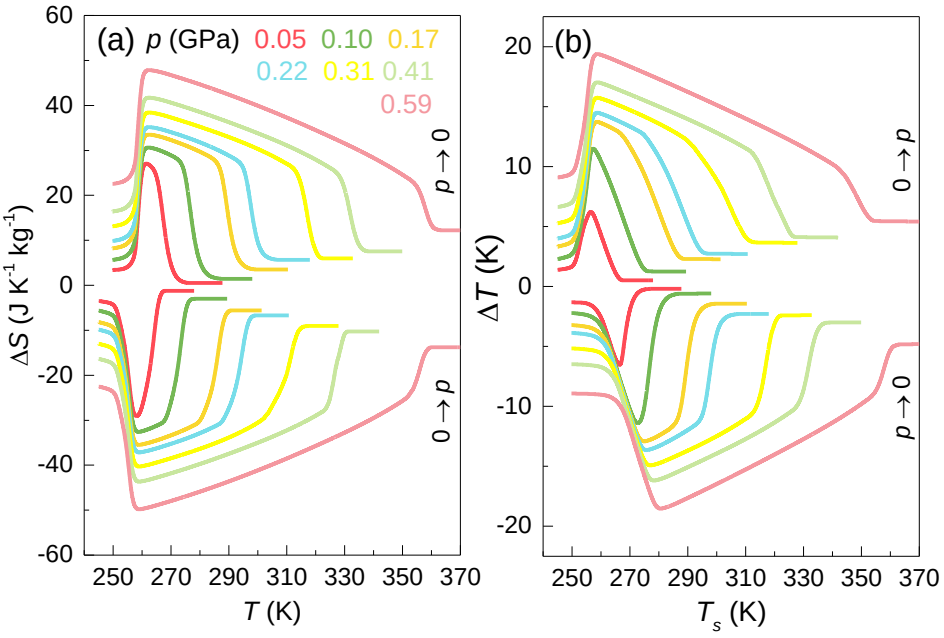

Figure 4.7. Barocaloric effects obtained on first application or removal of pressure. (a) Isothermal entropy changes on decompression and compression as a function of temperature at different pressures. (b) Adiabatic temperature changes on decompression and compression as a function of the starting temperature at different pressures.

As barocaloric cooling devices work in compression–decompression cycles, it is necessary for applications to determine the BC effects that occur when applying and removing pressure repeatedly. Given that compression processes end on cooling entropy curves at high pressure [$S_C(T, p)$] whereas decompression processes end on heating entropy curves at atmospheric pressure [$S_H(T, p_{atm})$], reversible BC effects are given by the difference between the entropy curves on cooling at high pressure and the entropy curve on heating at atmospheric pressure. Therefore, reversible ΔT is calculated as $|\Delta T_{rev}(p_{atm} \leftrightarrow p)| = |T(S_C, p) - T(S_H, p_{atm})|$. Obviously, this expression is only valid provided that the shift of the transition by application of pressure overcomes the

transition hysteresis, which establishes a lower threshold for the pressure change to obtain nonzero $|\Delta T_{\mathrm{rev}}|$, *i.e.* $p \geq p_{\mathrm{rev}}^{\Delta T}$. Nonetheless, it has been shown that a fraction of ΔS can be achieved reversibly (ΔS_{rev}) at $p_{\mathrm{rev}}^{\Delta S} < p_{\mathrm{rev}}^{\Delta T}$ due to the existence of minor loops allowed by partial transformation of the sample. Above this threshold pressure change, $\Delta S_{\mathrm{rev}}(T, p_{\mathrm{atm}} \leftrightarrow p)$ is determined as the overlap between $\Delta S(T)$ on compression and $\Delta S(T)$ on decompression. Using the procedure described elsewhere we obtain that for fullerite C_{60} across its sc $\rightarrow$ fcc transition, $p_{\mathrm{rev}}^{\Delta S} = 0$ and $p_{\mathrm{rev}}^{\Delta T} = 0.02 \pm 0.01$ GPa.

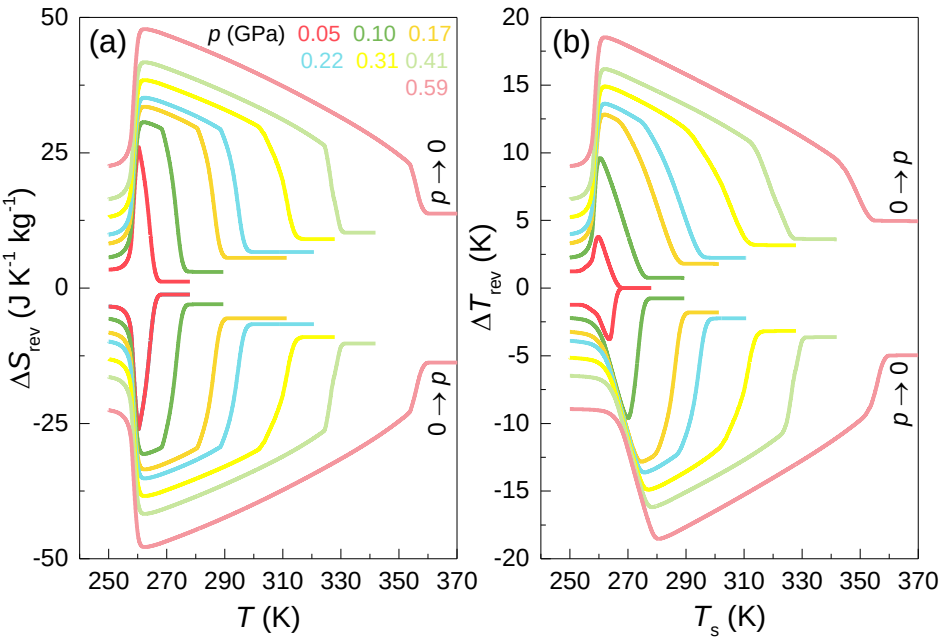

Figure 4.8. Reversible barocaloric effects. (a) Reversible isothermal entropy changes on decompression and compression as a function of temperature at different pressures. (b) Reversible adiabatic temperature changes on decompression and compression as a function of the starting temperature at different pressures.

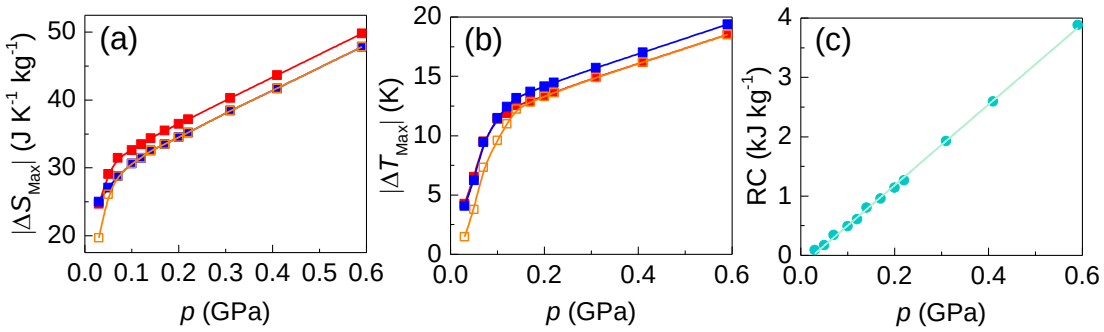

Figure 4.9. Maximum (a) isothermal entropy changes and (b) adiabatic temperature changes as a function of pressure change, on first decompression (red), on first compression (blue) and reversible values (orange). (c) Refrigerant capacity (RC) as a function of pressure.

From Figure 4.7 and 4.8, the maximum values of $|\Delta S|$, $|\Delta T|$, $|\Delta S_{rev}|$ and $|\Delta T_{rev}|$ as a function of pressure change are determined and shown in Figure 4.9 (a) and (b). Very interestingly, it can be observed that $|\Delta S_{rev}| > 0$ is obtained at any pressure change, as anticipated previously, and $|\Delta S_{rev}| = 25 \pm 3$ J K^{-1} kg^{-1} for $p = 0.05$ GPa and $|\Delta S_{rev}| = 32 \pm 3$ J K^{-1} kg^{-1} for $p = 0.1$ GPa can be reached. Larger values can be obtained at higher pressures. The area below the $|\Delta S_{rev}|$ *vs.* T curves gives an estimation of the Refrigerant Capacity (RC), which refers to the amount of heat that can be exchanged cyclically between hot and cold ends. Values for RC as a function of the pressure change are shown in Figure 4.9 (c). Under $p \approx 0.1$ GPa, we obtained giant BC effects of $|\Delta S_{rev}| \approx 32$ J K^{-1} kg^{-1} and $|\Delta T_{rev}| \approx 10$ K, with a RC ≈ 500 J kg^{-1}. These results suggest C_{60} as a very good BC cooling material.

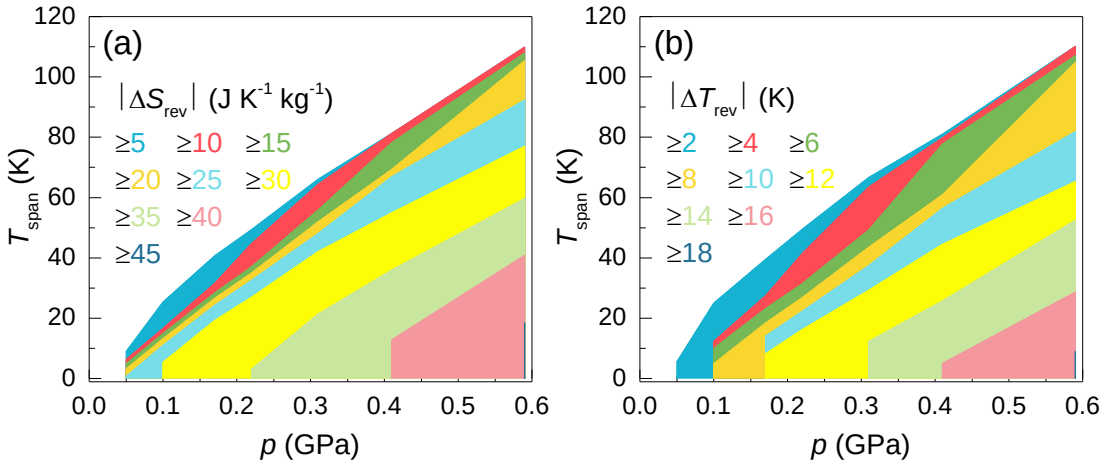

Figure 4.10. Temperature span as a function of applied pressure change for which different intervals of (a) reversible isothermal entropy changes and (b) reversible adiabatic temperature changes are obtained. For more details see the text.

Importantly, giant and reversible BC effects in C_{60} are obtained over a large temperature interval. In particular, Figure 4.10 shows the temperature span (T_{span}) as a function of the pressure range where an interval of ΔS_{rev} [panel (a)] and ΔT_{rev} [panel (b)] values can be achieved. At a given pressure change, the upper bound for T_{span} limiting each colour band corresponds to the minimum values of the BC effects indicated in the legend so that larger BC effects are obtained in a narrower T_{span} as expected. As examples, under a pressure change of $p \approx 0.1$ GPa, we obtain $|\Delta S_{rev}| \approx 25 \pm 3$ J K^{-1} kg^{-1} and $|\Delta T_{rev}| \approx 5.0 \pm 0.5$ K in a temperature interval of 11 K, and under a pressure change of $p \approx 0.41$ GPa, we obtain $|\Delta S_{rev}| \approx 31 \pm 3$ J K^{-1} kg^{-1} and $|\Delta T_{rev}| \approx 11 \pm 1$ K in a temperature interval of about 50 K. This excellent performance can be very useful in single-compound regenerative cooling methods, where heat sources and sinks are separated by large temperature spans by means of a regenerative heat exchanger.

4.5 Summary

In this chapter, the barocaloric behaviour of a crystalline powder of C_{60} was investigated by using isobaric calorimetry at high-pressure and X-ray diffraction measurements. The experimental results demonstrate giant isothermal entropy and adiabatic temperature changes at low pressures. This is mainly due to the partial ordering of molecular orientations across the first-order phase transition from face-centred-cubic to simple-cubic structure. In addition, the transition entropy change decreases with the increasing of pressure, but the isothermal entropy change still increases. This corresponds to the increase in additional changes arising outside the transition associated with the thermal expansion of each phase. Further, the obtained giant adiabatic temperature changes originate from a large sensitivity of the transition to pressure. This has been explained by applying the Clausius–Clapeyron relation where a very large transition volume change and giant transition entropy change can lead to a large value of $\mathrm{d}T/\mathrm{d}p$. In practice, this research demonstrates that the small hysteresis in C_{60} yields giant barocaloric effects that can be driven reversibly with very low pressures. Finally, the giant barocaloric effects in C_{60} are obtained over a very large temperature range, which can be very useful in single-component cooling methods using regeneration. The outcomes in this chapter indicate that C_{60} can be a promising candidate to be employed in future barocaloric cooling devices.

Chapter 5

Barocaloric effects in the layered hybrid perovskite $(C_{10}H_{21}NH_3)_2MnCl_4$

This chapter reports barocaloric effects in a layered hybrid organic-inorganic compound, $(C_{10}H_{21}NH_3)_2MnCl_4$, that are reversible and colossal under pressure changes below 0.1 GPa. This excellent barocaloric performance originates from a phase transition with a strong disordering of the organic chains and is unprecedented among solid-state cooling materials. At the same time, thanks to a very large sensitivity of the transition temperature to pressure and a small transition hysteresis, this colossal effect can be reversibly driven by low pressure. The result demonstrates that colossal effects can be obtained in materials other than plastic crystals. In addition, our experiments also demonstrate the existence of a triple point in the temperature-pressure phase diagram indicating enantiotropy at high pressure.

5.1 Layered hybrid organic-inorganic compounds

Over the past few decades, hybrid organic-inorganic perovskites (HOIPs) have earned

their credits in emerging semiconductor materials, especially for their successful application in photovoltaic cells [121]. In principle, HOIPs are identified as perovskites because these materials share similar structural features with the mineral $CaTiO_3$ named perovskite. A perovskite compound with general chemical formula ABX_3 shows a cubic structure with the B cation in 6-fold coordination, surrounded by an octahedron of anions, and the A cation in 12-fold cuboctahedral coordination (see Figure 5.1). It is to be noted that HOIPs perovskite structure with A = Cs^+, $CH_3NH_3^+$, and $[HC(NH_2)_2]^+$ are generally three-dimensional (3D) materials. However, by introducing large organic cations, there would be a dimensional reduction in the 3D crystal lattice [121].

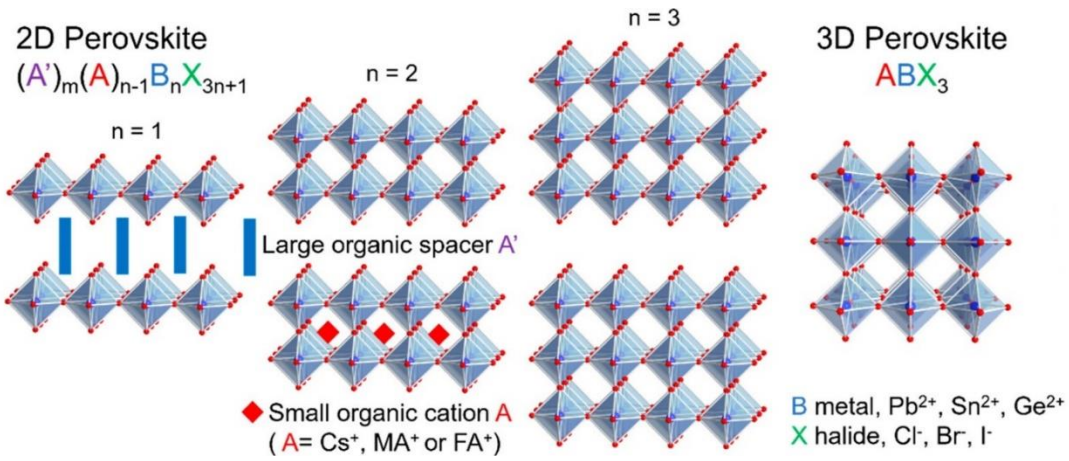

Figure 5.1. A structural schematic of two-dimensional and three-dimensional hybrid perovskite with key chemical components. (Reproduced from Ref. 121)

In fact, these reduced structures are recognized as 2-dimensional (2D) or layered HOIPs. In Figure 5.1, one can see that 2D HOIPs exhibit a perovskite-like structure

with reduced dimensionality where BX_6 octahedra sharing their corners only between neighbours in the planes of inorganic layers. For a better description, we use $(C_{10}H_{21}NH_3)_2MnCl_4$ as a case study. In the layered structure, there are two chains of alkylammonium $C_{10}H_{21}NH_3^+$ cations arranged along the *c* direction between the inorganic planes. Importantly, large organic cations prevent the 3D corner-sharing along the *c*-axis between octahedra belonging to different inorganic layers, and therefore, the actual structure of true perovskites cannot be arranged [121,122]. At the end of these long organic chains, electrostatic force and hydrogen bonds between ammonium and $MnCl_6$ make sure that the organic parts are stably aligned toward the inorganic octahedra. On the other hand, the organic chain tails facing each other are stabilized by their van der Waals interactions [123,124].

Thanks to their special structures, these materials always display abundant phases as a function of temperature at atmospheric pressure. For instance, DSC study has shown that these compounds normally exhibit a sequential order of two or more phase transitions with one showing significantly larger latent heat than the others [125-127]. This phenomenon has been well investigated by using X-ray diffraction, Fourier-transform infrared and Raman spectroscopic techniques [126,128]. For the significant or major transition, the origin of large latent heat comes from the chain-melting process during the phase transition. During this melting process, the organic chains show conformational disorders on account of the energetic rotation of the alkyl bonds [128]. Meanwhile, the polar head group of the chain remains ionically bonded to the inorganic part. Therefore, this conformational disorder tends to reduce the length of the chains. However, this reduction is compensated for by increasing the distance between the ends

of the facing organic chains. As a result, a significant volume change is achieved during the chain-melting, and also a large latent heat. In contrast, the minor transition is an order-disorder one that corresponds to the chain orientation process. Specifically, the organic chains rotate around the longitudinal chain axis between two equivalent orientations separated by 90°. At the same time, the neighbouring chains rotate in opposite directions. Although the entropy change that comes from this process is not huge, this value is still giant compared with most barocaloric materials.

Another important feature of 2D HOIPs is that their properties can be modified by tuning the inorganic layers and the organic cations [129]. For example, one can easily modify the transition temperatures by increasing the chain length. In $(C_nH_{2n+1}NH_3)_2MnCl_4$, the transition temperature varies from 287 K to 373 K when n = 9 increases to n = 17. In addition, their mechanical properties can be modified by replacing the inorganic elements or increasing the layer numbers [121]. Therefore, these features can offer a range of mechanical soft materials with caloric effects near room temperature [130].

Very recently, barocaloric studies on HOIPs [131] and spin-crossover compounds [132] have revealed large reversible effects at moderate pressures within large temperature spans. Although a colossal effect in those materials has not been reported, their chemical flexibility and property tunability provide us with a chance to find candidates showing colossal effects. In particular, as a subfamily of HOIPs, layered perovskites with the chemical formula $(C_nH_{2n+1}NH_3)_2MCl_4$ (with M being a divalent metal) have been widely investigated thanks to their rich composition and structural variety properties. In the 1970s, researchers investigated these compounds as phase change

materials for thermal energy storage applications [127]. As in the case of plastic crystals [133], this functionality emerges due to the occurrence of highly energetic, fully reversible first-order phase transitions with suitable transition temperatures. This feature, along with a large transition volume change, suggests that these compounds could be very suitable as barocaloric agents, as plastic crystals have already shown. It is worth noting that compounds with M = Mn, Fe (and other very similar compounds), awakened further interest due to their low-dimensional magnetic properties [134-136] whereas multicaloric effects are being investigated in magnetostructural materials showing similar properties [41,42].

In contrast to the orientational disorder facilitated by globular or small molecules in plastic crystals [24,25,137], $(C_nH_{2n+1}NH_3)_2MCl_4$ compounds exhibit more complex structure and dynamical disorder. In this work, we choose the compound $(C_{10}H_{21}NH_3)_2MnCl_4$ [n=10, bis(alkylammonium) tetrachloromanganate(II), $C_{10}Mn$ for short] because in this material the disorder fully develops across a single phase transition and near room temperature and therefore exhibits a larger transition entropy change than compounds with larger *n* values.

5.2 Sample preparation and structural information

The polycrystalline $(C_{10}H_{21}NH_3)_2MnCl_4$ sample were synthesized through the following reaction:

$$2(C_{10}H_{21}NH_2) + 2HCl + MnCl_2 \rightarrow (C_{10}H_{21}NH_3)_2MnCl_4.$$

Manganese(II) chloride tetrahydrate ($MnCl_2 \cdot 4H_2O$, 99%, Sigma-Aldrich) was added

into hydrochloric acid (HCl, 36.5–38.0%, Baker Analyzed) with magnetic stirring until $MnCl_2 \cdot 4H_2O$ was fully dissolved. Then, n-decylamine ($C_{10}H_{21}NH_2$, 99%, ACROS Organics) was added into this mixed solution with magnetic stirring for 3 hours. Then, $(C_{10}H_{21}NH_3)_2MnCl_4$ powder was obtained by precipitation and washed with ethanol twice. The synthetic yield of the reaction is 90%. However, the as-prepared power sample needs to be washed and recrystallized from ethanol. After that we can get our polycrystalline samples. The yield of the recrystallizing step is 80% which depends on the cooling speed but controllable. Thus, if we consider the multi-step reaction, the total yield of the our compound is *total yield* (%) = (0.9*0.8)*100 = 72%.

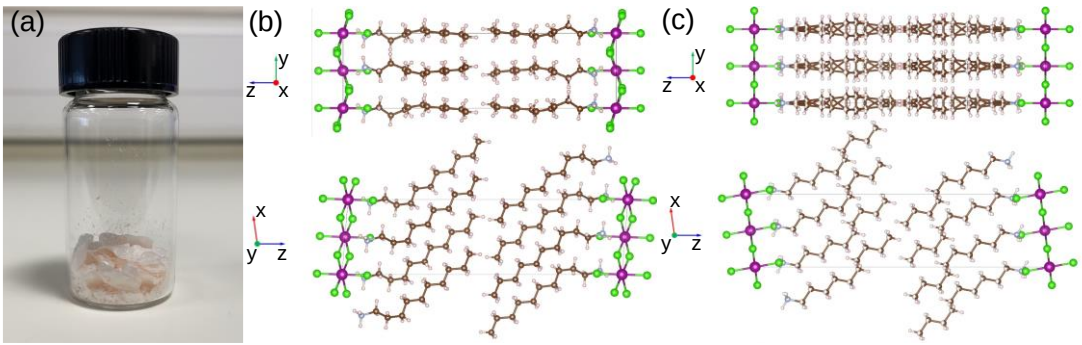

Figure 5.2. (a) Picture of the as prepared sample of $(C_{10}H_{21}NH_3)_2MnCl_4$ showing pale pink colour. The crystal structure of the low-temperature phase $P2_1/a$ (b) and high-temperature phase $C2/m$ (c) projected on the (100) and (010) planes, respectively. Purple, green, grey, brown and white spheres stand for Cl, Mn, N, C and H atoms.

The as-prepared sample is shown in Figure 5.2 (a). The compound has shown to be thermally stable for several years after synthesis, being stored. The thermodynamic transition properties are not modified after thermal cycling across the first-order phase

transition at different pressures applied randomly. In this sense, our observations are fully consistent with the findings in Ref. 138 where the thermal stability of $(C_{10}H_{21}NH_3)_2MnCl_4$ was specifically investigated.

The structure of $C_{10}Mn$ was characterized by using X-ray powder diffraction (XRPD) and Raman Spectroscopy measurements at atmospheric pressure and at temperatures around its solid-to-solid first-order phase transition. Raman spectra were obtained by using an IK Series Raman spectroscopy system. A 532 nm He–Cd laser was used for excitation. A calibrated Linkam heating–cooling stage was utilized to control sample temperature, via a thermocouple attached to the sample holder.

The diffraction patterns of the low-temperature phase at 295 K and of the high-temperature phase at 330 K were refined by means of a Rietveld refinement procedure [139] using TOPAS-Academic v.7 [140]. At low temperatures, a $P2_1/a$ (with $Z = 2$ formula units per unit cell) structure (cif number: CCDC 2096682) was obtained [see Figure 5.2 (b)], consistent with that reported in ref. [141], and in disagreement with the orthorhombic structure reported in ref. [123]. For the high-temperature phase, which was previously undetermined, a $C2/m$ (with $Z = 2$ formula units per unit cell) structure [see Figure 5.2 (c)] was obtained (cif number: CCDC 2096683). From these refinements, pattern matching of the temperature dependent XRPD patterns was performed, to obtain the unit cell volume as a function of temperature $V(T)$. A thorough explanation of the refinement details, the crystallographic structures of the unit cell in the two phases and the dependence of the patterns and the lattice parameters on temperature can be found in Figure A2-A5 in Appendix A.

5.3 Thermodynamic properties of $(C_{10}H_{21}NH_3)_2MnCl_4$ at atmospheric pressure

The results at atmospheric pressure confirmed the first-order phase transition at around $T \sim 309$ K [see Figure 5.3 (a) and (b)]. The unit cell volume plot in Figure 5.3 (a) revealed a very large increase in volume at the endothermic transition of $\Delta V/V_{II} \approx 7\%$. Both above and well below ($T < 309$ K) the transition, $V(T)$ shows a linear behaviour as indicated by the red linear fits, whereas below but close to the first-order transition (293–309 K), $V(T)$ shows a nonlinear behaviour as indicated by the second-order polynomial fit (green solid line). This nonlinear $V(T)$ regime can be associated with a pre-transitional regime.

Isobaric temperature-dependent calorimetry at atmospheric pressure yielded positive and negative peaks in $dQ/|dT|$ associated with endothermic and exothermic first-order phase transitions, respectively [see Figure 5.3 (b)]. The maxima of the peaks were obtained at $T_{II\rightarrow I} = 312 \pm 1$ K and $T_{I\rightarrow II} = 303 \pm 1$ K, whereas the onsets of the peaks were obtained at $T_{II\rightarrow I} = 309 \pm 1$ K and $T_{I\rightarrow II} = 306 \pm 1$ K. These values indicate a hysteresis of 9 K as defined from the peak maxima, and 3 K as defined from the peak onsets, which are both small.

Integration over temperature of $dQ/|dT|$ and $(1/T)dQ/|dT|$ after baseline subtraction yielded transition enthalpy changes $\Delta H_{II\rightarrow I} = 76 \pm 4$ J g^{-1} and $\Delta H_{I\rightarrow II} = 79 \pm 4$ J g^{-1} and transition entropy changes $\Delta S_{II\rightarrow I} = 241 \pm 12$ J K^{-1} kg^{-1} and $\Delta S_{I\rightarrow II} = 261 \pm 13$ J K^{-1} kg^{-1}, in very good agreement with the literature [141,142]. The integrated curve for ΔS_t

was used with the temperature-dependent heat capacity *c* obtained from modulated calorimetry [see Figure 5.3 (c)] to calculate the temperature-dependent entropy with respect to a reference temperature T_0 = 213 K (chosen arbitrarily below the transition) as $S(T, p_{atm}) - S(T_0, p_{atm}) = \int_{T_0}^{T} \frac{1}{T}\left(C_p + dQ/dT\right)dT$ [see Figure 5.3 (d)]. In this compound the baseline chosen for integration in the low-temperature interval may be a source of significant uncertainty due to a smooth tail below the transition peak corresponding to the pre-transitional regime. However, it shows a short tail compared to that observed for C_{60}. By using the methods in Chapter 3, we calculated and plotted the temperature- and pressure-dependent entropy. Again, as our high-pressure calorimetry does not capture such a pre-transitional tail, we can associate the integrated values entirely with the first-order transition.

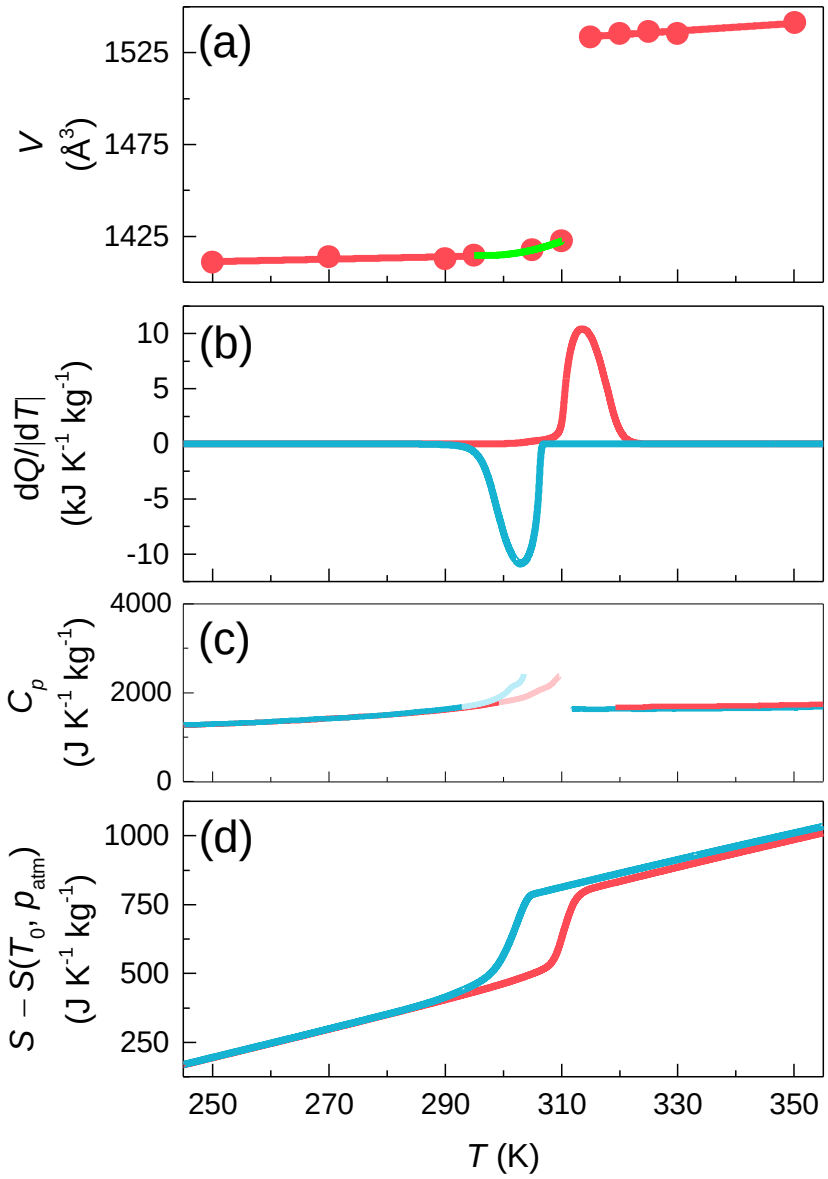

Figure 5.3. (a) Unit cell volume as a function of temperature at atmospheric pressure. Red lines are linear fits to $V(T)$ data above and well below the transition, respectively. The green solid line is a second-order polynomial fit to $V(T)$ data at the pre-transitional regime. (b) heat flow in temperature (exothermic down), (c) specific heat capacity, and (d) entropy as a function of temperature at atmospheric pressure. Red and blue curves correspond to data obtained on heating and on cooling, respectively. The heat capacity data with light colours corresponds to the pre-transitional regime.

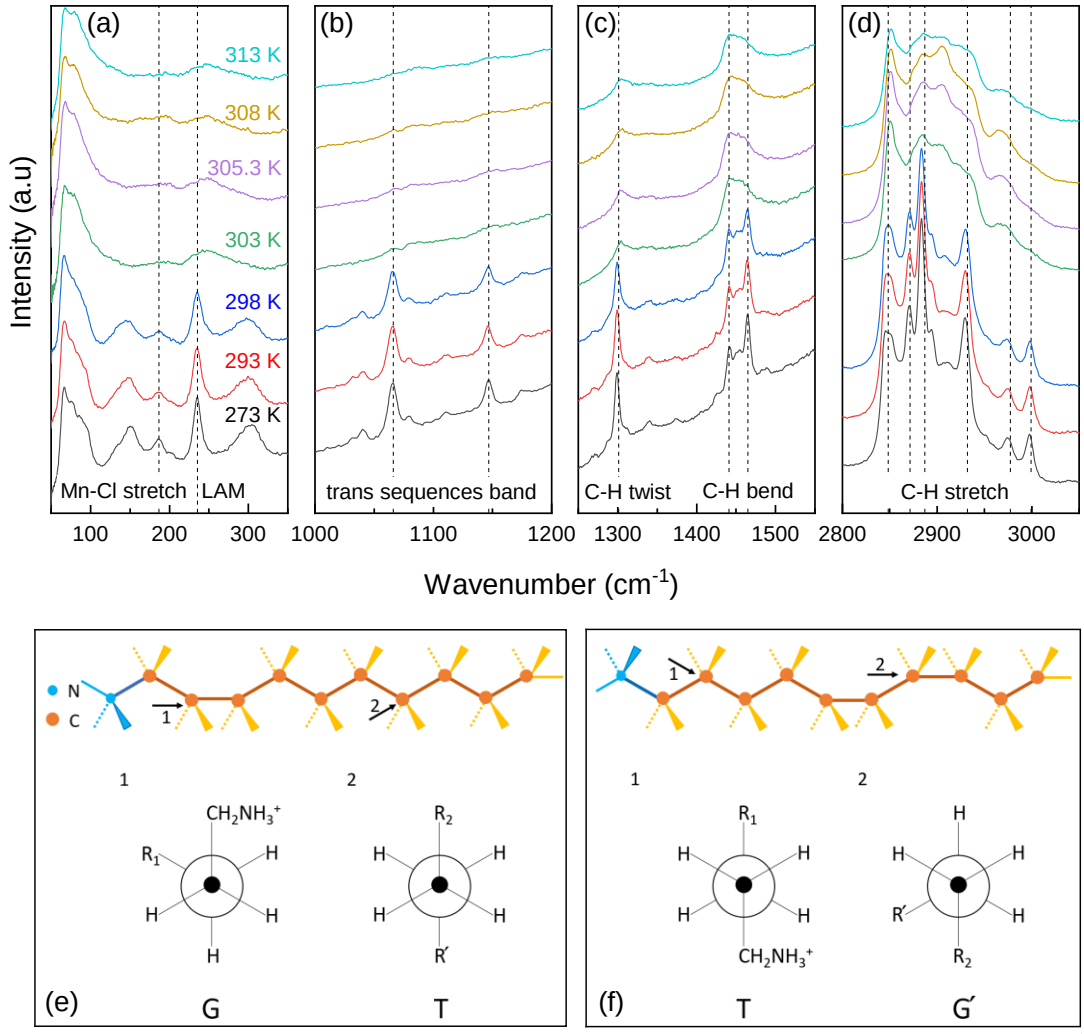

Figure 5.4. (a–d) Temperature dependence of the Raman spectrum of $(C_{10}H_{21}NH_3)_2MnCl_4$ at different wave number intervals. (e,f) Schematic diagram for the probable conformation of the decylammonium chain under low and high temperature respectively, along with Newman projections for trans (T) and gauche (G) conformations corresponding to the positions indicated by numbers 1 and 2. R_1 stands for $-CH_2-CH_2-CH_2-CH_2-CH_2-CH_2-CH_3$. R_2 stands for $-CH_2-CH_2-CH_2-CH_2-CH_2-CH_2-NH_3^+$. R' stands for $-CH_2-CH_3$.

To understand the origin of such large entropy changes at the transition, we investigated the molecular disordering process by temperature-dependent Raman scattering at both low and high wavenumbers. Previous Raman studies on organic chains have described a peak at low frequency as corresponding to an accordion-like longitudinal acoustic mode (LAM) [143-145]. In our measurements, such a peak is obtained in the low temperature phase near 235 cm^{-1} [see Figure 5.4 (a)]. In particular, this is higher than the value for all-trans (T) chain (209 cm^{-1}) or for chains of the same length engaged in hydrogen bonds, such as n-decylamine (213 cm^{-1}) or decylammonium chloride (217 cm^{-1}) [146], and corresponds to a conformational effect and the existence of a gauche (G) conformation near the NH_3 polar head. In Figure 5.4 (b), the characteristic bands of the trans planar chains are observed at 1065, 1109, 1146 and 1174 cm^{-1}. This indicates that the most intense bands in the Raman spectrum of the long alkyl chains correspond to the limiting $k = 0$ modes of an infinite chain [147]. Figure 5.4 (c) and (d) shows the characteristic bands of the C–H twisting (1300 cm^{-1}), bending (1420–1480 cm^{-1}) and stretching (2830–3000 cm^{-1}) mode. It is worth noting that the scattering wing on the 2846 cm^{-1} line is due to intermolecular forces [147]. Moreover, the Mn–Cl stretching mode band can be found at 186 and 236 cm^{-1} (overlapped with LAM at 235 cm^{-1}) and wavenumbers 300, 1040, and 1080 cm^{-1} correspond to the NH_3 torsional band (overlapped with the trans bond stretching at 300 cm^{-1}) [148,149]. Overall, the low-temperature study of these spectral regions indicates a typical ordered state of the low-temperature phase and gives further evidence for the existence of inter- and intramolecular coupling in an almost completely extended chain.

In the high-temperature phase, the Raman spectra indicate the emergence of disorder.

First, the LAM mode and the limiting k = 0 mode bands disappear and only a broad and weak band is observed near 247 cm^{-1}, which means that the conformation of the long trans planar chains is changed. Further evidence of appearing of the gauche bond structure can be found in the decrease of the 1465 cm^{-1} shoulder, which is due to intramolecular coupling of trans structures [147,149]. In order to fully understand the structure of the organic part, we schematically show the probable conformation of the decylammonium chain as reported in the literature from infrared spectra [141] and incoherent neutron scattering [150]. In Figure 5.4 (e) and (f), we can see that the conformation for low temperature is T-G-T-T-T-T-T-T while the high temperature becomes T-T-T-T-G-T-G'-T. As discussed previously, it is believed that the reorientation of the whole chain and the disorder of the hydrocarbon parts come from the increase of the G and G' conformations which is regarded as conformational disorder and contributes a large latent heat in the order–disorder first-order phase transition. Furthermore, the C–H stretching mode bands at 2870, 2883, and 2930 cm^{-1} merge into a broad peak, indicating that the intermolecular forces are greatly changed. Finally, the Mn–Cl stretching mode bands become weak and broad at high temperature with the disappearing of the NH_3 torsional mode band. This means a dramatic change for the layer, which is consistent with the increase of the c-axis length from the XRPD data.

5.4 High-pressure thermodynamic properties and barocaloric effects

Through the use of high-pressure differential thermal analysers, isobaric temperature-

dependent calorimetric signals under various pressures were recorded. The raw experimental data along with the chosen baseline are shown in Figure B2 in Appendix B. Data including all the transition temperatures and entropy changes under various pressures are shown in Figure 5.5 and 5.6. However, for better illustration, we only present and analyse part of the data for the BC study.

Figure 5.5 shows the isobaric temperature-dependent heat flow $dQ/|dT|$ data performed at different pressures using Calorimeter A and Calorimeter B. As can be seen from Figure 5.5, the heat flow curves below 0.1 GPa reveal single peaks associated with the II↔I transition (see Figure 5.6) which shifts strongly to higher temperatures with increasing pressure. Above 0.18 GPa, both exothermic and endothermic calorimetric signals clearly exhibit two consecutive peaks which indicate the appearance of a new phase (III) between the two peaks. The larger peak corresponds to the transition II→III and is followed by the smaller peak corresponding to the transition III→I. The exothermic transitions show peak splitting at lower pressures. Two possible causes are: *i*) the occurrence of transitions between equilibrium phases, I-III-II, but with different hysteresis (i.e., a larger thermal hysteresis of the transition III→II than that of the transition I→II), for which the peak splitting can be more easily identified in exothermic peaks than in endothermic peaks because in the latter the overlap of the very close peaks prevents distinguishing them; *ii*) the occurrence of a metastable phase transition from the equilibrium phase I to the metastable phase III at temperatures and pressures below the triple point in equilibrium, followed by a phase transition from the metastable phase III to the stable phase II. Or a combination of (i) and (ii) is possible.

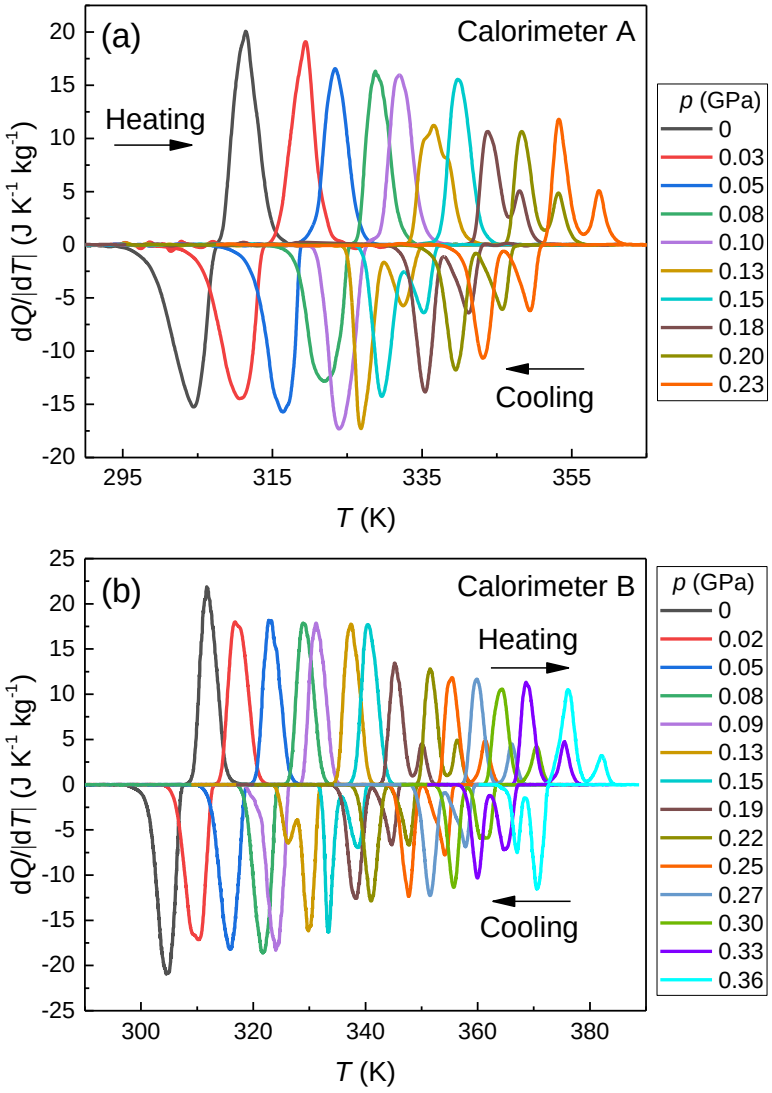

Figure 5.5. Isobaric heat flow dQ/|dT| as a function of temperature at different applied pressures on heating (positive peaks) and on cooling (negative peaks). (a) for Calorimeter A and (b) for Calorimeter B.

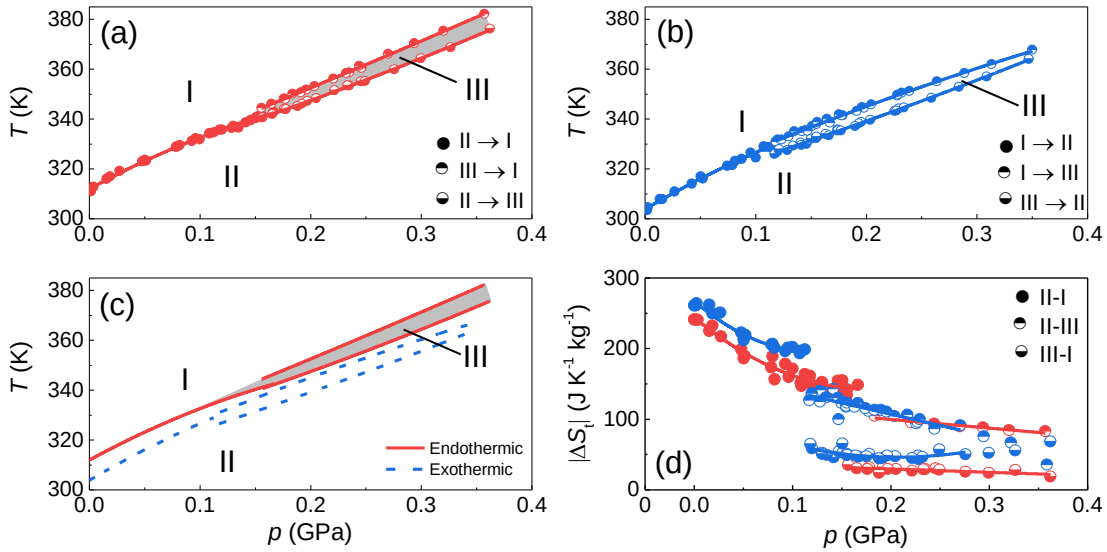

Figure 5.6. Transition temperatures as a function of pressure determined as the maximum of the peaks. For the sake of clarity, endothermic (a) and exothermic (b) data are shown separately. Panel (c) shows the fits for both endothermic and exothermic transitions. Shadowed areas show the equilibrium region for phase III. d) Transition entropy change as a function of the applied pressure, for the endothermic (red) and exothermic (blue) transitions. Filled symbols, top-half filled symbols and bottom-half filled symbols stand for II↔I, III↔I and II↔III transitions, respectively. Lines are fits to data.

Figure 5.6. presents the transition temperatures as a function of pressure determined as the maximum of the peaks from isobaric heat flow curves under constant pressures. For the single peaks associated with the II↔I transition, the pressure-dependent transition temperatures can be fitted by slightly convex second-order polynomials, yielding $dT_{\mathrm{II}\rightarrow\mathrm{I}}/dp$ = 250 ± 6 K GPa^{-1} and $dT_{\mathrm{I}\rightarrow\mathrm{II}}/dp$ = 280 ± 20 K GPa^{-1} for the endothermic and exothermic transitions, respectively [see Figure 5.6 (a) and (b)]. For heat flow

curves showing two peaks, the striking similarity between the dT/dp values of the different coexistence lines ($dT_{II \rightarrow III}/dp = 180 \pm 1$ K GPa^{-1}, $dT_{III \rightarrow II}/dp = 161 \pm 2$ K GPa^{-1}, $dT_{III \rightarrow I}/dp = 170 \pm 2$ K GPa^{-1}, $dT_{I \rightarrow III}/dp = 160 \pm 3$ K GPa^{-1}) makes it even more difficult to determine the actual cause. Moreover, this behaviour prevents an accurate determination of the coordinates of the triple point where phases I, II, and III coexist in equilibrium, (T_{tp}, p_{tp}), as cause (*i*) would lead the triple point to be at (~330 K, ~0.12 GPa) whereas cause (*ii*) would lead the triple point to be closer to (~337 K, ~0.14 GPa). On the other hand, notice that at the highest applied pressure $p = 0.36$ GPa the exothermic peaks are observed in the reverse order, with first the larger peak followed by the smaller peak. This behaviour can only be explained if part of the material undergoes a phase transition from stable phase I towards a metastable phase II, which on further cooling becomes stable, while the rest of the material undergoes the transition sequence between stable phases I→III→II.

Integration of the peaks in $(1/T)(dQ/|dT|)$ at different pressures reveals that the transition entropy change decays significantly with increasing pressure, at a rate of ~−1.1 × 10^3 J K^{-1} kg^{-1} GPa^{-1} [see Figure 5.6 (d)]. Close to the triple point (p ~0.15 GPa), we obtained $\Delta S_{II \rightarrow I} = 144 \pm 14$ J K^{-1} kg^{-1}, $\Delta S_{II \rightarrow III} = 102 \pm 10$ J K^{-1} kg^{-1} and $\Delta S_{III \rightarrow I} = 32 \pm 4$ J K^{-1} kg^{-1}. For the exothermic transitions we obtained $\Delta S_{II \rightarrow I} = 196 \pm 20$ J K^{-1} kg^{-1}, $\Delta S_{II \rightarrow III} = 134 \pm 14$ J K^{-1} kg^{-1} and $\Delta S_{III \rightarrow I} = 60 \pm 6$ J K^{-1} kg^{-1}. Notice that these values are consistent with the thermodynamic requirement at the triple point $\Delta S_{II \rightarrow I} \approx \Delta S_{II \rightarrow III} + \Delta S_{III \rightarrow I}$. By comparison with the transition sequence exhibited by other compounds of the same family at atmospheric pressure [125-127], and given that

$\Delta S_{II \rightarrow III}$ is significantly larger than $\Delta S_{III \rightarrow I}$, we expect that above the triple point the II→III transition is the major transition involving the chain melting whereas the III→I transition corresponds to the minor transition of the order–disorder type. On the other hand, given the inverse transition order obtained on cooling in a very few cases, to avoid any inconsistency in the determination of $\Delta S_{I \rightarrow III}$ and $\Delta S_{III \rightarrow II}$, we have omitted the integration values at high pressure when performing the fits to the data displayed in Figure 5.6 (d) and when determining the BC effects. Also, it is worth noticing that the joint integration of the two peaks shows a smooth and monotonic behaviour regardless of the transition order. This strongly indicates that the transitions order does not affect the thermodynamic properties associated with the overall transition path I→II.

To calculate the barocaloric effect via the quasi-direct method, the isobaric entropy as a function of temperature and for different pressures, $S(T, p)$ was obtained with respect to a reference taken at temperature T_0 and atmospheric pressure including the construction of pressure-dependent heat capacity and temperature-dependent entropy curves have been explained in the Experimental methods section in Chapter 3. It is to be noted that the temperature dependence of c in the transition temperature interval was estimated as a weighted average of the two phases I and II, that is $c(T', p) = (1 - x)c_{II}(T', \mathrm{p}) + xc_{I}(T', p)$, where $x(T, p)$ is the fraction of the system in phase I and is computed using the normalized cumulative integral for the transition entropy change. The former expression is also used for pressures above the triple point, where the c of phase III is experimentally inaccessible. However, given the very narrow temperature range of stability of this phase, the error introduced in the entropy due to this approxim-

ation is expected to be insignificant.

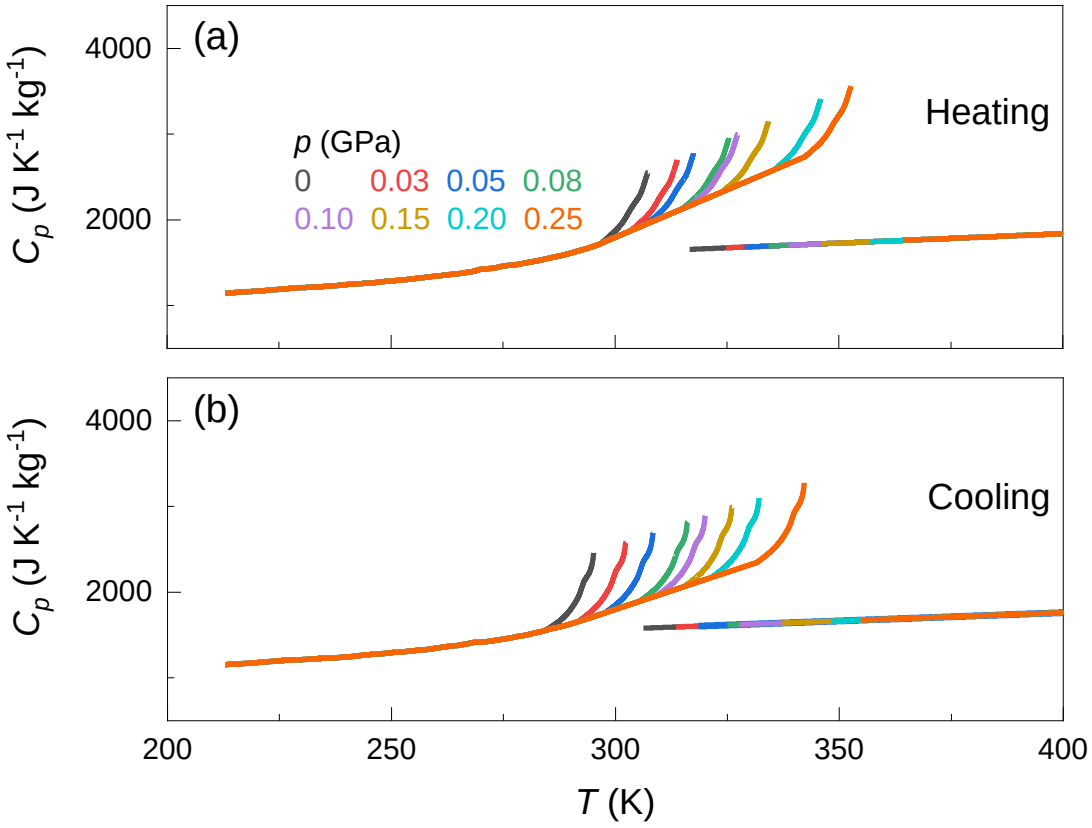

Figure 5.7. Heat capacity as a function of temperature at different pressures for heating (a) and cooling (b), constructed from heat capacity at atmospheric pressure shown in Figure 5.3 (c) and volume-temperature data as explained in the manuscript.

The pressure dependence of c was evaluated from the temperature dependence of volume by means of the thermodynamic relation $\left(\frac{\partial C_p}{\partial p}\right)_T = -T\left(\frac{\partial^2 V}{\partial T^2}\right)_p$. According to our data, $V(T)$ is approximately linear in phase II below ≈ 295 K and in phase I in the measured interval [see red linear fit in Figure 5.3 (a)], indicating that c is independent

of pressure in these temperature intervals. Recent XRPD measurements performed during isobaric cooling in $C_{10}Mn$ have directly confirmed this independent behaviour by showing temperature dependence of specific volume across the transition [151]. Details have been discussed in Chapter 3. Instead, $V(T)$ is nonlinear in the temperature interval from 295 to 310 K [see green line in Figure 5.3 (a)], indicating a pressure dependence of c in this temperature interval [see lines with light colours in Figure 5.3 (c)]. Moreover, as the transition temperature increases with pressure, these c features must be translated to higher temperatures with increasing pressure by an amount $(dT/dp)(p - p_{atm})$. Calculated $c(T, p)$ curves are shown in Figure 5.7. A detailed explanation of the procedure for the construction of the $C_p(T, p)$ curves can be found in Chapter 3.

Based on the temperature- and pressure-dependent heat capacity and pressure-dependent heat flow curves, the temperature- and pressure-dependent $S(T, p)$ curves were constructed. The resulting functions $S(T, p) - S(T_0, p_{atm})$ are shown in Figure 5.8 (a) and (b) for selected pressures. Notice that $\Delta S_+(p)$ was evaluated below the transition temperature at atmospheric pressure to avoid the forbidden possibility of the transition temperature rising to the temperature at which $\Delta S_+(p)$ was evaluated at high pressure. The calculated $\Delta S_+(p)$ in our testing range is relatively small which corresponds to the very small $\left(\frac{\partial V}{\partial T}\right)_{p_{atm}}$ value obtained from the $V(T)$ curves as shown in Figure 5.3 (a). From Figure 5.8 (a) and (b), one can see that the entropy change associated with the transition combines with the same-sign additional entropy change $\Delta S_+(p)$ away from the transition, yielding a total entropy change $\Delta S(p)$. Due to the rapid decrease of the

transition entropy under higher pressure, the constructed curves show a gap at high temperature. We carefully include error in the following discussion.

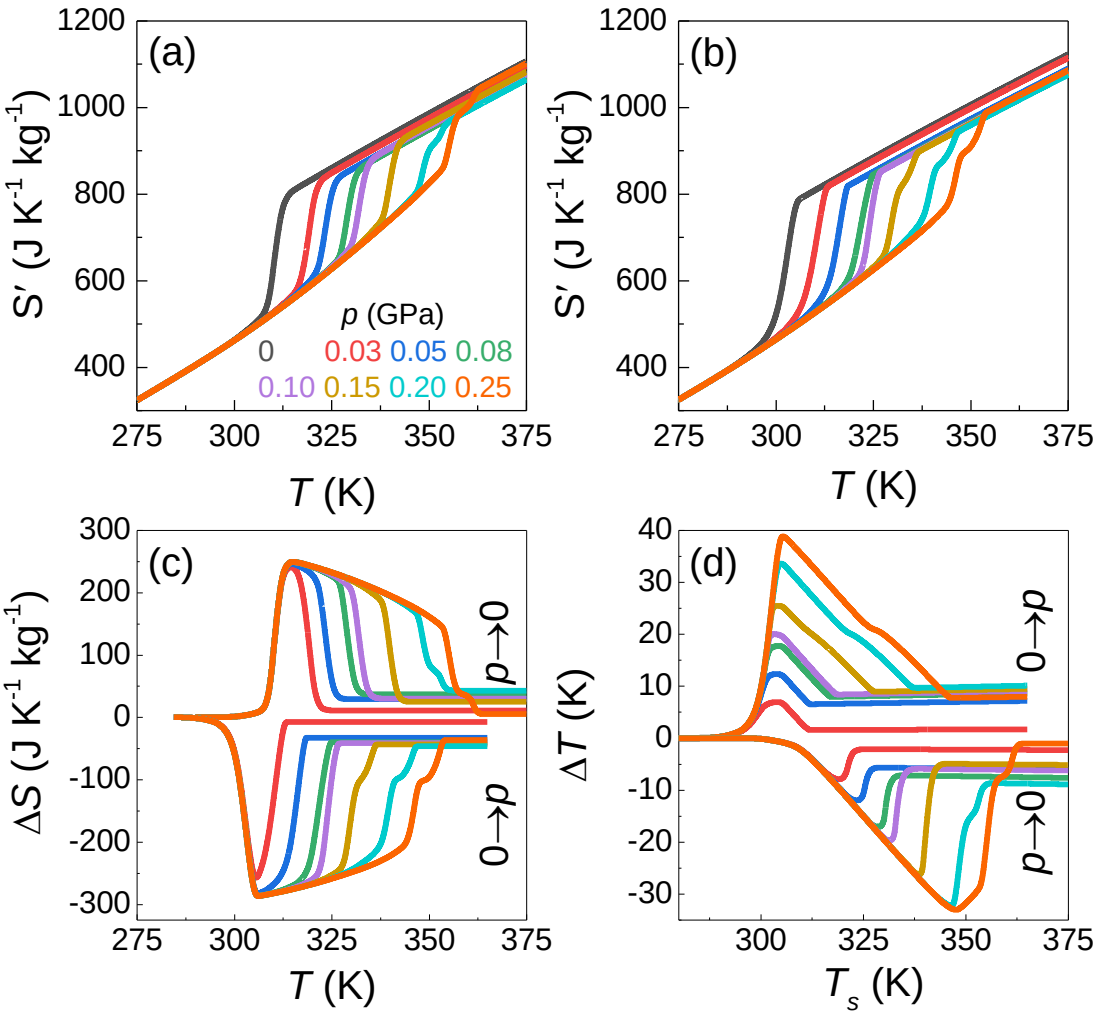

Figure 5.8. Isobaric entropy as a function of temperature for different values of applied pressure, a) on heating and b) on cooling. c) Isothermal entropy changes as a function of temperature and d) adiabatic temperature changes as a function of the starting temperature, for different values of pressure changes on first compression and on first decompression.

As shown in Chapter 3, the BC effects can be obtained from the entropy–temperature curves determined in Figure 5.8 (a) and (b). The calculated ΔS and ΔT are displayed in Figure 5.8 (c) and (d). Under $p \approx 0.1$ GPa, we obtain colossal BC effects of $\Delta S \approx 250 \pm 20$ J K^{-1} kg^{-1} and $\Delta T \approx 20$ K, which have never been reported in other materials. For higher pressure ($p \approx 0.25$ GPa), the achieved ΔT is about 35 K.

To verify the pressure-driven reversibility effect in $C_{10}Mn$, reversible BC effects are plotted in Figure 5.9 (a) and (b). The obtained results reveal reversible values for ΔS_{rev} that exceed 100 J K^{-1} kg^{-1} under pressure changes as low as 0.03 GPa, and are colossal ($\approx 230 \pm 20$ J K^{-1} kg^{-1}) under $p \approx 0.05$ GPa. As discussed in Chapter 4, the pressure change for nonzero $|\Delta S_{rev}|$ is lower than the pressure change to obtain nonzero $|\Delta T_{rev}|$. In Figure 5.9 (a) and (b), we obtain that for $C_{10}Mn$ across its phase transition, $p_{rev}^{\Delta S} \approx 0.03$ GPa, and $p_{rev}^{\Delta T} \approx 0.05$ GPa.

The area below the $|\Delta S_{rev}|$ *vs. T* curves gives an estimation of the Refrigerant Capacity (RC), which refers to the amount of heat that can be exchanged cyclically between hot and cold ends. Values for RC as a function of the pressure change are shown in Figure 5.9 (c). Under $p \approx 0.1$ GPa, we obtain colossal BC effects of $\Delta S_{rev} \approx 250 \pm 20$ J K^{-1} kg^{-1} and $\Delta T_{rev} \approx 12$ K, with a refrigerant capacity RC ≈ 3.5 kJ kg^{-1}. RC values under such low pressure have never been reported before. For a higher pressure change of ≈ 0.25 GPa, we have colossal BC effects of $\Delta S_{rev} \approx 250 \pm 20$ J K^{-1} kg^{-1} and $\Delta T_{rev} \approx 30$ K, with a refrigerant capacity RC ≈ 9 kJ kg^{-1}. All these features suggest that $C_{10}Mn$ could be a good BC cooling candidate.

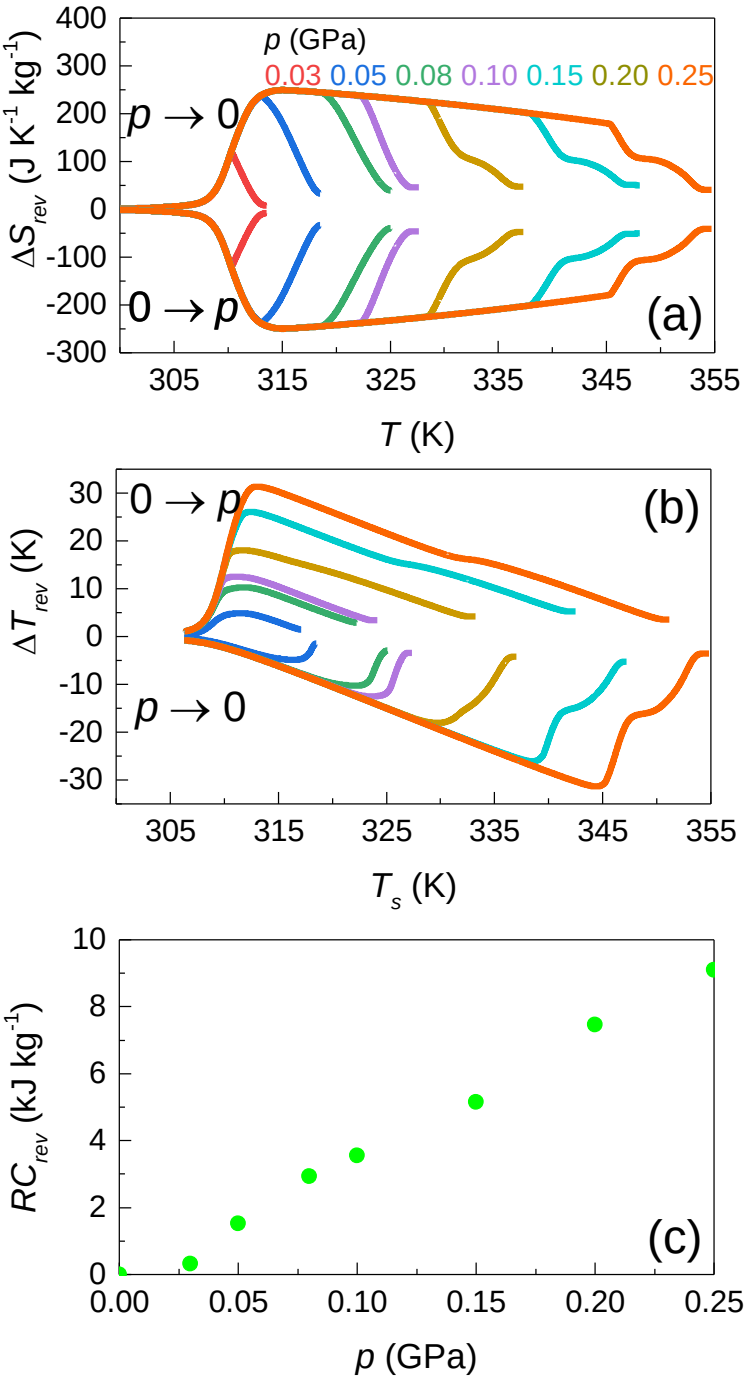

Figure 5.9. Reversible a) isothermal entropy changes and b) adiabatic temperature changes upon application and removal of pressure changes from or to atmospheric pressure, as a function of temperature. c) Reversible refrigerant capacity as a function of pressure change.

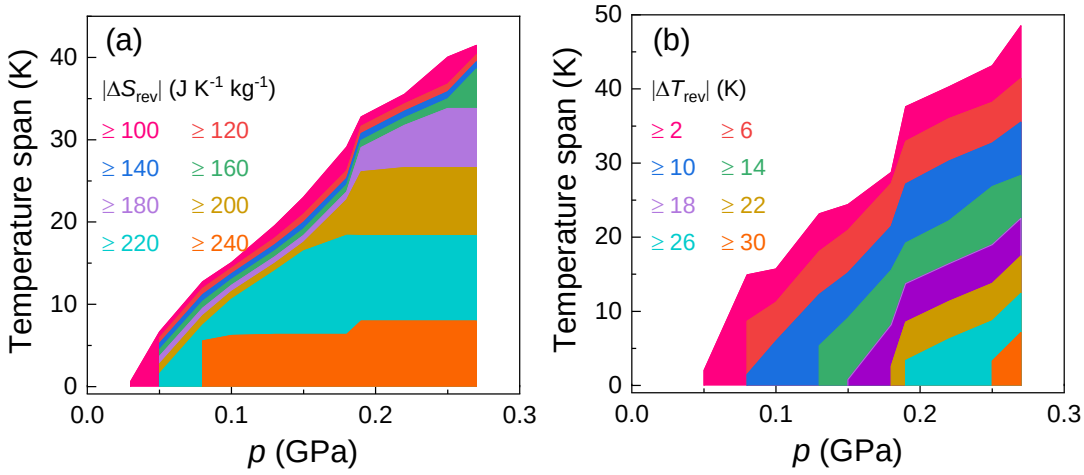

Figure 5.10. Temperature span where a range of (a) isothermal entropy changes and (b) adiabatic temperature changes take place, as a function of the required pressure change.

The temperature span where these effects occur near room temperature are plotted as a function of the applied pressure change p in Figure 5.10 (a) and (b) for ΔS_{rev} and ΔT_{rev}, respectively. For instance, at $p \approx 0.1$ GPa, at least $\Delta S \approx 100 \pm 10$ J K^{-1} kg^{-1} is obtained within an interval of ≈ 13 K. This excellent performance can be very useful in single-compound regenerative cooling methods, where heat sources and sinks are separated by large temperature spans by means of a regenerative heat exchanger.

5.5 Summary

In this chapter, colossal barocaloric effects have been reported in an unexplored material family, the layered organic–inorganic hybrid perovskites. In particular, I have shown that layered $(C_{10}H_{21}NH_3)_2MnCl_4$ undergoes reversible isothermal entropy changes of 230 J K^{-1} kg^{-1} under low pressure changes of 0.05 GPa. Additionally, the

results show an isothermal entropy change of 240 J K^{-1} kg^{-1} and reversible adiabatic temperature change of 10 K can be achieved under pressure changes of 0.08 GPa near room temperature. I have demonstrated that the origin of this extremely good response comes from the following features: a very large increase in entropy and volume associated with the melting of the organic chain across, a sharp and low-hysteresis first-order solid–solid phase transition. This research not only widens the horizons for colossal barocaloric materials to include other compounds beyond the canonical plastic crystals but it also expands the limits for the barocaloric performance in solid-state materials.

Chapter 6

Comparison and future prospects

In this chapter, I summarize and compare the barocaloric properties of different compounds by introducing the Coefficient of Refrigeration Performance. The results indicate that $(C_{10}H_{21}NH_3)_2MnCl_4$ exhibits the largest CRP value among the materials studied, showing colossal barocaloric effects. The colossal effects and large CRP values suggest that layered $(C_{10}H_{21}NH_3)_2MnCl_4$ compound could be a good barocaloric cooling candidate. We then introduce the possible ways to find excellent barocaloric effects in similar layered materials.

6.1 Barocaloric performances

A comparison of the BC performance between different compounds by computing the Coefficient of Refrigeration Performance (CRP) is shown in Table 6.1 and Figure 6.1. It can be seen that the largest CRP value so far has only been reported in materials showing giant BC effects. The largest CRP value has been reported in $[TPrA]Mn[dca]_3$, which is about 3.51 under a relatively low pressure change of 0.007 GPa. However, the

operation temperature span at this pressure is about 1 K which is too small for practical application. For $(NH_4)_2SO_4$, the CRP value at 0.1 GPa is about 3.31 which is among the best values. However, materials showing a colossal BC effect always display low CRP values. For instance, the largest value obtained in 1-Cl-ada is about 1.4 which is much lower than the value in $(NH_4)_2SO_4$. In our study, the CRP value for C_{60} is about 1.35 under a pressure change of 0.1 GPa. This value is larger than in the plastic crystals and most BC materials. Moreover, CRP values for $(C_{10}H_{21}NH_3)_2MnCl_4$ under different pressures are comparable to or better than the best reversible BC effects reported so far (e.g., 1-Br-ada and 1-Cl-ada) [9, 137]. These excellent values obtained under low pressure bring BC materials closer to real applications.

Table 6.1 Coefficient of Refrigeration Performance and associated quantities in giant barocaloric materials

Materials	T_t (K)	ΔT_{rev} (K)	ΔS (J K^{-1} kg^{-1})	ΔV 10^{-6} m^3 kg^{-1}	Δp (GPa)	CRP	Refs.
$MnCoGeB_{0.03}$	286	10	30	5.0	0.17	0.71	120
$Ni_{50}Mn_{31.5}Ti_{18.5}$	243	7.3	74	1.9	0.40	0.96	58
$BaTiO_3$	400	5	1.6	0.19	0.1	0.67	73
$(NH_4)_2SO_4$	219	8	60	2.9	0.10	3.31	17
AgI	390	18	60	7.4	0.25	1.17	20
Fe_3(*bntrz*)$_6$(*tcnset*)$_6$	316	35	120	20.5	0.26	1.6	59
$[TPrA]Mn[dca]_3$	330	4.1	30	10.0	0.007	3.51	23
$[TPrA]Cd[dca]_3$	385	1.4	11.5	5.3	0.007	0.87	21
$(CH_3)_2C(CH_2OH)_2$	315	6	450	46	0.20	0.59	24, 25
$(CH_3)C(CH_2OH)_3$	354	10	490	38	0.24	1.07	27
$(CH_3)_3C(CH_2OH)$	235	16	320	45.5	0.26	0.87	27
1-Cl-ada[1]	254	15	160	47	0.10	1.4	137
1-Br-ada[2]	316	20	130	40	0.10	1.2	137
C_{60}	257	9.7	32	4.6	0.10	1.35	This work
$(C_{10}H_{21}NH_3)_2MnCl_4$	306	10	249	36	0.08	2.17	This work
$(C_{10}H_{21}NH_3)_2MnCl_4$	306	27	249	36	0.19	2.47	This work

[1] 1-chloroadamantane ($C_{10}H_{15}Cl$); [2] 1-bromoadamantane ($C_{10}H_{15}Br$).

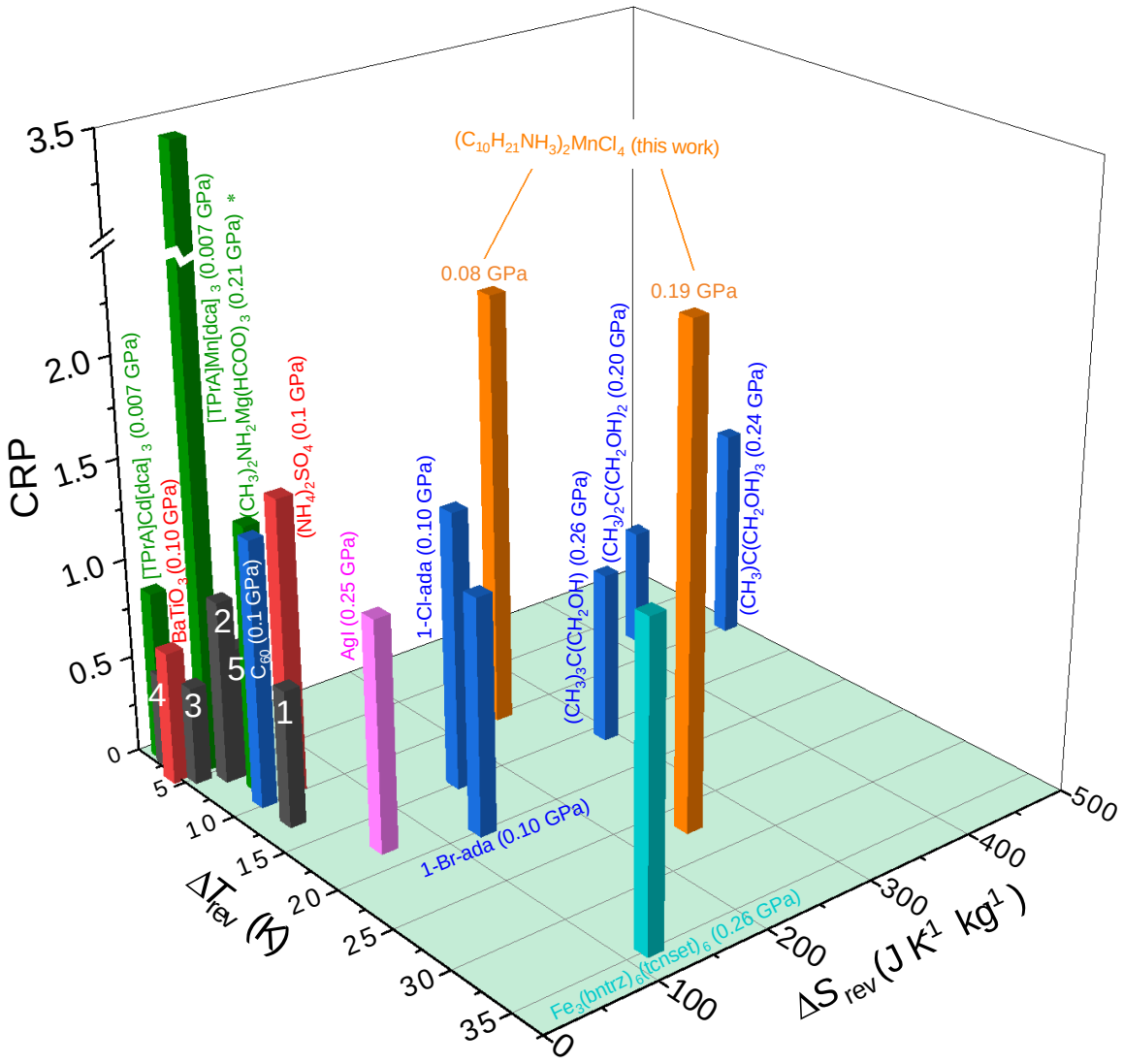

Figure 6.1. Coefficient of refrigerant performance (CRP), reversible adiabatic temperature changes (ΔT), and reversible isothermal entropy changes (ΔS) for different materials reported in the literature. [9] Label 1 corresponds to $MnCoGeB_{0.03}$, 2 to $Co_{50}Fe_{2.5}V_{31.5}Ga_{16}$, 3 to $Fe_{49}Rh_{51}$, 4 to $Ni_{35.5}Co_{14.5}Mn_{35}Ti_{15}$, and 5 to $MnNiSi_{0.61}FeCoGe_{0.39}$. Colour bars stand for different types of transitions: Black refer to ferromagnetic or metamagnetic systems, cyan to spin-crossover compounds, magenta to superionic conductors, red to ferroelectric inorganic salts, blue to plastic crystals, green to HIOPs and orange to the hybrid compound studied in this work. *The value of ΔT used for $(CH_3)_2NH_2Mg(HCOO)_3$ is irreversible.

6.2 Barocaloric effect in other layered materials

Since colossal BC effects have been successfully demonstrated in $(C_{10}H_{21}NH_3)_2MnCl_4$, we now pay attention to other materials showing similar structure as discussed in the Motivation section. Figure 6.2 summarizes 2D HOIPs showing solid-solid phase transitions with different chemical components from Refs. 151 to 155. In addition, a series of dialkyl ammonium salts $(C_nH_{2n+1}NH_3)_2W$ (n=1, 2, 3…) with W = Cl, Br, I, ClO_3 and NO_3 is included, which also shows a layered structure but not based on the perovskite structure. These salts exhibit a bilayer structure like 2D HOIPs but with long alkyl chains and ionic layers with the orientation of the alkyl chains is vertical or more or less inclined to the ionic layer. Phase transition properties associated with these salts highly rely on the ionic layer and the long organic chains just like 2D HOIPs. Therefore, an extensive review on those layered materials is meaningful.

In Figure 6.2 (a), one can see that the phase transition entropy changes show enhancement with the increasing of *n*. Meanwhile, as it has been shown in Figure 6.2 (b), the phase transition temperature is increased too. Generally, the entropy changes for $(C_nH_{2n+1}NH_3)_2MCl_4$ are about 200 J K^{-1} kg^{-1} for transitions near room temperature. However, as we have discussed before, most of the samples show two or more phase transitions and these transitions shows a large temperature gap. Thus, one can only choose to use the major phase transition for BC study even if the minor transition is associated with a giant entropy change.

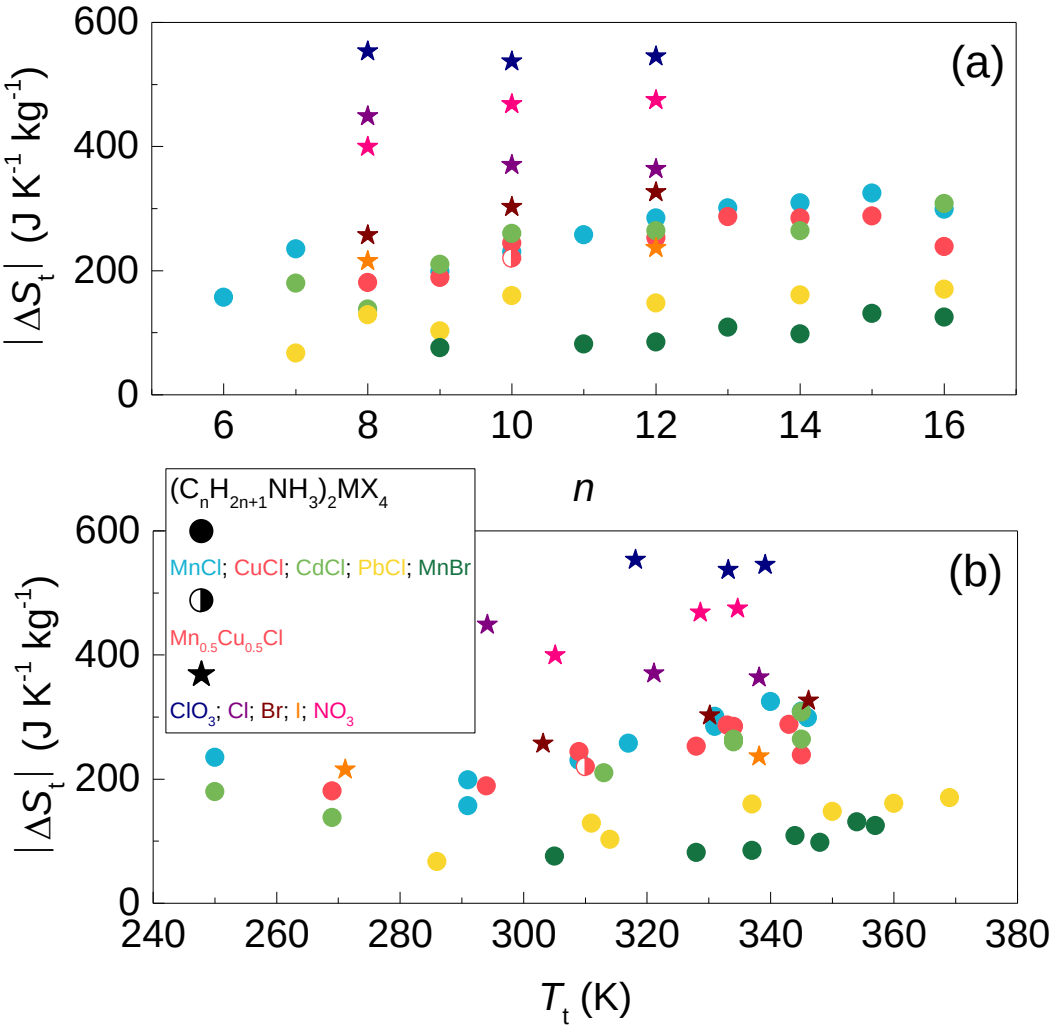

Figure 6.2. Summary of the solid-solid phase transitions in layered materials with dialkyl ammonium structure. (a) The transition entropy changes as a function of *n*, where *n* is the number of carbons in organic cations. (b) The transition entropy changes as a function of phase transition temperatures. Notice that some materials show two or more phase transitions, which normally include a major transition and a minor transition. Here, for better illustration, the transition temperature for major transition is used in this plot. The half-filled circle stands for $(C_{10}H_{21}NH_3)_2(Mn_{0.5}Cu_{0.5})Cl_4$ that was prepared and characterized in the lab.

For $(C_nH_{2n+1}NH_3)_2W$, the values for entropy change are about two times those in 2D HOIPs. In particular, materials with chlorate or nitrate anions exhibit larger entropy changes than those with halide ions. However, a larger entropy change is always accompanied by an increased transition temperature. Therefore, to find a promising candidate, one needs to modify the phase transition properties by adjusting the organic cations and anions. It is also worth noting that the thermal hysteresis in $(C_nH_{2n+1}NH_3)_2W$ is larger than in $(C_nH_{2n+1}NH_3)_2MCl_4$.

Considering the above discussions, some optimization methods for these materials are considered and discussed below.

Materials preparation:

Sample preparation for these materials is quite simple as we have shown in section 5.3. Polycrystalline samples used for our BC study were quickly recrystallized from the hot solution. However, we noticed that one can prepare single crystals or sample with good qualities by cooling the hot solution very slowly. In this way, layered samples will show high alignment properties (or single crystals) which have been confirmed by our XRPD data (see Figure A6 in Appendix A). Here, based on our XRPD data, we can absolutely conclude that the slowly prepared materials show high alignment properties. However, we cannot confirm that they are single crystals because we did not do the single-crystal X-Ray diffraction.

Then we measured the phase transition properties through DSC (see Figure 6.3). The corresponding results show a smaller transition hysteresis of 4.5 K as defined from the

peak maxima, and 1.5 K as defined from the peak onsets respectively. Values for polycrystalline power samples are 9 K, and 3 K respectively. At the same time, the entropy change for this transition is not changed (~240 J K^{-1} kg^{-1}). Therefore, one possible way to get perfect BC materials in layered materials is by preparing single crystals rather than polycrystalline materials. Actually, this has been confirmed and well investigated in a recent work on a BC study of $(C_{10}H_{21}NH_3)_2MnCl_4$.

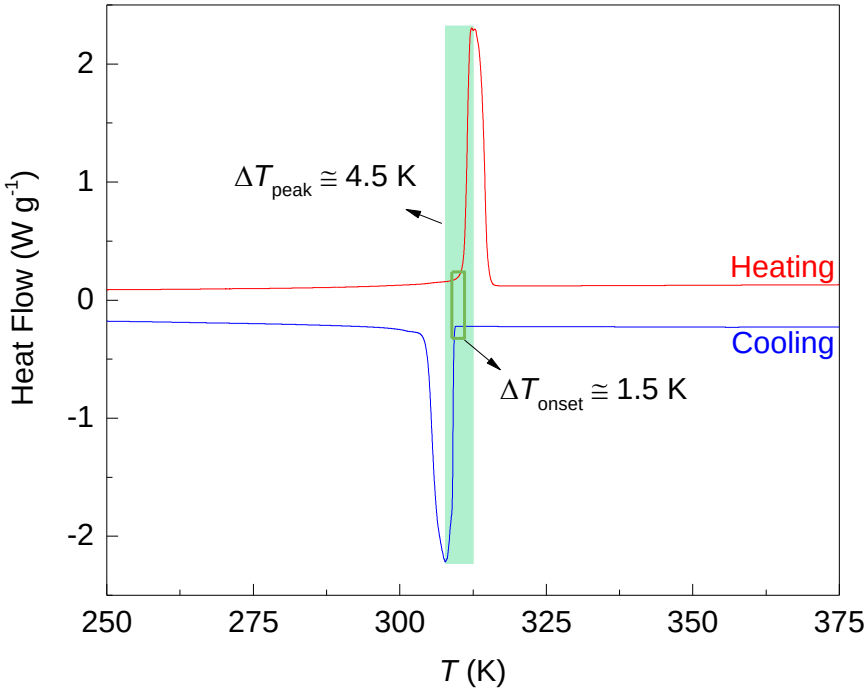

Figure 6.3. Heat flow curve of $(C_{10}H_{21}NH_3)_2MnCl_4$ samples [highly aligned in (001)] in temperature.

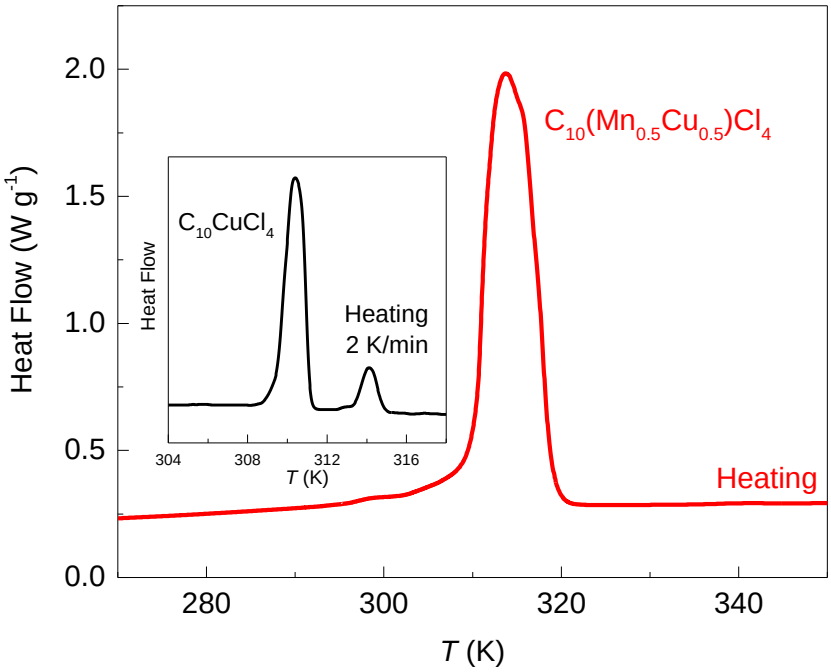

Figure 6.4. The heat flow curve of $(C_{10}H_{21}NH_3)_2(Mn_{0.5}Cu_{0.5})Cl_4$. The inset shows the heat flow curve of $(C_{10}H_{21}NH_3)_2CuCl_4$ where the heat flow value is not presented in the original paper (reproduced from Ref. 155).

Elemental substitution:

Due to the unique "chain melting" transition, 2D HOIPs always include one major and one minor phase transition. This will enlarge the transition width and require a large pressure to drive a full reversible phase transition. Here, we try to modify this transition feature through chemical doping. It is known that $(C_{10}H_{21}NH_3)_2MnCl_4$ shows one single phase transition at room temperature. $(C_{10}H_{21}NH_3)_2CuCl_4$ exhibits two room temperature transitions with two exothermic and two endothermic peaks [155]. We synthesized a new compound with 50% of Cu replaced by Mn, $(C_{10}H_{21}NH_3)_2(Mn_{0.5}Cu_{0.5})Cl_4$. Manganese(II) chloride tetrahydrate ($MnCl_2 \cdot 4H_2O$,

99%, Sigma-Aldrich) and copper(II) chloride dihydrate ($CuCl_2 \cdot 2H_2O$, 99%, Sigma-Aldrich) were added into hydrochloric acid (HCl, 36.5–38.0%, Baker Analyzed) with magnetic stirring until the $MnCl_2 \cdot 4H_2O$ and $CuCl_2 \cdot 2H_2O$ were fully dissolved. Then, n-decylamine ($C_{10}H_{21}NH_2$, 99%, ACROS Organics) was added into this mixed solution with magnetic stirring for 3 hours. Then, $(C_{10}H_{21}NH_3)_2(Mn_{0.5}Cu_{0.5})Cl_4$ powder was obtained by precipitation and washed with ethanol twice.

Then we measured the phase transition properties through DSC (see figure 6.4). The result shows one exothermic peak across the phase transition at 310 K with an entropy change of 230 J K^{-1} kg^{-1} which shows no reduction (see Figure 6.2). However, a more systemic characterization is needed on the new sample and combined with a thorough analysis. For example, the heating rate we used here was 10 K/min which is larger than the 2 K/min in the literature report for $(C_{10}H_{21}NH_3)_2CuCl_4$. DSC runs with more heating rates are needed. Furthermore, a full structure characterization should be performed to study the influence of doping. Finally, one may also need to test the phase transition properties under high pressure cycles to confirm this single peak under higher pressure.

Dialkyl ammonium salts:

As we can see from Figure 6.2, dialkyl ammonium salts display larger entropy changes than 2D HOIPs. However, further BC study on these materials has never been reported. Here, I study the phase transition properties of $(C_8H_{17}NH_3)_2Cl$ at low pressure using DSC from Setaram, KEP Technologies. Here, nitrogen gas is used to maintain the pressure. Heat flow curves under a pressure range from 0 to 0.02 GPa are shown in

Figure 6.5 (a). Unlike the heating curve, there is a minor transition seen during cooling. This minor phase transition is very sensitive to the external pressure as the $dT/dp \approx$ 1000 K GPa^{-1}. As one can see from Figure 6.5 (b), this minor peak disappeared under a pressure change of 0.014 GPa. While more high-pressure data cannot be achieved through this set-up, one still can obtain some useful data for BC study. For example, the calculated results show a smaller transition hysteresis of 6.5 K as defined from the peak maxima, and 3 K as defined from the peak onsets. The dT/dp for heating and cooling in this compound is about 210 and 160 K GPa^{-1} respectively. These data demonstrate that this material is very good for low-pressure driven BC cooling. Moreover, the transition entropy change in $(C_8H_{17}NH_3)_2Cl$ is about 370 J K kg^{-1} which is comparable with the entropy change in the best BC materials reported so far. Combining the low thermal hysteresis, large dT/dp and colossal transition entropy change, this material is a very good candidate for BC cooling study.

Overall, I have summarized the layered materials with colossal entropy change across first-order phase transitions. With an expectation of finding excellent BC effect in 2D HOIPs or layered materials, I have introduced two possible methods to modify the phase transition properties. I have also predicted a colossal BC effect under low pressure change in $(C_8H_{17}NH_3)_2Cl$.

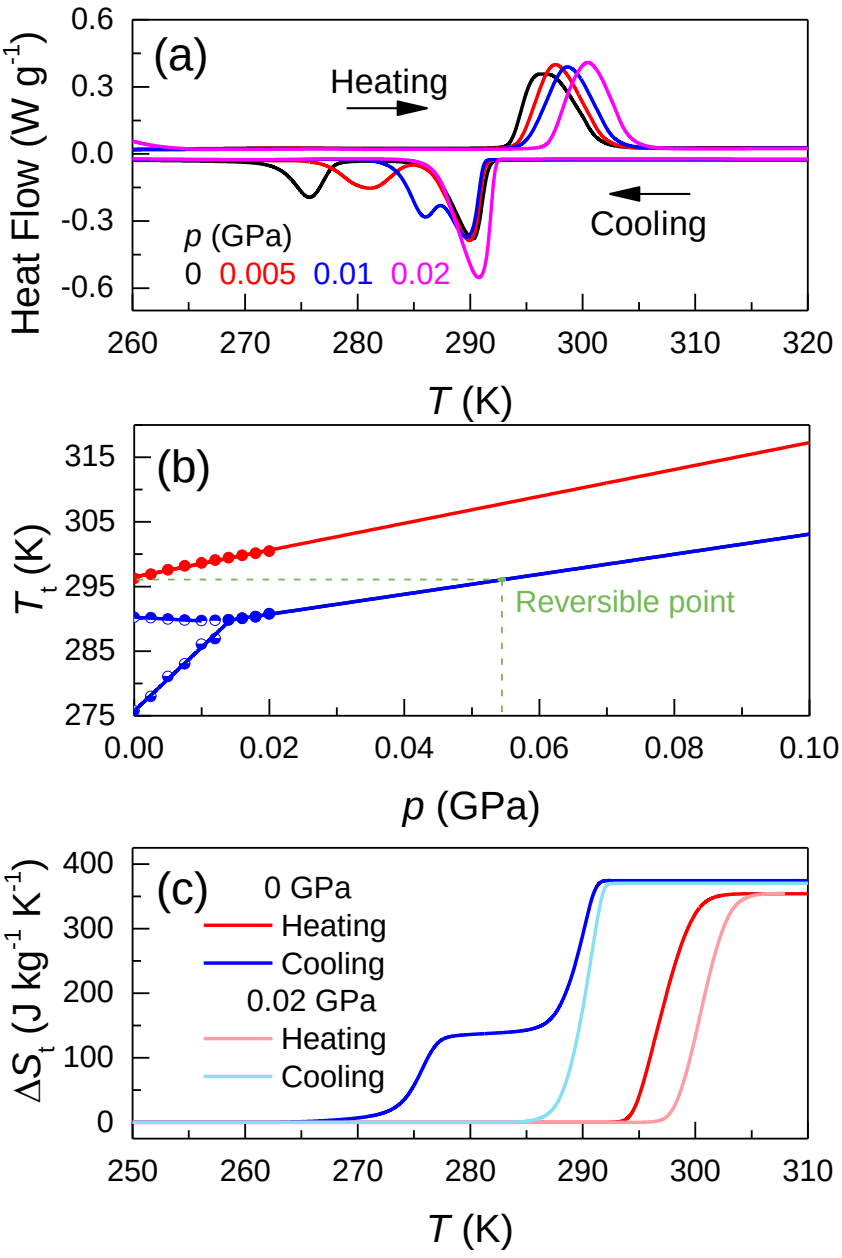

Figure 6.5. Phase transition properties of $(C_8H_{17}NH_3)_2Cl$ under pressure. (a) Heat flow curves in temperature. (b) Phase transition temperature as a function of pressure. (c) The entropy of phase transition under atmospheric pressure and high pressure.

6.3 Summary

Finally, I have summarized the layered materials with colossal entropy change across first-order phase transition. Based on preliminary results, proposed methods in finding excellent barocaloric materials are presented. Our study paves the way for finding colossal BC effects in compounds beyond plastic crystals, thus widening the range of suitable materials and stimulating the research in similar compounds. This is especially appealing in this family of compounds because material properties can be sensitively tuned to match desired features by changing the chain length and/or by chemical substitution of the cation.

Chapter 7

The effect of anisotropy on caloric properties in two-dimensional hybrid organic-inorganic perovskite

In this chapter, I investigated the lattice deformation behaviour during first-order phase transition in two-dimensional hybrid organic-inorganic perovskites, in particular $(C_{10}H_{21}NH_3)_2MnCl_4$. A very strong anisotropic effect in lattice deformation was found in the *c*-axis which is about one order of magnitude larger than the value for the *a*-axis and the *b*-axis. Thermodynamically, I obtained a colossal elastocaloric effect under relatively low uniaxial stress which was applied along the direction of the *c*-axis. This colossal elastocaloric effect originates from the mechanical flexibility of hybrid perovskites and stress-induced lattice formation in specific direction. Regarding this finding, I have proposed a direct observation of elastocaloric effects in two-dimensional perovskites by using an infrared camera. This work provides a way of finding elastocaloric effects in two-dimensional materials other than shape-memory alloys and polymers in recent research focus.

7.1 Motivation

Mechanocaloric (mC) effects have been mainly studied as barocaloric (BC) and elastocaloric (eC) effects in a wide range of materials [7]. In Chapter 2, I analysed the BC effect from the point of view of thermodynamics in Section 2.2. Here, I will briefly introduce the thermodynamics of the eC effect.

For the eC effect, the differential change of Gibbs free energy associated with differential changes of temperature T and stress σ are given by

$$dG = -SdT - \varepsilon d\sigma, \tag{7.1}$$

and, the entropy S and strain ε are expressed as

$$S = -\left(\frac{\partial G}{\partial T}\right)_{\sigma}, \tag{7.2}$$

$$\varepsilon = -\left(\frac{\partial G}{\partial \sigma}\right)_{\sigma}. \tag{7.3}$$

Then, using Equations (7.2) and (7.3), the Maxwell relation can be derived in terms of (S, T) and (ε, σ) as follows

$$-\left(\frac{\partial^2 G}{\partial \sigma \partial T}\right)_{\sigma} = \left(\frac{\partial \varepsilon}{\partial T}\right)_{\sigma} = \left(\frac{\partial S}{\partial \sigma}\right)_{T} = \alpha. \tag{7.4}$$

For eC effects, ΔS and ΔT are expressed as

$$\Delta S(T, 0 \rightarrow \sigma) = S(T, \sigma) - S(T, 0) = \int_0^{\sigma} \left(\frac{\partial \varepsilon}{\partial T}\right)_{\sigma} d\sigma, \tag{7.5}$$

and

$$\Delta T(0 \rightarrow \sigma) = T(S, \sigma) - T(S, 0) = -\int_0^{\sigma} \frac{T}{C} \left(\frac{\partial \varepsilon}{\partial T}\right)_{\sigma} d\sigma. \tag{7.6}$$

From Equations (7.5) and (7.6), we can see that an enhanced eC effect can be found in materials with a strong temperature induced length (in a specific direction) change.

Actually, Equation (7.4) reveals that solid materials showing large linear thermal expansion coefficients α, may theoretically exhibit excellent eC effects.

In our two-dimensional (2D) perovskites $(C_{10}H_{21}NH_3)_2MnCl_4$ ($C_{10}Mn$), we noticed that the lattice deformation in the *c*-axis, which occurred during heating, is about ~ −7.7% which is extremely large when compared with the value in the *a*-axis (~ −0.64%) and the *b*-axis (~ 0.3%) (see Figure 7.1). This anomalous change across the phase transition comes from the conformational change of the organic chain which was explained in Chapter 5. We understand that this anisotropic effect may have less impact on BC property because hydrostatic pressure is applied from all directions. However, according to Equations (7.4) and (7.5), this strong temperature-induced lattice deformation in the *c*-axis indicates a strong eC response if there is a uniaxial compressive stress applied along the direction of the *c*-axis.

The anisotropic effect on eC properties has been studied in $(NH_4)_2NbOF_5$ [156], $(NH_4)_2SO_4$ [157] and $NH_2CH_2COOH)_3{\cdot}H_2SO_4$ [158] single crystals. Mikhaleva and co-workers found a large eC effect under uniaxial compression along the *b*-axis in single crystal NH_4HSO_4, which is two times larger than the values obtained from the other axes [159]. Interestingly, under uniaxial compression, an inverse effect in the *c*-axis was observed. They also proposed a cooling cycle with enhanced thermodynamic efficiency by alternate using uniaxial compression along the a-axis and the c-axis. However, the obtained eC effects were small due to the low lattice deformation in specific axes and weak anisotropic effects in these three-dimensional crystals.

Thanks to the 2D structure of $C_{10}Mn$, we found a strong anisotropic effect in the *c*-

axis with a large lattice deformation in this direction. Therefore, we expected to find an eC effect in this strongly anisotropic material.

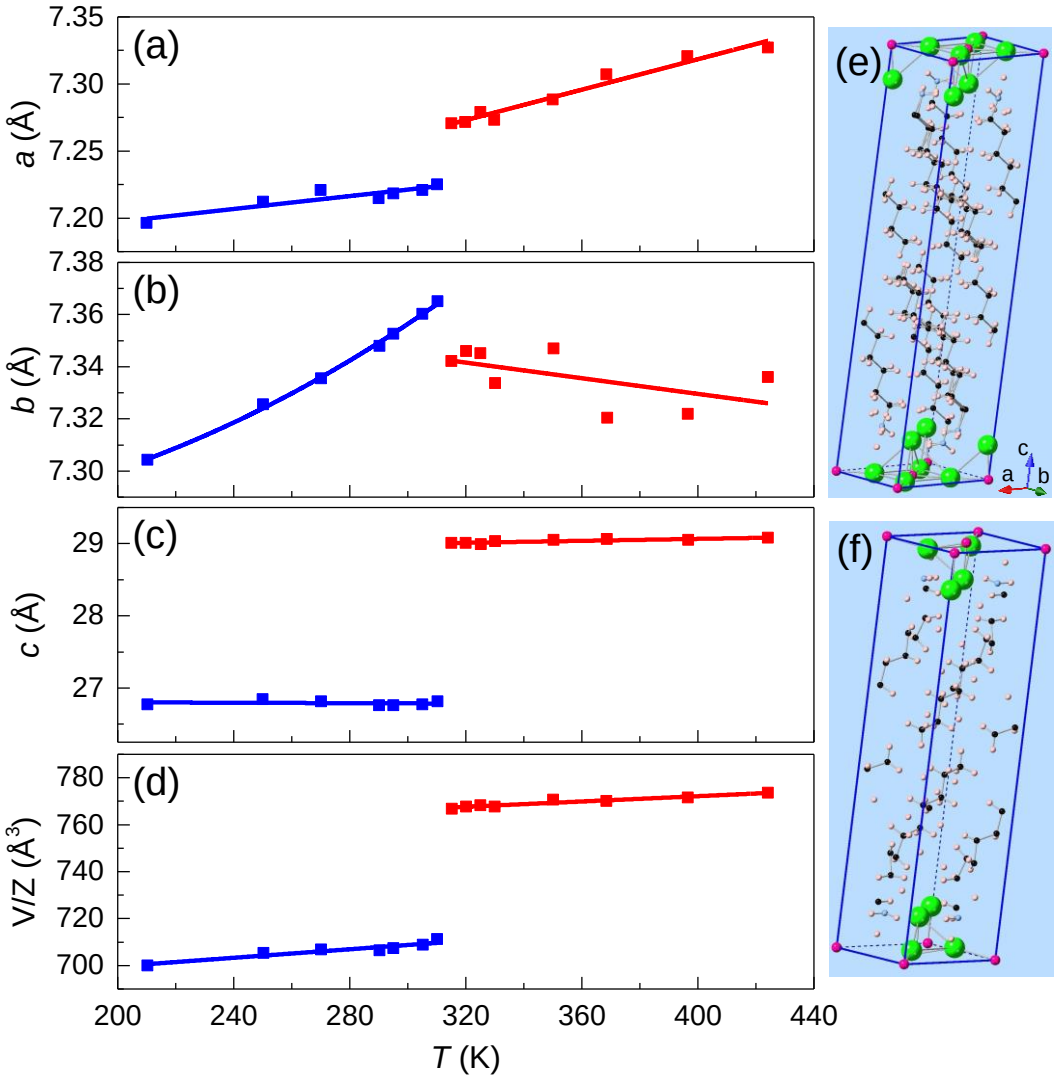

Figure 7.1. Temperature dependencies of (a-c) *a*-, *b*-, and *c*-axis lattice parameters, and (d) unit cell volume per formular unit of $(C_{10}H_{21}NH_3)_2MnCl_4$ as determined from data shown in Figure A5 in Appendix A. Red and blue symbols correspond to high-temperature phase (*C*2/*m*) and low-temperature phase ($P2_1/a$), respectively. (e) and (f) show the unit cell of high-temperature phase and low-temperature phase respectively.

7.2 Structure and phase diagram

For eC calculations based on the quasidirect method, one needs to measure the heat capacity data at atmospheric pressure, the specific volume data at atmospheric pressure and heat flow at constant external fields to construct the entropy change curves (see Section 3.4.1). The data at atmospheric pressure have been systematically studied and presented in Chapter 5. The core part of this method is the heat flow measured at constant external fields. Although we have no heat flow data at higher stress, we assumed that the heat capacity and the phase transition entropy under high stress within our studied range is constant. Therefore, we have $c(T', \sigma_{\mathrm{atm}})$ and $(dQ/dT)_{\sigma_{\mathrm{atm}}}$ at constant uniaxial stress. Then, the entropy change curves $S(T, \sigma)$ can be expressed mathematically as:

$$S(T,\sigma) = S(T_0,\sigma_{\mathrm{atm}}) + \int_{T_0}^{T} \frac{1}{T'}\left(c(T',\sigma_{\mathrm{atm}}) + \frac{dQ}{dT'}(T',\sigma_{\mathrm{atm}})\right) dT'. \qquad (7.7)$$

Here, the contribution of the lattice entropy change under uniaxial stress is not included. The last step is the shifting of the phase transition temperature or entropy curves under high stress which can be been calculated from the Clausius-Clapeyron equation. For the eC effect, the Clausius-Clapeyron equation is expressed as follows

$$\frac{dT}{d\sigma} = -\frac{\Delta\varepsilon}{\Delta S_{\mathrm{t}}} V_0, \qquad (7.8)$$

where $\Delta\varepsilon$ is the transformation strain during the phase transition and V_0 is the volume of the high-temperature phase (*C*2/*m*) (see Figure 7.1). One can calculate the d*T*/dσ value (shift of transition temperature) using the strain change and entropy change across phase transition at ambient pressure.

Table 7.1. Lattice deformation and the shift of the phase transition temperatures of $C_{10}Mn$ under uniaxial compressive stress (0 - 150 MPa) and hydrostatic pressure (0 - 150 MPa).

	$\frac{\Delta i}{i}\left(\frac{\Delta V}{V}\right)$ (%)	$\frac{\mathrm{d}T}{\mathrm{d}\sigma_i}\left(\frac{\mathrm{d}T}{\mathrm{d}p}\right)$ ($\times 10^{-3}$ K·MPa^{-1})
a	-0.64 ± 0.06	19 ± 1
b	0.30 ± 0.03	-9 ± 1
c	-7.66 ± 0.7	225 ± 20
V_{cal}[1]	-8 ± 0.8	235 ± 20
V_{exp}[2]	-7.52 ± 0.7	250 ± 20

[1] V_{cal} obtained from the summation of $(\Delta i/i)$, i refers to the a-, b-, and c- axes. [2] V_{exp} is the experimental data shown in Chapter 5.

We firstly consider the σ-T diagram. Normally, the σ-T diagram is experimentally constructed by measuring the heat flow at constant pressure. However, the dT/dσ predicted from Equation (7.8) agreed very well with experimental results in many research works [55,160-162]. This allows us to construct the σ-T diagram through Equation (7.8) by using data at atmospheric pressure. Table 7.1 shows the lattice deformation in different axes. Strain change is calculated as $\Delta\varepsilon = (\Delta i/i)$, i is the lattice data of the a-, b-, and c-axes respectively. It can be seen that the $\Delta\varepsilon$ for the c-axis is about one order of magnitude larger than the value for the a-axis and the b-axis. In addition, by using Equation (7.8), we also present the dT/dσ values in Table 7.1. The large dT/dσ value in the c-axis indicates that the uniaxial stress along the direction of the c-axis can greatly change the phase transition temperature. All these data demonstrate the fact that the anisotropic effect in the c-axis is very strong. While we cannot examine our data through experiments, the relations between $\Delta\varepsilon$ and ΔV_t ($\frac{\Delta V_t}{V} = \sum_{i=a,b,c}\frac{\Delta i}{i}$) provide us a

chance to compare experimental dT/dp with the data based on our dT/dσ. We can see that the calculated data and the experimental data shows a good agreement. In this way, we carefully state that this method in predicting the dT/dσ is reasonable. Furthermore, by comparing the dT/dp with the dT/dσ in c-axis, one can find that this colossal caloric effect achieved through hydrostatic pressure can also be induced by a uniaxial stress along *c*-direction thanks to the strong anisotropic effect. Based on the above calculations and discussion, we then plot the σ-T diagram in Figure 7.2.

During the construction of the σ-T diagram (under compressive stress), we only plot a stress range from atmospheric pressure to 150 MPa for two reasons. On the one hand, a new phase (phase III in Chapter 5) appeared when applied hydrostatic pressure is larger than 150 MPa. This critical behaviour has a strong influence on the entropy change and dT/dp. It is strongly believed that this new phase can be observed under a large uniaxial stress. Therefore, we intend to study the eC effect at low stress and avoid this critical point to make a more convincing prediction. On the other hand, in the BC study, the entropy change of the phase transition shows a reduction with the increase of the pressure. This decrease implies a pressure-induced decreasing of $|\Delta V_0|$ via the Clausius-Clapeyron equation. Under a uniaxial stress, the volume decrease may not be as strong as hydrostatic pressure. Actually, it has been experimentally shown that the uniaxial stress has less impact on the entropy change of the phase transition in shape-memory alloys [162-164] with applied stress below 150 MPa. Therefore, a small uniaxial stress under 150 MPa is reasonable and preferred in this study.

In the phase diagram, one can see that the phase transition temperature is very sensitive to the mechanical stress along the direction of the *c*-axis within our studied stress

range. An orange line for the hydrostatic pressure-induced transition is plotted for better illustration. For compression stress along the *b*-axis, the phase transition temperature shows decrease with increasing stress. This indicates that both conventional and inverse eC effects can be realized within compression stress applied along different directions.

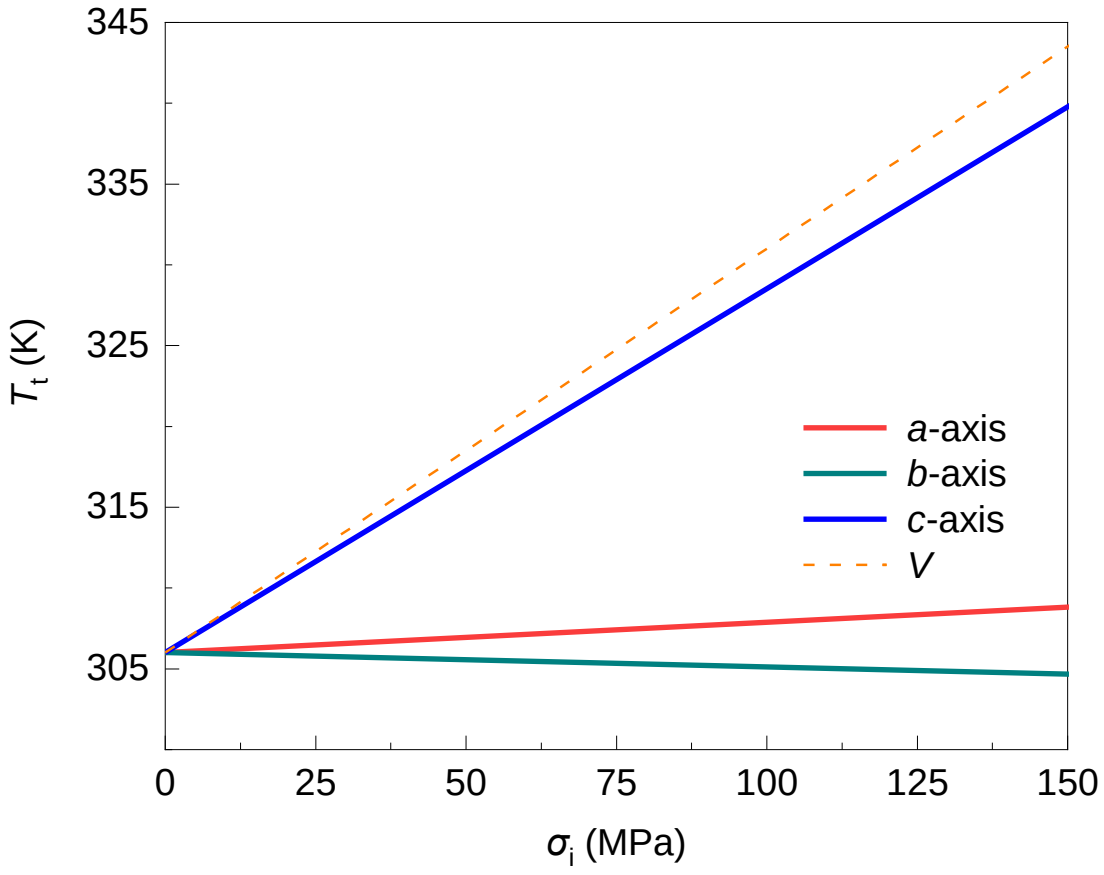

Figure 7.2. The σ-T phase diagram of $(C_{10}H_{21}NH_3)_2MnCl_4$ under applied uniaxial compressive stress in different directions (0 - 150 MPa). The orange dashed line indicates the pressure-induced temperature change.

7.3 Caloric responses under uniaxial stress

Through the use of the above method, we finally construct the $S(T, \sigma)$ curves with applied stress along the direction of the *a*-, *b*- and *c*-axes respectively. The $S(T, \sigma)$ curves with applied stress along the direction of the *a*- and *b*-axes are shown in Figure 7.3 (a) and 7.4(a). Caloric effects were calculated from σ to zero stress so that stress changes will be approximated to $|\Delta \sigma| \approx \sigma$. For phase transitions with $dT/d\sigma > 0$, transitions on uniaxial compression are exothermic and therefore ΔS and ΔT on first compression must be computed from isoelastic entropy functions on cooling, [$S_C(T, \sigma)$]), as displayed in Figure 7.3 (c) and (d). For phase transitions with $dT/d\sigma < 0$, transitions on uniaxial compression are endothermic and therefore ΔS and ΔT on first compression must be computed from isoelastic entropy functions on heating, [$S_H(T, \sigma)$]), as displayed in Figure 7.4 (c) and (d). It can be seen that the uniaxial stress applied along *a*- and *b*-axis can induce a giant isothermal entropy change of 160 and 80 J K^{-1} kg^{-1} at 150 MPa respectively. However, the adiabatic temperature change and the temperature span for ΔS and ΔT are relatively small owing to the low $dT/d\sigma$ value. Obviously, the applied 150 MPa uniaxial stress is too low to drive a full phase transition.

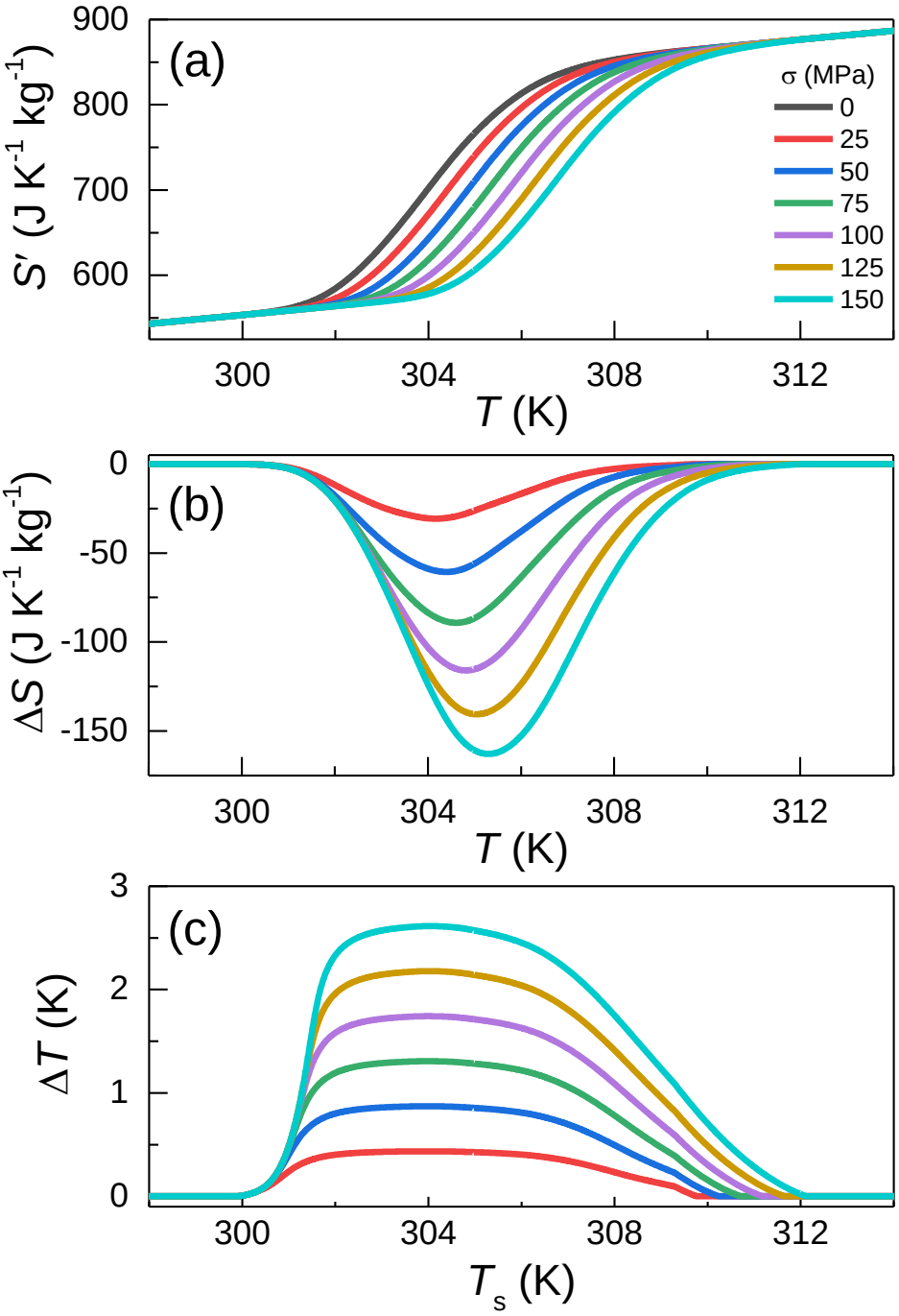

Figure 7.3. Temperature dependencies of (a) isoelastic entropy, (b) isothermal entropy changes and (c) adiabatic temperature changes for different values of applied uniaxial compressive stress in the *a*-axis direction.

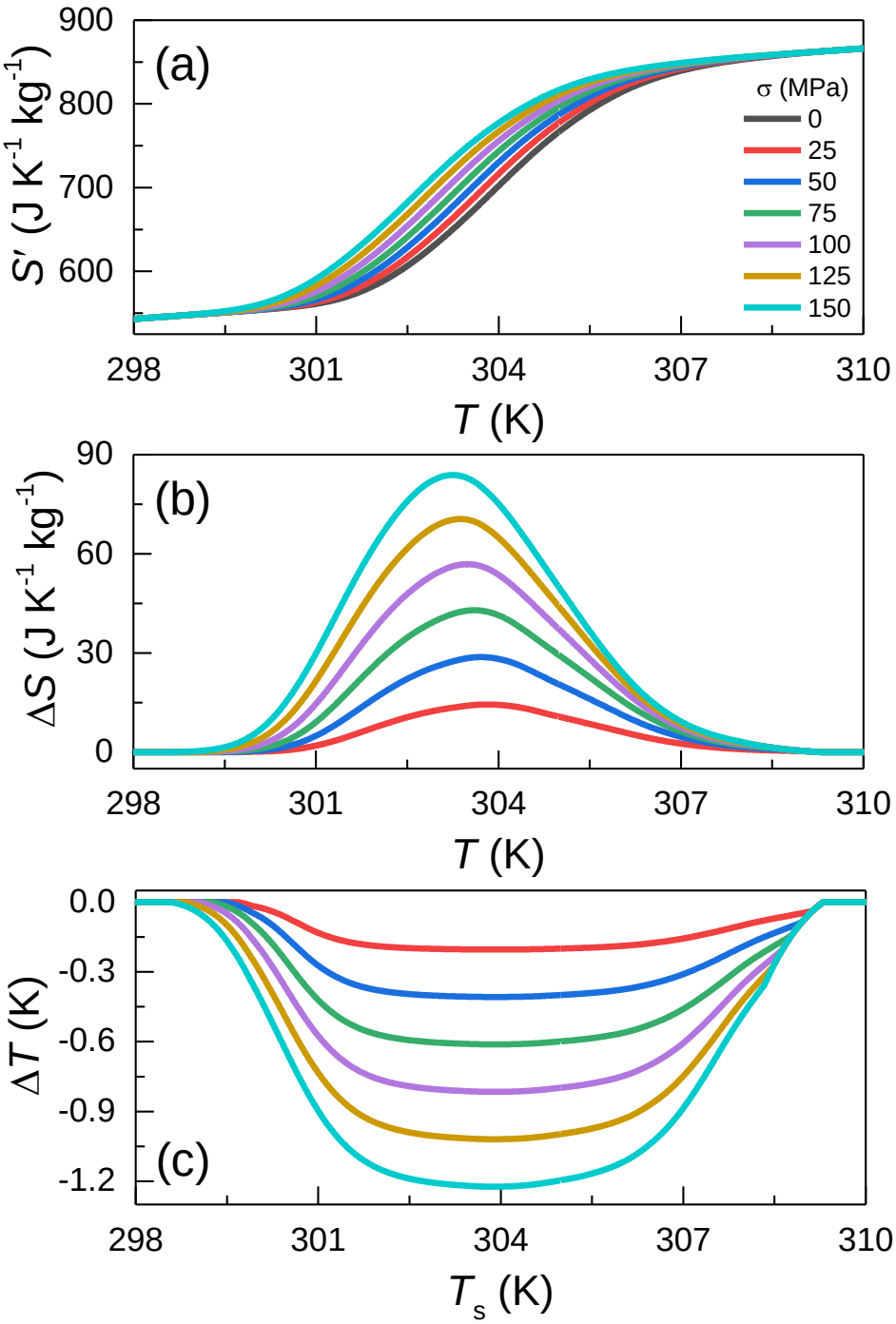

Figure 7.4. Temperature dependencies of (a) isoelastic entropy, (b) isothermal entropy changes and (c) adiabatic temperature changes for different values of applied uniaxial compressive stress in the b-axis direction.

In Figure 7.5, we show the obtained eC effects along *c*-axis. There is a colossal entropy change of $|\Delta S| \approx 250$ J K^{-1} kg^{-1} under such a small change of $|\Delta\sigma| \approx 25$ MPa, such a large eC effect has never been reported before. It is to be noted that a theoretical work has predicted a colossal eC effect with an entropy change of 200 in J K^{-1} kg^{-1} in the so called fast ion conductor, CaF_2 crystal [165]. However, despite the fact that its phase transition temperature is 163 K, the required stress is 5000 MPa which is a huge value when compared with the stress value in the present work.

The largest value of $|\Delta S| \approx 260$ J K^{-1} kg^{-1} was achieved under $|\Delta p| \approx 50$ MPa. Importantly, the large stress-induced shift of transition temperature (Figure 7.2) permits large entropy changes to be driven over a wide range of temperatures. For example, values of $|\Delta S| \approx 260$ J K^{-1} kg^{-1} can be driven in a temperature range of 25 K using $|\Delta\sigma| \approx 150$ MPa [Figure 7.5 (b)]. In addition, a large $|\Delta T| \approx 30$ K can be achieved under a stress change of $|\Delta\sigma| \approx 150$ MPa [Figure 7.5 (c)]. The eC effects under such low stress that we report here compare favourably to the best caloric effects that have been achieved in solid-state caloric materials near room temperature [24, 25, 55].

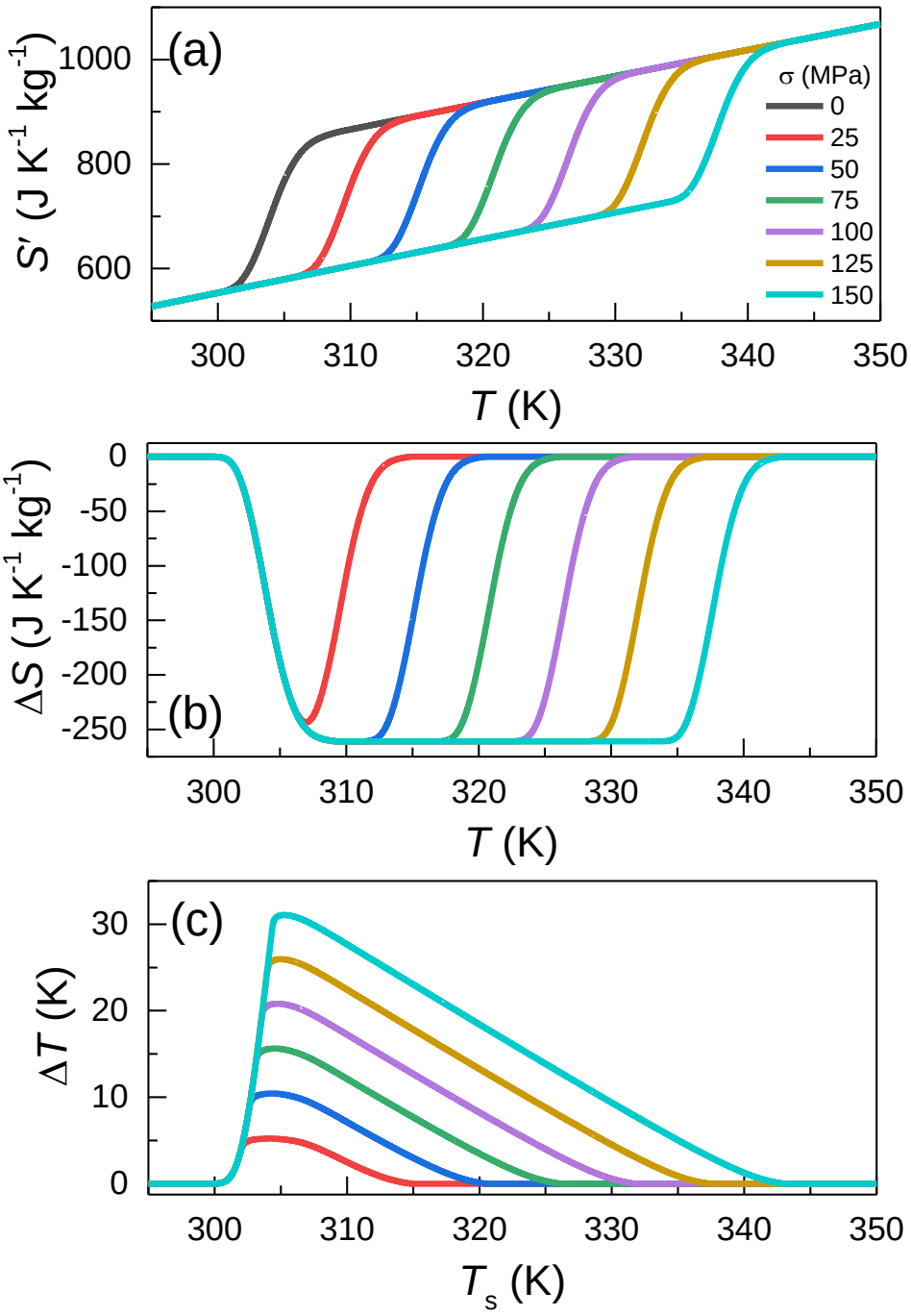

Figure 7.5. Temperature dependencies of (a) isoelastic entropy, (b) isothermal entropy changes and (c) adiabatic temperature changes for different values of applied uniaxial compressive stress in the c-axis direction.

7.4 Evaluation and experimental design

We first pay attention to the reversibility of the eC effect reported here. As our method only predicts the isothermal entropy and adiabatic temperature changes under first application of the stress, we cannot obtain the reversible data and then confidently compare our finding with other materials. However, $C_{10}Mn$ single crystal shows a hysteresis of 4.5 K as defined from the peak maxima, and 1.5 K as defined from the peak onsets, which are both very small. Considering a 30 K adiabatic temperature change achieved under stress change of 150 MPa along the *c*-axis, we believed that such stress is strong enough to drive a full reversible phase transition.

The physical origin of the colossal eC effect in $(C_{10}H_{21}NH_3)_2MnCl_4$ or 2D hybrid perovskites needs to be investigated through experimental or theoretical methods. Recently, the eC effect of $CH_3NH_3PbI_3$ has been studied with molecular dynamics simulations [166]. In this work, Liu and co-workers predicted a giant room-temperature $|\Delta T|$ of 10.7 K for a uniaxial stress change of 550MPa. Such a giant effect can be attributed to the molecular rotations that tend to be stable or ordered under increasing stress. Specifically, the $CH_3NH_3^+$ cations are likely to align with the direction of the applied uniaxial stress, thus limiting their rotation, which considerably reduces the entropy of the crystal.

Since colossal eC effects have been predicted in 2D hybrid perovskites, direct eC characterizations on these materials are highly desirable for revealing their real cooling potential. In practice, most eC materials undergo strong mechanical fatigue and fracture after intensive stretching or compression across their first-order phase transitions. For

2D hybrid materials, Spanopoulos and co-workers investigated out-of-plane mechanical properties by performing nanoindentation measurements [167]. The results demonstrated that their soft and flexible nature can be compared to current commercially available polymer substrates, PMMA for example. This means those materials can be stretched and compressed significantly even with moderate stresses. More importantly, their mechanical properties can be modified by changing the chemical composition. Recently, Xiao and co-workers directly found a reversible ferroelastic domain switching in layered perovskite $(CH_3(CH_2)_3NH_3)_2(CH_3N\text{-}H_3)Pb_2I_7$ single crystals through bending and unbending [168]. Their finding revealed the fact that 2D materials are sensitive to uniaxial stress and those materials show good flexibility.

Based on our evaluation, we proposed a possible direct eC measurement on 2D hybrid materials as shown in Figure 7.6. Normally, single crystal samples are slowly grown in a chemical solution or on a substrate. One can transfer the as-grown crystal to a soft substrate through the use of a hydrophilic polydimethylsiloxane (PDMS) for example. This technique has been widely reported and the details can be found in Refs. 168 and 169. Since the substrate is soft, the uniaxial stress on the crystal can be realized by bending and unbending the PDMS substrate. An infrared camera is proposed to record the surface temperature change of the crystal during loading and unloading. IR cameras can provide fast and precise temperature responses without touching the sample. Hopefully, this proposal can inspire the developments of the direct eC measurements in organic-inorganic hybrid materials.

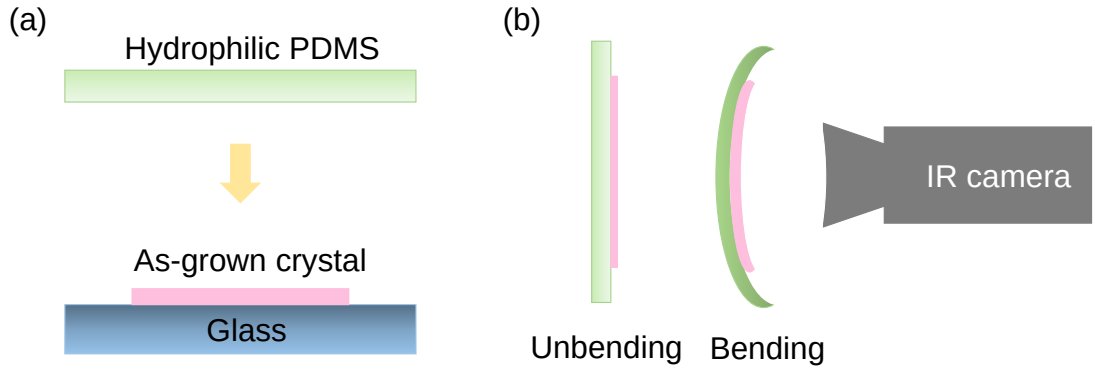

Figure 7.6. (a) Scheme of transferring layered perovskite crystals to soft substrate and applying external stress on crystal, and (b) direct elastocaloric effect measurement through infrared (IR) camera.

7.5 Summary

In this chapter, I have demonstrated colossal elastocaloric effects in the two-dimensional hybrid organic–inorganic perovskites. In particular, $(C_{10}H_{21}NH_3)_2MnCl_4$ undergoes predicted isothermal entropy changes of 260 J K^{-1} kg^{-1} and adiabatic temperature changes of 30 K near room temperature under low uniaxial compressive stress changes of 150 MPa along the *c*-axis direction, which are outstanding compared to other solid-state materials. The origin of this extremely good response is the strong anisotropic effect of lattice deformation in the *c*-axis across a sharp and low-hysteresis first-order solid–solid phase transition. This compound not only widens the horizons for colossal elastocaloric materials to include other compounds beyond the sharp-memory alloys and polymers, but it also expands the limits for the elastocaloric performance in solid-state materials. I also proposed a further direct experiment on this colossal elastocaloric effect.

Chapter 8

Conclusion and Perspectives

Research works within the thesis have successfully answered the initial research question about finding barocaloric effects in molecular crystals with small hysteresis and colossal effects in materials other than plastic crystals. Using pressure-dependent calorimetry, we firstly demonstrate that the molecular crystal C_{60} exhibits outstanding barocaloric properties thanks to its large transition entropy change, small transition hysteresis and high sensitivity of the transition to the applied pressure. Moreover, at moderate pressure changes, giant reversible BC effects are obtained over a very wide temperature range, which expands the operational temperatures around room temperature and suggests its use in regenerative cooling cycles. Then we demonstrate not only that colossal barocaloric effects can be obtained in compounds other than plastic crystals, such as layered hybrid organic-inorganic perovskites, but also that an improved barocaloric performance can be obtained at lower pressure than those reported so far in plastic crystals, due to a very small hysteresis and a very large sensitivity of the transition temperature to pressure. Raman spectroscopy experiments explored changes in structure and dynamics across the transition. Finally, we theoretically found a coloss-

al elastocaloric effect in two-dimensional hybrid perovskites owing to a large anisotropic effect in lattice deformation in the *c*-axis. This predicated colossal elastocaloric effect could elevate the research interests in low-dimensional materials which exhibit anisotropy naturally. Thanks to the mechanical softness of these materials, we proposed a direct method to test the elasocaloric effect. Hopefully, this work can widen the horizons for elastocaloric materials since this area has been dominated by shape-memory alloys for many years.

Ideal barocaloric materials do not exist and an optimal solution is needed. Although we have discovered colossal barocaloric effects under low pressure changes, practical applications may require more. For example, materials with high thermal conductivities are preferred because this could help the cooling devices transfer the heat efficiently. As far as I know, materials with colossal effects always show low thermal conductivities [< 1 W/(m·K)] compared to barocaloric alloys [> 10 W/(m·K)]. As we are looking for economical and environmentally friendly refrigeration methods, the materials themselves should be harmless and economically accessible. Another key problem is the development of cooling prototypes based on barocaloric effects. This is crucial to any cooling techniques because prototypes can truly examine their real capabilities of cooling things down.

For future investigations, further studies on two-dimensional hybrid materials are highly recommended as this family has already shown excellent barocaloric and elastocaloric properties. One can easily modify their chemical composition through a general design principle that has been displayed in our work. In addition, research work on thermal conductivities is also recommended.

Bibliography

[1] J.L. Dupont, P. Domanski, P. Lebrun, and F. Ziegler, "The role of refrigeration in the global economy-38", Informatory Note on Refrigeration Technologies (2019).

[2] C.O. Negrão, and C.J. Hermes, "Energy and cost savings in household refrigerating appliances: A simulation-based design approach", Applied Energy **88**, 3051-3060 (2011).

[3] J.U. Ahamed, R. Saidur and H.H. Masjuki, "A review on exergy analysis of vapor compression refrigeration system", Renewable and Sustainable Energy Reviews **15**, 1593-1600 (2011).

[4] D. Strahan, "Clean cold and the global goals". URL www.birmingham.ac.uk/Documents/college-eps/energy/Publications/Clean-Cold-and-the-Global-Goals. pdf. (2017).

[5] X. Moya, and N.D. Mathur, "Caloric materials for cooling and heating", Science **370**, 797-803 (2020).

[6] K.A. Gschneidner Jr, and V.K. Pecharsky, "Magnetocaloric materials", Annual Review of Materials Science **30**, 387-429 (2000).

[7] L. Mañosa and A. Planes, "Solid-state cooling by stress: A perspective", Applied Physics Letters **116**, 050501 (2020).

[8] C. Cazorla, “Novel mechanocaloric materials for solid-state cooling applications”, Applied Physics Reviews **6**, 041316 (2019).

[9] P. Lloveras and J.L. Tamarit, “Advances and obstacles in pressure-driven solid-state cooling: A review of barocaloric materials”, MRS Energy & Sustainability **8**, 3-15 (2021).

[10] D. Boldrin, “Fantastic barocalorics and where to find them”, Applied Physics Letters **118**, 170502 (2021).

[11] J.F. Scott, “Electrocaloric materials”, Annual Review of Materials Research **41**, 229-240 (2011).

[12] T. Strässle, A. Furrer and K.A. Müller, “Cooling by adiabatic application of pressure–the barocaloric effect”, Physica B: Condensed Matter **276**, 944-945 (2000).

[13] T. Strässle, A. Furrer, A. Dönni and T. Komatsubara, “Barocaloric effect: The use of pressure for magnetic cooling in $Ce_3Pd_{20}Ge_6$”, Journal of applied physics, **91**, 8543-8545 (2002).

[14] L.G. de Medeiros Jr, N.A. de Oliveira, and A. Troper, “Barocaloric and magnetocaloric effects in $La(Fe_{0.89}Si_{0.11})_{13}$”, Journal of Applied Physics **103**, 113909, (2008).

[15] L. Mañosa, D. González-Alonso, A. Planes, E. Bonnot, M. Barrio, J.L. Tamarit, S. Aksoy and M. Acet, “Giant solid-state barocaloric effect in the Ni–Mn–In magnetic shape-memory alloy”, Nature materials **9**, 478-481 (2010).

[16] L. Mañosa, D. Gonzalez-Alonso, A. Planes, M. Barrio, J.L. Tamarit, I.S. Titov, M.Acet, A. Bhattacharyya and S. Majumdar, “Inverse barocaloric effect in the

giant magnetocaloric La–Fe–Si–Co compound", Nature communications **2**, 1-5 (2011).

[17] P. Lloveras, E. Stern-Taulats, M. Barrio, J.L. Tamarit, S. Crossley, W. Li, V. Pomjakushin, A. Planes, L. Mañosa, N.D. Mathur and X. Moya, "Giant barocaloric effects at low pressure in ferrielectric ammonium sulphate", Nature communications **6**, 1-6 (2015).

[18] Y. Liu, J. Wei, P.E. Janolin, I.C. Infante, X. Lou and B. Dkhil, "Giant room-temperature barocaloric effect and pressure-mediated electrocaloric effect in $BaTiO_3$ single crystal", Applied Physics Letters **104**, 162904 (2014).

[19] J.M. Bermudez-Garcia, M. Sanchez-Andujar and M.A. Senaris-Rodriguez, "A new playground for organic–inorganic hybrids: barocaloric materials for pressure-induced solid-state cooling", The Journal of Physical Chemistry Letters **8**, 4419-4423 (2017).

[20] J.M. Bermúdez-García, M. Sánchez-Andújar, S.Castro-García, J. López-Beceiro, R. Artiaga and M.A. Señarís-Rodríguez, "Giant barocaloric effect in the ferroic organic-inorganic hybrid [TPrA][Mn $(dca)_3$] perovskite under easily accessible pressures", Nature communications **8**,1-8 (2017).

[21] J.M. Bermúdez-García, S. Yáñez-Vilar, A. García-Fernández, M. Sánchez-Andújar, S. Castro-García, J. López-Beceiro, R. Artiaga, M. Dilshad, X. Moya and M.A. Señarís-Rodríguez, "Giant barocaloric tunability in $[(CH_3CH_2CH_2)_4N]Cd[N(CN)_2]_3$ hybrid perovskite", Journal of Materials Chemistry C **6**, 9867-9874 (2018).

[22] C. Cazorla and D. Errandonea, “Giant mechanocaloric effects in fluorite-structured superionic materials”, Nano letters **16**, 3124-3129 (2016).

[23] A. Aznar Luque, P. Lloveras, M. Romanini, M.D. Barrio Casado, J.L. Tamarit Mur, C. Cazorla Silva, D. Errandonea Ponce, N.D. Mathur, A. Planes, X. Moya and L. Mañosa Carrera, “Giant barocaloric effects over a wide temperature range in the superionic conductor AgI”, Nature communications **8**, 1-6 (2017).

[24] B. Li, Y. Kawakita, S. Ohira-Kawamura, T. Sugahara, H. Wang, J. Wang, Y. Chen, S.I. Kawaguchi, S. Kawaguchi, K. Ohara and K. Li, “Colossal barocaloric effects in plastic crystals”, Nature **567**, 506-510 (2019).

[25] P. Lloveras, A. Aznar, M. Barrio, P. Negrier, C. Popescu, A. Planes, L. Mañosa, E. Stern-Taulats, A. Avramenko, N.D. Mathur and X. Moya, “Colossal barocaloric effects near room temperature in plastic crystals of neopentylglycol”, Nature communications **10**, 1-7 (2019).

[26] ASHRAE, Chapter 30 Thermophysical properties of refrigerants. ASHRAE Handbook-Fundamentals (SI), 30-1 (2009).

[27] A. Aznar, P. Lloveras, M. Barrio, P. Negrier, A. Planes, L. Mañosa, N.D. Mathur, X. Moya and J.L. Tamarit, “Reversible and irreversible colossal barocaloric effects in plastic crystals”, Journal of Materials Chemistry A **8**, 639-647 (2020).

[28] B. Emre, S. Yüce, E. Stern-Taulats, A. Planes, S. Fabbrici, F. Albertini and L. Mañosa, “Large reversible entropy change at the inverse magnetocaloric effect in Ni-Co-Mn-Ga-In magnetic shape memory alloys”, Journal of Applied Physics **113**, 213905 (2013).

[29] T. Hess, L.M. Maier, N. Bachmann, P. Corhan, O. Schäfer-Welsen, J. Wöllenstein and K. Bartholomé, “Thermal hysteresis and its impact on the efficiency of first-order caloric materials”, Journal of Applied Physics **127**, 075103 (2020).

[30] T. Gottschall, A. Gracia-Condal, M. Fries, A. Taubel, L. Pfeuffer, L. Manosa, A. Planes, K.P. Skokov and O. Gutfleisch, “A multicaloric cooling cycle that exploits thermal hysteresis”, Nature materials **17**, 929-934 (2018).

[31] E. Stern-Taulats, A. Planes, P. Lloveras, M.Barrio, J.L. Tamarit, S. Pramanick, S. Majumdar, S. Yüce, B. Emre, C. Frontera and L. Mañosa, “Tailoring barocaloric and magnetocaloric properties in low-hysteresis magnetic shape memory alloys”, Acta Materialia **96**, 324-332 (2015).

[32] D. Holme, “A description of a property of caoutchouc, or indian rubber; with some reflections on the cause of the elasticity of this substance, In a letter to Dr. Holme”, The Philosophical Magazine **24**, 39-43 (1806).

[33] W. Thomson, “On the thermoelastic and thermomagnetic properties of matter”, Quarterly Journal of Mathematics **1**, 57-77 (1857).

[34] J.P. Joule, “On some thermo-dynamic properties of solids”, Philosophical Trans-actions of the Royal Society of London **149**, 91-131 (1859).

[35] A. Smith, “Who discovered the magnetocaloric effect?”, The European Physical Journal H **38**,507-517 (2013).

[36] P. Weiss and A. Piccard, “Le phénomène magnétocalorique”, Journal of Physics: Theories and Applications **7**, 103-109 (1917).

[37] E. Warburg, “Magnetische untersuchungen”, Annalen der Physik **249**, 141-164 (1881).

[38] P. Kobeko and J. Kurtschatov, “Dielektrische eigenschaften der seignettesalz-kristalle”, Zeitschrift für Physik **66**, 192-205 (1930).

[39] K.A. Müller, F. Fauth, S. Fischer, M. Koch, A. Furrer and P. Lacorre, “Cooling by adiabatic pressure application in $Pr_{1-x}La_xNiO_3$” Applied physics letters **73**, 1056-1058 (1998).

[40] R. Wang, S. Fang, Y. Xiao, E. Gao, N. Jiang, Y. Li, L. Mou, Y. Shen, W. Zhao, S. Li and A.F. Fonseca, “Torsional refrigeration by twisted, coiled, and super-coiled fibers”, Science **366**, 216-221 (2019).

[41] M.M. Vopson, “The multicaloric effect in multiferroic materials”, Solid State Communications **152**, 2067-2070 (2012).

[42] E. Stern-Taulats, T. Castán, L. Mañosa, A. Planes, N.D. Mathur and X. Moya, “Multicaloric materials and effects”, MRS Bulletin **43**, 295-299 (2018).

[43] T. Gottschall, K.P. Skokov, M. Fries, A. Taubel, I. Radulov, F. Scheibel, D. Benke, S. Riegg and O. Gutfleisch, “Making a cool choice: the materials library of magnetic refrigeration”, Advanced Energy Materials **9**, 1901322 (2019).

[44] V.K. Pecharsky and K.A.J. Gschneidner, “Giant Magnetocaloric Effect in $Gd_5Si_2Ge_2$d”, Physical Review Letters **78**, 4494-4497(1997).

[45] K.P. Skokov, A.Y. Karpenkov, D.Y. Karpenkov and O. Gutfleisch, “The maximal cooling power of magnetic and thermoelectric refrigerators with La $(FeCoSi)_{13}$ alloys”, Journal of Applied Physics **113**, 17A945 (2013).

[46] A. Chirkova, K.P. Skokov, L. Schultz, N.V. Baranov, O. Gutfleisch and T.G. Woodcock, “Giant adiabatic temperature change in FeRh alloys evidenced by direct measurements under cyclic conditions”, Acta Materialia **106**, 15-21 (2016).

[47] T, Gottschall, K.P. Skokov, R. Burriel and O. Gutfleisch, “On the S (T) diagram of magnetocaloric materials with first-order transition: Kinetic and cyclic effects of Heusler alloys”, Acta Materialia **107**, 1-8 (2016).

[48] A.S. Mischenko, Q. Zhang, J.F. Scott, R.W. Whatmore and N.D. Mathur, “Giant electrocaloric effect in thin-film $PbZr_{0.95}Ti_{0.05}O_3$”, Science **311**, 1270-1271 (2016).

[49] B. Neese, B. Chu, S.G. Lu, Y. Wang, E. Furman and Q.M. Zhang, “Large electrocaloric effect in ferroelectric polymers near room temperature”, Science **321**, 821-823 (2008).

[50] X. Moya, E. Stern-Taulats, S. Crossley, D. González-Alonso, S. Kar-Narayan, A. Planes, L. Mañosa and N.D. Mathur, “Giant electrocaloric strength in single-crystal $BaTiO_3$”, Advanced materials **25**, 1360-1365 (2013).

[51] B. Nair, T. Usui, S. Crossley, S. Kurdi, G.G. Guzmán-Verri, X. Moya, S. Hirose and N.D. Mathur, “Large electrocaloric effects in oxide multilayer capacitors over a wide temperature range”, Nature **575**, 468-472 (2019).

[52] Y. Chen, J. Qian, J. Yu, M. Guo, Q. Zhang, J. Jiang, Z. Shen, L.Q. Chen and Y. Shen, “An All-Scale Hierarchical Architecture Induces Colossal Room-Temperature Electrocaloric Effect at Ultralow Electric Field in Polymer Nanocomposites”, Advanced Materials **32**, 1907927 (2020).

[53] J. Tušek, K. Engelbrecht, R. Millán-Solsona, L. Manosa, E. Vives, L.P. Mikkelsen and N. Pryds, “The elastocaloric effect: a way to cool efficiently”, Advanced Energy Materials **5**, 1500361 (2015).

[54] H. Chen, F. Xiao, X. Liang, Z. Li, Z. Li, X. Jin and T. Fukuda, “Giant elastocaloric effect with wide temperature window in an Al-doped nanocrystalline Ti–Ni–Cu shape memory alloy”, Acta Materialia **177**, 169-177 (2019).

[55] D. Cong, W. Xiong, A. Planes, Y. Ren, L.Mañosa, P. Cao, Z. Nie, X. Sun, Z. Yang, X. Hong and Y. Wang, “Colossal elastocaloric effect in ferroelastic Ni-Mn-Ti alloys”, Physical review letters **122**, 255703 (2019).

[56] G. Coativy, H. Haissoune, L. Seveyrat, G. Sebald, L. Chazeau, J.M. Chenal and L. Lebrun, “Elastocaloric properties of thermoplastic polyurethane”, Applied Physics Letters **117**, 193903 (2020).

[57] Z. Xie, G. Sebald and D. Guyomar, “Temperature dependence of the elastocaloric effect in natural rubber”, Physics Letters A **381**, 2112-2116 (2017).

[58] A. Aznar, A. Gràcia-Condal, A. Planes, P. Lloveras, M. Barrio, J.L.Tamarit, W. Xiong, D. Cong, C. Popescu and L. Mañosa, “Giant barocaloric effect in all-d-metal Heusler shape memory alloys”, Physical Review Materials **3**, 044406 (2019).

[59] M. Romanini, Y.Wang, K. Gürpinar, G. Ornelas, P. Lloveras, Y. Zhang, W. Zheng, M. Barrio, A. Aznar, A. Gràcia-Condal and B. Emre, “Giant and Reversible Barocaloric Effect in Trinuclear Spin-Crossover Complex $Fe_3(bntrz)_6(tcnset)_6$”, Advanced Materials **33**, 2008076 (2021).

[60] X. Moya, S. Kar-Narayan and N.D. Mathur, “Caloric materials near ferroic phase transitions”, Nature materials **13**, 439-450 (2014).

[61] J. Shi, D. Han, Z. Li, L. Yang, S.G. Lu, Z. Zhong, J. Chen, Q.M. Zhang and X. Qian, “Electrocaloric cooling materials and devices for zero-global-warming-potential, high-efficiency refrigeration”, Joule **3**, 1200-1225 (2019).

[62] A. Torelló, P. Lheritier, T. Usui, Y. Nouchokgwe, M. Gérard, O. Bouton, S. Hirose and E. Defay, “Giant temperature span in electrocaloric regenerator” Science **370**, 125-129 (2020).

[63] Y. Wang, Z. Zhang, T. Usui, M. Benedict, S. Hirose, J. Lee, J. Kalb and D. Schwartz, “A high-performance solid-state electrocaloric cooling system”, Science **370**, 129-133 (2020).

[64] K. Engelbrecht, “Future prospects for elastocaloric devices”, Journal of Physics: Energy **1**, 021001 (2019).

[65] J. Chen, L. Lei and G. Fang, “Elastocaloric cooling of shape memory alloys: A review”, Materials Today Communications **28**, 102706 (2021).

[66] A. Chauhan, S. Patel, R. Vaish and C.R. Bowen, “A review and analysis of the elasto-caloric effect for solid-state refrigeration devices: Challenges and opportunities”, MRS Energy & Sustainability 2 (2015).

[67] J. Quarini and A. Prince, “Solid state refrigeration: Cooling and refrigeration using crystalline phase changes in metal alloys”, Proceedings of the Institution of Mechanical Engineers, Part C: Journal of Mechanical Engineering Science **218**, 1175-1179 (2004).

[68] W.H. Dos Santos, C.Y. Iguchi, and Jr, R. Gregorio, “Thermal properties of poly (vinilidene fluoride) in the temperature range from 25 to 210 °C”, Polymer testing **27**, 204-208 (2008).

[69] A. Kitanovski, J. Tušek, U. Tomc, U. Plaznik, M. Ožbolt and A. Poredoš, “The thermodynamics of magnetocaloric energy conversion”, In Magnetocaloric Energy Conversion, Green Energy and Technology. Springer, Cham, 1-21(2015).

[70] Y. Liu, “Multicaloric effect in ferroic materials”, (Doctoral dissertation, Université Paris-Saclay), (2016).

[71] A. Greco, C. Aprea, A. Maiorino and C. Masselli, “A review of the state of the art of solid-state caloric cooling processes at room-temperature before 2019”, International Journal of Refrigeration **106**, 66-88 (2019).

[72] D.S. Arnold, A. Tura, A. Ruebsaat-Trott and A. Rowe, “Design improvements of a permanent magnet active magnetic refrigerator”, International Journal of Refrigeration **37**, 99-105 (2014).

[73] E. Stern Taulats, “Giant caloric effects in the vicinity of first-order phase transitions”, (Doctoral dissertation, Universitat de Barcelona), (2017).

[74] A. Planes, T. Castan and A. Saxena, “Thermodynamics of multicaloric effects in multiferroics”, Philosophical Magazine **94**, 1893-1908 (2014).

[75] A. Giguere, M. Foldeaki, B.R. Gopal, R. Chahine, T.K. Bose, A. Frydman and J.A. Barclay, “Direct measurement of the “giant” adiabatic temperature change in $Gd_5Si_2Ge_2$”, Physical Review Letters **83**, 2262 (1999).

[76] J.R. Sun, F.X. Hu and B.G. Shen, “Comment on “Direct Measurement of theGiant'Adiabatic Temperature Change in $Gd_5Si_2Ge_2$”, Physical review letters **85**, 4191 (2000).

[77] M. Földeaki, R. Chahine, T.K. Bose and J.A. Barclay, “Földeàki et al. Reply”, Physical review letters **85**, 4192 (2000).

[78] A.J. Meyer and P. Taglang, “Influence du champ magnétique sur une transformation polymorphique d'un ferromagnétique”, Journal de Physique et le Radium **14**, 82-84 (1953).

[79] A. Planes, L. Mañosa and M. Acet, “Magnetocaloric effect and its relation to shape-memory properties in ferromagnetic Heusler alloys”, Journal of Physics: Condensed Matter **21**, 233201 (2009).

[80] P.A. Domanski, J.S. Brown, J. Heo, J. Wojtusiak and M.O. McLinden, “A thermodynamic analysis of refrigerants: Performance limits of the vapor compression cycle”, International journal of refrigeration **38**, 1-79 (2014).

[81] J. Cui, Y.S Chu, O.O. Famodu, Y. Furuya, J. Hattrick-Simpers, R.D. James, A. Ludwig, S. Thienhaus, M. Wuttig, Z. Zhang and I. Takeuchi, “Combinatorial search of thermoelastic shape-memory alloys with extremely small hysteresis width”, Nature materials **5**, 286-290 (2006).

[82] J. Lin, P. Tong, X. Zhang, Z. Wang, Z. Zhang, B. Li, G. Zhong, J. Chen, Y. Wu, H. Lu and L. He, “Giant room-temperature barocaloric effect at the electronic phase transition in $Ni_{1-x}Fe_xS$”, Materials Horizons **7**, 2690-2695 (2010).

[83] Z. Zhang, K. Li, S. Lin, D. Yu, R. Song, Y. Wang, I. Wang, S. Kawaguchi, Z. Zhang, C. Yu and X. Li, “Barocaloric thermal batteries”, arXiv preprint arXiv:2103.04348 (2021).

[84] E. Brück, H. Yibole and L. Zhang, “A universal metric for ferroic energy materials”, Philosophical Transactions of the Royal Society A: Mathematical, Physical and Engineering Sciences **374**, 20150303 (2016).

[85] J. Lin, P. Tong, K. Tao, W. Lu, X. Zhang, W. Song and Y. Sun, "Colossal and Reversible Barocaloric Effect in Phase Change Materials n-Alkanes", (2021).

[86] J.D. Menczel, L. Judovits, R.B. Prime, H.E. Bair, M. Reading and S. Swier, "Differential scanning calorimetry (DSC)", Thermal analysis of polymers: Fundamentals and applications **7**, 239 (2009).

[87] W. Li, R.D. Sherwood, D.M. Cox and M. Radosz, "PVT Measurements on Fullerite from 30 to 330 °C and Pressure to 200 MPa", Journal of Chemical and Engineering Data **39**, 467-469 (1994).

[88] V.V. Diky, L.S. Zhura, A.G. Kabo, V.Y. Markov and G.J. Kabo, "High-temperature heat capacity of C_{60} fullerene", Fullerene science and technology **9**, 543-551 (2001).

[89] H.W. Kroto, A.W. Allaf and S.P. Balm, "C_{60}: Buckminsterfullerene", Chemical Reviews **91**, 1213-1235 (1991).

[90] L. Forró and L. Mihály, "Electronic properties of doped fullerenes", Reports on Progress in Physics **64**, 649 (2001).

[91] M. Haluška, H. Kuzmany, M. Vybornov, P. Rogl and P. Fejdi, "A double-temperature-gradient technique for the growth of single-crystal fullerites from the vapor phase", Applied Physics A **56**, 161-167 (1993).

[92] C.S. Yannoni, P.P.Bernier, D.S. Bethune, G. Meijer and J.R. Salem, "NMR determination of the bond lengths in C_{60}", Journal of the American Chemical Society **113**, 3190-3192 (1991).

[93] R. Moret, P. Launois, P.A. Persson and B. Sundqvist, “First X-ray diffraction analysis of pressure polymerized C_{60} single crystals”, EPL (Europhysics Letters) **40**, 55 (1997).

[94] K.P. Meletov, D. Christofilos, S. Ves and G.A. Kourouklis, “Pressure-induced orientational ordering in C_{60} single crystals studied by Raman spectroscopy”, Physical Review B **52**, 10090 (1995).

[95] F. Wudl, “The chemical properties of buckminsterfullerene (C_{60}) and the birth and infancy of fulleroids”. Accounts of chemical research **25**, 157-161 (1992).

[96] D. Jonsson, P. Norman, K. Ruud, H. Ågren and T. Helgaker, “Electric and magnetic properties of fullerenes”, The Journal of chemical physics **109**, 572-577 (1998).

[97] L.S. Fomenko, S.V. Lubenets, A.N. Izotov, R.K. Nikolaev and N.S. Sidorov, “Mechanical properties of C_{60} single crystals” Materials Science and Engineering: A **400**, 320-324 (2005).

[98] R.C. Yu, N. Tea, M.B. Salamon, D. Lorents and R. Malhotra, “Thermal conductivity of single crystal C_{60}”, Physical review letters **68**, 2050 (1992).

[99] A.R. Kortan, “Superconductivity at 18 K in potassium-doped C_{60}”, Nature **350**, 600-601 (1991).

[100] P.A. Heiney, “Structure, dynamics and ordering transition of solid C60”, Journal of Physics and Chemistry of Solids **53**, 1333-1352 (1992).

[101] G.A. Samara, J.E. Schirber, B. Morosin, L.V. Hansen, D. Loy and A.P. Sylwester, “Pressure dependence of the orientational ordering in solid C_{60}”, Physical review letters **67**, 3136 (1991).

[102] I.O. Bashkin, V.I. Rashchupkin, A.F. Gurov, A.P. Moravsky, O.G.Rybchenkot, N.P. Kobelev, Y.M. Soifer and E.G. Ponyatovsky, "A new phase transition in the TP diagram of C_{60} fullerite", Journal of Physics: Condensed Matter **6**, 7491 (1994).

[103] W. David, R.M. bberson, T.J.S. Dennis, J.P.Hare and K. Prassides, "Structural phase transitions in the fullerene C_{60}", EPL (Europhysics Letters) **18**, 219 (1992).

[104] R. Sengupta, M. Bhattacharya, S. Bandyopadhyay and A.K Bhowmick, "A review on the mechanical and electrical properties of graphite and modified graphite reinforced polymer composites", Progress in polymer science **36**, 638-670 (2011).

[105] E.A. Ekimov, V.A. Sidorov, E.D. Bauer, N.N. Mel'Nik, N.J. Curro, J.D. Thompson and S.M. Stishov, "Superconductivity in diamond", Nature **428**, 542-545 (2004).

[106] M.J Allen, V.C. Tung and R.B. Kaner, "Honeycomb carbon: a review of graphene", Chemical reviews **110**, 132-145 (2010).

[107] A.K. Geim and K.S. Novoselov, "The rise of graphene", Nature Materials **6**, 183–191 (2007).

[108] Z. Wu, Z. Chen, X. Du, J.M. Logan, J. Sippel, M. Nikolou, K. Kamaras, J.R. Reynolds, D.B. Tanner, A.F. Hebard and A.G. Rinzler, "Transparent, conductive carbon nanotube films", Science **305**, 1273-1276 (2004).

[109] J. Hone, M..C. Llaguno, N.M. Nemes, A.T. Johnson, J.E. Fischer, D.A. Walters, M.J. Casavant, J. Schmidt and R.E. Smalley, "Electrical and thermal transport properties of magnetically aligned single wall carbon nanotube films", Applied physics letters **77**, 666-668 (2000).

[110] M. Prato, “Fullerene chemistry for materials science applications”, Journal of Materials Chemistry **7**, 1097-1109 (1997).

[111] S. Lisenkov, R. Herchig, S. Patel, R. Vaish, L. Cuozzo and I. Ponomareva, “Elastocaloric effect in carbon nanotubes and graphene”, Nano letters *16*, 7008-7012 (2016).

[112] M.S. Reis and S. Soriano, “Electrocaloric effect on graphenes”, Applied Physics Letters **102**, 112903 (2013).

[113] N. Ma and M.S. Reis, “Barocaloric effect on graphene”, Scientific reports **7**, 1-8 (2017).

[114] D. André, A. Dworkin, H. Szwarc, R. Céolin, V. Agafonov, C. Fabre, A. Rassat, L. Straver, P. Bernier and A. Zahab, “Molecular packing of fullerene C_{60} at room temperature”, Molecular Physics **76**, 1311-1317(1992).

[115] Y. Miyazaki, M. Sorai, R. Lin, A. Dworkin, H. Szwarc and J. Godard, “Heat capacity of a giant single crystal of C_{60}”, Chemical physics letters **305**, 293-297 (1999).

[116] G.A. Samara, L.V. Hansen, R.A. Assink, B. Morosin, J.E. Schirber and D. Loy, “Effects of pressure and ambient species on the orientational ordering in solid C_{60}”, Physical Review B **47**, 4756 (1993).

[117] J.E. Fischer, A.R. McGhie, J.K. Estrada, M. Haluška, H. Kuzmany and H.U. Ter Meer, “Heat capacity and the orientational transition in solid C_{60}”, Physical Review B **53**, 11418 (1996).

[118] N.P. Kobelev, R.K. Nikolaev, N.S. Sidorov and Y.M.Soifer, "Temperature dependence of elastic moduli for solid C_{60}", Physics of the Solid State **43**, 2344-2350 (2001).

[119] A. Lundin and B. Sundqvist, "Compressibility of C_{60} between 150 and 335 K and up to 1 GPa", EPL (Europhysics Letters) **27**, 463 (1994).

[120] A. Aznar, P. Lloveras, J.Y. Kim, E. Stern-Taulats, M. Barrio, J.L. Tamarit, C.F. Sánchez-Valdés, J.L. Sánchez Llamazares, N.D. Mathur and X. Moya, "Giant and reversible inverse barocaloric effects near room temperature in ferromagnetic $MnCoGeB_{0.03}$", Advanced Materials **31**, 1903577 (2019).

[121] L. Mao, C.C. Stoumpos and M.G. Kanatzidis, "Two-dimensional hybrid halide perovskites: principles and promises", Journal of the American Chemical Society **141**, 1171-1190 (2018).

[122] D.B. Mitzi, "Templating and structural engineering in organic–inorganic perovskites", Journal of the Chemical Society, Dalton Transactions 1-12 (2001).

[123] W.W. Zhong, Y.Y. Di, Y.X. Kong, D.F. Lu and J.M. Dou, "Lattice potential energies and thermochemical properties of phase change materials $(1\text{-}C_nH_{2n+1}NH_3)_2MnCl_4$(s) (n=10 and 11)", The Journal of Chemical Thermodynamics **72**, 100-107 (2014).

[124] R. Blinc, M. Burgar, B. Lozar, J. Seliger, J. Slak, V. Rutar, H. Arend and R. Kind, "Proton NMR study of the structural phase transitions in perovskite layer compounds:$(C_nH_{2n+1}NH_3)_2CdCl_4$ and $(NH_3\text{–}(CH_2)_n\text{–}NH_3)CdCl_4$", The Journal of Chemical Physics **66**, 278-287 (1977).

[125] K.J. Schenk and G. Chapuis, “Thermotropic phase transitions in bis (n-tetradecylammonium) tetrachlorocadmate (II) and some homologous compounds”, The Journal of Physical Chemistry **92**, 141-147 (1988).

[126] G.F. Needham, R.D. Willett and H.F. Franzen, “Phase transitions in crystalline models of bilayers. 1. Differential scanning calorimetric and x-ray studies of $(C_{12}H_{25}NH_3)_2MCl_4$ and $(NH_3C_{14}H_{29}NH_3)_2MCl_4$ salts ($M=Mn^{2+}$, Cd^{2+}, Cu^{2+})”, The Journal of Physical Chemistry **88**, 674-680 (1984).

[127] V. Busico, C. Carfagna, V. Salerno, M. Vacatello and F. Fittipaldi, “The layer perovskites as thermal energy storage systems”, Solar Energy **24**, 575-579 (1980).

[128] R. Kind, S. Pleško, H. Arend, R. Blinc, B. Žekš, J. Seliger, B. Ložar, J. Slak, A. Levstik, C. Filipič and V. Žagar, “Erratum: Dynamics of the n-decylammonium chains in the perovskite-type layer structure compound $(C_{10}H_{21}NH_3)_2CdCl_4$) [J. Chem. Phys. 7 1, 2118 (1979)]”, The Journal of Chemical Physics **73**, 1482-1482 (1980).

[129] W. Li, Z. Wang, F. Deschler, S. Gao, R.H. Friend and A.K. Cheetham, “Chemically diverse and multifunctional hybrid organic–inorganic perovskites”, Nature Reviews Materials **2**, 1-18 (2017).

[130] M.M. Kenisarin and K.M. Kenisarina, “Form-stable phase change materials for thermal energy storage”, Renewable and Sustainable Energy Reviews **16**, 1999-2040 (2012).

[131] M. Szafrański, W.J. Wei, Z.M. Wang, W. Li and A. Katrusiak, “Research Update: Tricritical point and large caloric effect in a hybrid organic-inorganic perovskite”, APL Materials **6**, 100701 (2018).

[132] S.P. Vallone, A.N. Tantillo, A.M. Dos Santos, J.J. Molaison, R. Kulmaczewski, A. Chapoy, P. Ahmadi, M.A. Halcrow and K.G. Sandeman, "Giant barocaloric effect at the spin crossover transition of a molecular crystal", Advanced Materials **31**, 1807334 (2019).

[133] D.K. Benson, R.W. Burrows and J.D. Webb, "Solid state phase transitions in pentaerythritol and related polyhydric alcohols", Solar Energy Materials **13**, 133-152 (1986).

[134] K.W. Lee and C.E. Lee, "Magnetic resonance study of the two-dimensional spin diffusion in the Heisenberg paramaget $(C_{18}H_{37}NH_3)_2MnCl_4$", Solid state communications **126**, 343-346 (2003).

[135] H. Van Kempen, F.H. Mischgofsky and P. Wyder, "Magneto-optical observations of the magnetic domains in the nearly-two-dimensional Heisenberg ferromagnet $(C_3H_7NH_3)_2CuBr_4$", Physical Review B **15**, 4386 (1977).

[136] T. Nakajima, H. Yamauchi, T. Goto, M. Yoshizawa, T. Suzuki and T. Fujimura, "Magnetic and elastic properties of $(CH_3NH_3)_2FeCl_4$ and $(C_2H_5NH_3)_2FeCl_4$", Journal of Magnetism and Magnetic Materials **31**,1189-1190 (1983).

[137] A. Aznar, P. Negrier, A. Planes, L. Mañosa, E. Stern-Taulats, X. Moya, M. Barrio, J.L. Tamarit and P. Lloveras, "Reversible colossal barocaloric effects near room temperature in 1-X-adamantane (X=Cl, Br) plastic crystals", Applied Materials Today **23**, 101023 (2021).

[138] C.R. Raj, S. Suresh, R.R. Bhavsar, V.K. Singh, A.S. Reddy and A. Upadhyay, "Manganese-based layered perovskite solid–solid phase change material: Synthesis, characterization and thermal stability study", Mechanics of Materials **135**, 88-97 (2019).

[139] H.M. Rietveld, "A profile refinement method for nuclear and magnetic structures", Journal of applied Crystallography **2**, 65-71 (1969).

[140] A.A. Coelho, "TOPAS and TOPAS-Academic: an optimization program integrating computer algebra and crystallographic objects written in C++", Journal of Applied Crystallography **51**, 210-218 (2018).

[141] M.R. Ciajolo and C. MR, "Comparative studies of layer structures: The crystal structure of bi(monodecylammonium) tetrachloromanganate (II)", Gazzetta Chimica Italiana **106**, 807-806 (1976).

[142] M. Vacatello, "Relationships between structure and properties of compounds of the type $(RNH_3)_2MX_4$. I. compounds with M=Mn, X=Cl and R=N-$C_{10}H_{21}$, N-$C_{12}H_{25}$, N-$C_{14}H_{29}$, and N-$C_{16}H_{33}$", Gazzetta Chimica Italiana **103**,1027-1036 (1973).

[143] A. Schaufele and T. Shimanouchi, "Longitudinal acoustical vibrations of finite polymethylene chains", The Journal of Chemical Physics **47**, 3605-3610 (1967).

[144] W.L. Peticolas, G.W. Hibler, J.L. Lippert, A. Peterlin and H. Olf, "Raman scattering from longitudinal acoustical vibrations of single crystals of polyethylene", Applied Physics Letters **18**, 87-89 (1971).

[145] A. Masters, “The LAM-1 band in the low-frequency Raman spectra of even and odd monosubstituted n-alkanes”, Physical Chemistry Chemical Physics **1**, 415-419 (1999).

[146] J.R. Scherer and R.G. Snyder, “Raman spectra of liquid n-alkanes. II. Longitudinal acoustic modes and the gauche–trans energy difference”, The Journal of Chemical Physics **72**, 5798-5808 (1980).

[147] L. Ricard, R. Cavagnat and M. Rey-Lafon, “Vibrational study of the dynamics of n-alkylammonium chains in the perovskite-type layer compounds $(C_nH_{2n+1}NH_3)_2CdCl_4$ (n = 8, 12, 16)”, The Journal of Physical Chemistry **89**, 4887-4894 (1985).

[148] H.L. Casal, D.G. Cameron and H.H. Mantsch, “A vibrational spectroscopic characterization of the solid-phase behavior of n-decylammonium chloride (n-$C_{10}H_{21}NH_3Cl$) and bis (n-decylammonium) tetrachlorocadmate [(n-$C_{10}H_{21}NH_3)_2CdCl_4$]”, The Journal of Physical Chemistry **89**, 5557-5565 (1985).

[149] Y. Abid, M. Kamoun, A. Daoud and F. Romain, “Vibrational study of phase transitions in $(C_3H_7NH_3)_2PbCl_4$”, Journal of Raman spectroscopy **21**, 709-716 (1990).

[150] F. Guillaume, G. Coddens, A.J. Dianoux, W. Petry, M. Rey-Lafon and C. Sourisseau, “Molecular motions of decylammonium chains in the perovskite type layered compound $(C_{10}H_{21}NH_3)_2MnCl_4$: An incoherent neutron scattering study”, Molecular Physics **67**, 665-679 (1989).

[151] W. Depmeier, “The uniqueness of the propyl compound in the series $(C_nH_{2n+1}NH_3)_2MnCl_4$ with n=1–10”, Journal of Solid-State Chemistry **29**, 15-26 (1979).

[152] J.D. Gault, H.A. Gallardo and H. J. Müler, “Thermotropic mesophases of the C8, C10, C12 and C16 n-alkyl ammonium chlorides”, Molecular Crystals and Liquid Crystals **130**, 163-177 (1985).

[153] S. Steinert, W. Voigt, R. Glausch and M. Neuschütz, “Thermal characteristics of solid–solid phase transitions in long-chain dialkyl ammonium salts”, Thermochimica acta **435**, 28-33 (2005).

[154] J. Mason, J.Seo, R. McGillicuddy, A. Slavney, S. Zhang, A. Yakovenko and S.L. Zheng, “Colossal Barocaloric Effects with Ultralow Hysteresis in Two-Dimensional Metal–Halide Perovskites”, (2021).

[155] N.B. Chanh, C. Lartigue-Bourdeau, M. Khechoubi, J.K. Kang, J.H. Choy and M. Rey-Lafon, “Structural and Vibrational Study of the Phase Transitions in Crystalline bis (n-decylammonium) tetrachlorocuprate”, Molecular Crystals and Liquid Crystals Science and Technology. Section A. Molecular Crystals and Liquid Crystals **238**, 93-108 (1994).

[156] M. Gorev, E. Bogdanov, I. Flerov and N. Laptash, “Thermal expansion, phase diagrams and barocaloric effects in $(NH_4)_2NbOF_5$”, Journal of Physics: Condensed Matter **22**, 185901 (2010).

[157] E. Mikhaleva, M. Gorev, V. Bondarev, E. Bogdanov and I. Flerov, “Comparative analysis of elastocaloric and barocaloric effects in single-crystal and ceramic ferroelectric $(NH_4)_2SO_4$”, Scripta Materialia **191**, 149-154 (2021).

[158] E.A. Mikhaleva, I.N. Flerov, E.V. Bogdanov, V.S. Bondarev, M.V. Gorev and E. Rysiakiewicz-Pasek, “Size effect on sensitivity to external pressure and caloric

effects in TGS: Ceramics and nanocomposites", Materials Today Communications **25**, 101463 (2020).

[159] E.A. Mikhaleva, M.V. Gorev, M.S. Molokeev, A.V. Kartashev and I.N. Flerov, "Anisotropy of piezocaloric effect at ferroelectric phase transitions in ammonium hydrogen sulphate", Journal of Alloys and Compounds **839**, 155085 (2020).

[160] E. Bonnot, R. Romero, L. Mañosa, E. Vives and A. Planes, "Elastocaloric effect associated with the martensitic transition in shape-memory alloys", Physical review letters **100**, 125901 (2008).

[161] R. Millán-Solsona, E. Stern-Taulats, E. Vives, A. Planes, J. Sharma, A.K. Nayak, K.G. Suresh and L. Mañosa, "Large entropy change associated with the elastocaloric effect in polycrystalline Ni-Mn-Sb-Co magnetic shape memory alloys", Applied Physics Letters **105**, 241901 (2014).

[162] A. Gràcia-Condal, E. Stern-Taulats, A. Planes, E. Vives and L. Mañosa, "The Giant Elastocaloric Effect in a Cu–Zn–Al Shape-Memory Alloy: a Calorimetric Study", physica status solidi (b) **255**, 1700422 (2018).

[163] A. Gràcia-Condal, E. Stern-Taulats, A. Planes and L. Mañosa, "Caloric response of Fe 49 Rh 51 subjected to uniaxial load and magnetic field", Physical Review Materials **2**, 084413 (2018).

[164] A. Gràcia-Condal, T. Gottschall, L. Pfeuffer, O. Gutfleisch, A. Planes and L. Mañosa, "Multicaloric effects in metamagnetic Heusler Ni-Mn-In under uniaxial stress and magnetic field", Applied Physics Reviews **7**, 041406 (2020).

[165] C. Cazorla and D. Errandonea, "Giant mechanocaloric effects in fluorite-structured superionic materials", Nano letters **16**, 3124-3129 (2016).

[166] S. Liu and R.E. Cohen, “Response of methylammonium lead iodide to external stimuli and caloric effects from molecular dynamics simulations”, The Journal of Physical Chemistry C **120**, 17274-17281 (2016).

[167] I. Spanopoulos, I. Hadar, W. Ke, Q. Tu, M. Chen, H. Tsai, Y. He, G. Shekhawat, V.P. Dravid, M.P. Wasielewski and A.D. Mohite, “Uniaxial expansion of the 2D Ruddlesden–Popper perovskite family for improved environmental stability”, Journal of the American Chemical Society **141**, 5518-5534 (2019).

[168] X. Xiao, J. Zhou, K. Song, J. Zhao, Y. Zhou, P.N. Rudd, Y. Han, J. Li and J. Huang, “Layer number dependent ferroelasticity in 2D Ruddlesden–Popper organic-inorganic hybrid perovskites”, Nature communications **12**, 1-6 (2021).

[169] C. Kim,M.A. Yoon, B. Jang, H.D. Kim, J.H. Kim, A.T. Hoang, J.H. Ahn, H.J. Jung, H.J. Lee and K.S. Kim, “Damage-free transfer mechanics of 2-dimensional materials: competition between adhesion instability and tensile strain”, NPG Asia Materials **13**, 1-11 (2021).

Publications

[1] **Li, Junning**, David J. Dunstan, Xiaojie Lou, Antoni Planes, Lluís Mañosa, María Barrio, Josep-Lluis Tamarit, and Pol Lloveras. "Reversible barocaloric effects over a large temperature span in fullerite C 60." Journal of Materials Chemistry A **8**, 20354-20362 (2020).

[2] **Li, Junning**, María Barrio, David J. Dunstan, Richard Dixey, Xiaojie Lou, Josep-Lluís Tamarit, Anthony E. Phillips, and Pol Lloveras. "Colossal Reversible Barocaloric Effects in Layered Hybrid Perovskite (C10H21NH3) 2MnCl4 under Low Pressure Near Room Temperature." Advanced Functional Materials **31**, 2105154 (2021).

[3] **Li, Junning**. The effect of anisotropy on caloric response in two-dimensional hybrid organic-inorganic perovskite" 2021 (in preparation)

Appendix A

X-ray powder diffraction patterns and structure information

The X-ray powder diffraction data were performed and analysed by pattern matching by Dr. María Barrio at Universitat Politècnica de Catalunya.

Dr. Anthony Phillips and Dr. Richard Dixey in the Centre for Condensed Matter and Materials Physics at Queen Mary University of London performed Rietveld Refinement in the X-ray data analysis.

Figure A1: X-ray powder diffraction data of C_{60}.

Figure A2-A6: X-ray powder diffraction data of $(C_{10}H_{21}NH_3)_2MnCl_4$.

Data in Figure A6 was collected and analysed by myself.

X-Ray Diffraction:

X-ray diffraction patterns were obtained using two diffractometers. A Siemens D5000 X-ray powder diffractometer operating in transmission mode, with monochromatic Cu-Kα1 radiation was employed to check the purity of the synthesized samples because impurities had been reported to modify thermodynamic transition data.[22] An INEL X-ray powder diffractometer operating in transmission mode, with Cu-Kα1 = 1.5406 Å radiation, a curved position-sensitive detector (CPS120), a 0.5-mm-diameter Lindemann capillary and a 700 series Oxford Cryostream Cooler to control the temperature were used to perform temperature-dependent high-resolution X-ray powder diffraction measurements at atmospheric pressure and different temperatures.

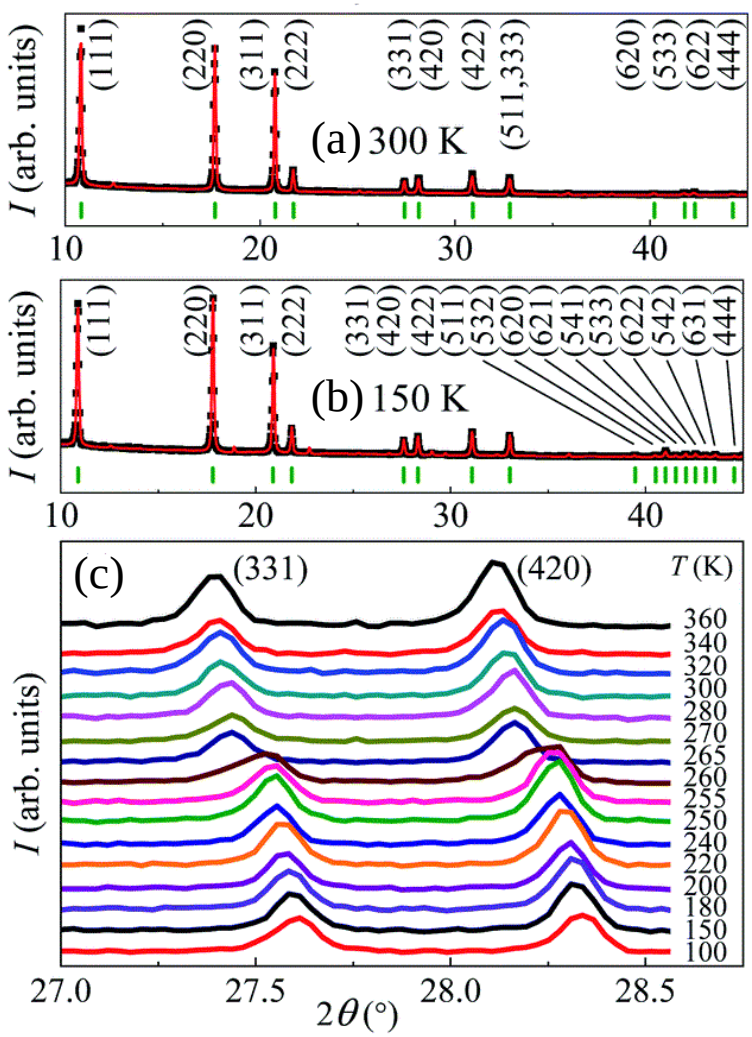

Figure A1. (a and b) X-ray powder diffraction patterns recorded at 300 K and 150 K, corresponding to the fcc and sc phases, respectively, in the interval 2θ = (10, 45)°. Black symbols correspond to experimental data, red lines are calculated patterns *via* a pattern matching fitting procedure and green lines indicate the position of the Bragg peaks, whose (*hkl*) Miller indices are indicated on top of each panel. (c) Temperature evolution of the (331) and (420) Bragg peaks well above, across, and well below the phase transition.

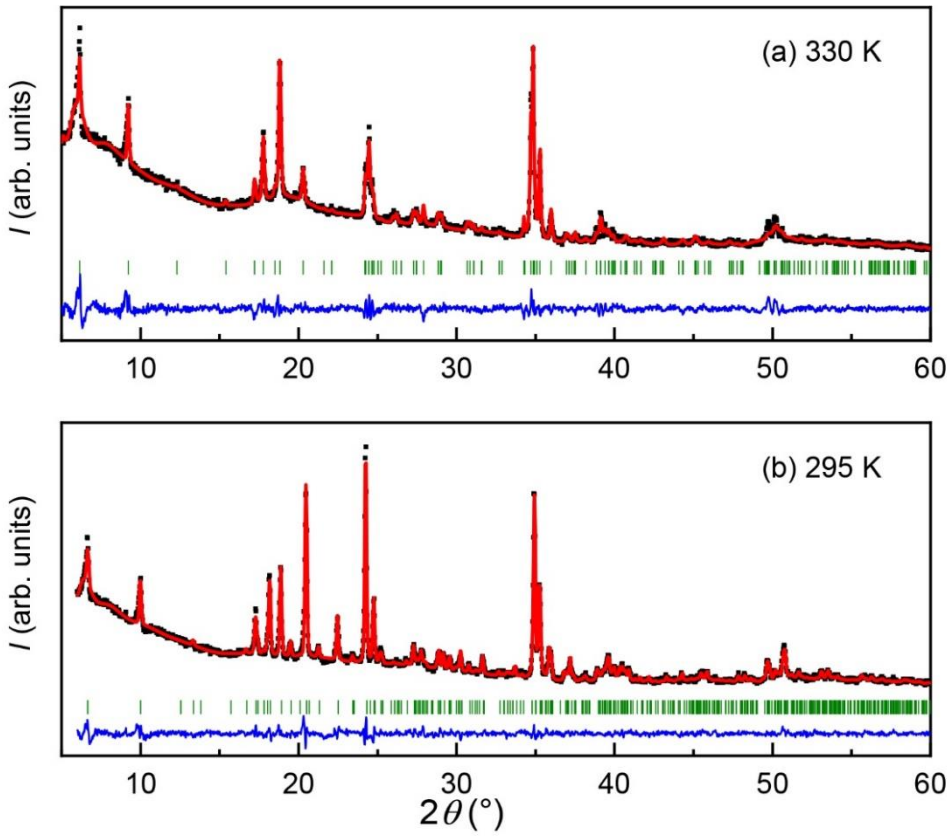

Figure A2. X-ray powder diffraction patterns obtained at (a) T = 330 K (high- temperature phase *C*2/*m*) and (b) T = 295 K (low-temperature phase $P2_1/a$). Black symbols correspond to experimental data, red lines correspond to calculated patterns via pattern matching, blue lines correspond to the difference between experimental and calculated patterns and green symbols correspond to the positions of Bragg peaks.

Notes for structure analysis:

We refined models of the low- and high-temperature phases using TOPAS-Academic v.7. In the low-temperature phase, we refined a model based on the reported structure in space group $P2_1/a$. The decylammonium ion was modelled as a rigid body in which all C-C bond lengths and C-C-C bond angles were refined, while the C-C-C-C torsion

angles refined freely. H atoms were placed by geometry. The positions of the Cl atoms were restrained so that the Mn-Cl bond lengths had approximately their reported values of 2.485 and 2.584 A and the Cl-Mn-Cl angles were approximately 90%. The Mn atom sits on the center of symmetry at the origin and has no translational degrees of freedom. Isotropic atomic displacement parameters (ADPs) were refined for all atoms, with the Cl atoms and, separately, the C and N atoms constrained to have the same value. A spherical harmonic correction for preferred orientation was used, refining terms up to eighth order. This gave good agreement with the experimental data [Figure A2 (b)].

To our knowledge, no structural model of the high-temperature phase has previously been reported. Since the transition is first-order, the space group of this phase is not required to be a supergroup of that of the low-temperature phase. However, for simplicity, and by analogy with the related Cd-containing material, we began by considering possible space groups among the minimal supergroups of $P2_1/a$. These can be divided into two categories: the translationengleiche supergroups, which have orthorhombic symmetry; and the klassengleiche supergroups, which have a new translational symmetry element.

Considering the first possibility, we searched for a possible orthorhombic cell, using simulated annealing to refine the cell parameters in a Pawley fit. It quickly became clear that the experimental pattern could not be reproduced by an orthorhombic cell with the same volume, ruling out the possibility of describing it in a translationengleiche supergroup. On the other hand, a monoclinic cell described it well.

Turning to the second possibility, the obvious potential new translational symmetry element is along the vector (1/2, 1/2, 0), connecting the two Mn atoms. This is easily

described by a C-centered cell. There are now only two possible space groups, *C*2/*m* and *C*2/*c*. By inspection, of these only *C*2/*m* is compatible with the observed structure (with cell vectors remaining the same as $P2_1/a$).

As a final alternative, we also considered a non-supergroup structure in *Pbca*, in which the unit cell doubles along the c axis. This structure occurs in the Pb analogue of this material. Considering only the peak positions in a Pawley fit showed that this is indeed a plausible unit cell. However, in Rietveld refinement the structural model gave very poor agreement with the data. We did not, therefore, pursue it further.

We concluded therefore that the best description of these data is given by a *C*2/*m* model. In this space group, the Mn and one Cl atom must sit on special positions, and have no translational degrees of freedom in Rietveld refinement. The other Cl atom and the decylammonium ion sit on, or are disordered about, the mirror plane. QENS measurements suggest that the dominant conformation in the HT phase is TTTTGTG'T, where each letter represents a torsion angle along the N-C10 chain: T for a trans conformation, G and G' for gauche conformations with opposite torsion angles. Accordingly, we modelled the decylammonium ion as a rigid body with ideal 180o and 60o torsion angles, this time also fixing the bond lengths and angles. The N atom and free Cl atom were fixed on the plane, while all other atoms were modelled as split sites above and below the plane. Isotropic ADPs were refined for all atoms, with those of N and all C atoms constrained to be the same. Again, H atoms were placed by geometry, and a spherical harmonic correction for preferred orientation was used, refining terms up to eighth order. This model gave excellent agreement with the data.

As a check, we also considered the low-temperature conformation TGTTTTTT and the all-trans possibility TTTTTTTT. These gave poorer fits to the data, although they were individually plausible, indicating the limited sensitivity of powder X-ray diffraction data to the precise conformation of the alkyl chains. For this reason, we made no attempt to model any conformational disorder. However, the rather large ADPs suggest that a more sophisticated disorder model might be preferable if more data were available: for instance, from single-crystal measurements.

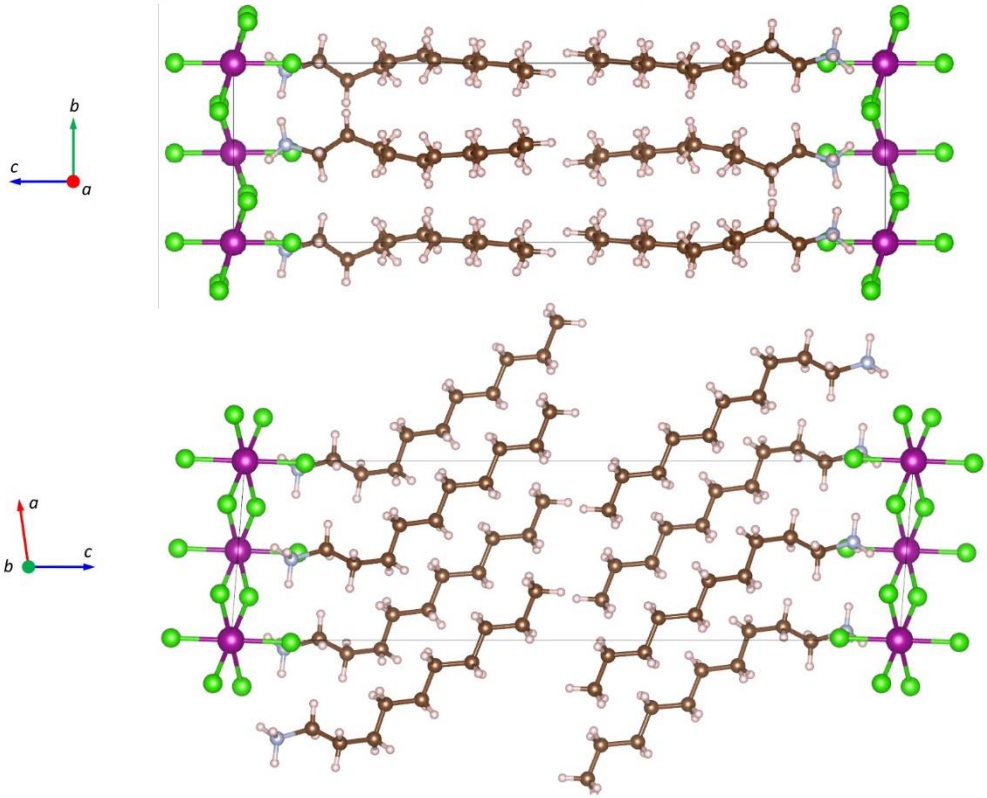

Figure A3. Unit cell structure of the low-temperature phase $P2_1/a$ projected on the (100) and (010). Purple, green, grey, brown and white spheres stand for Cl, Mn, N, C and H atoms.

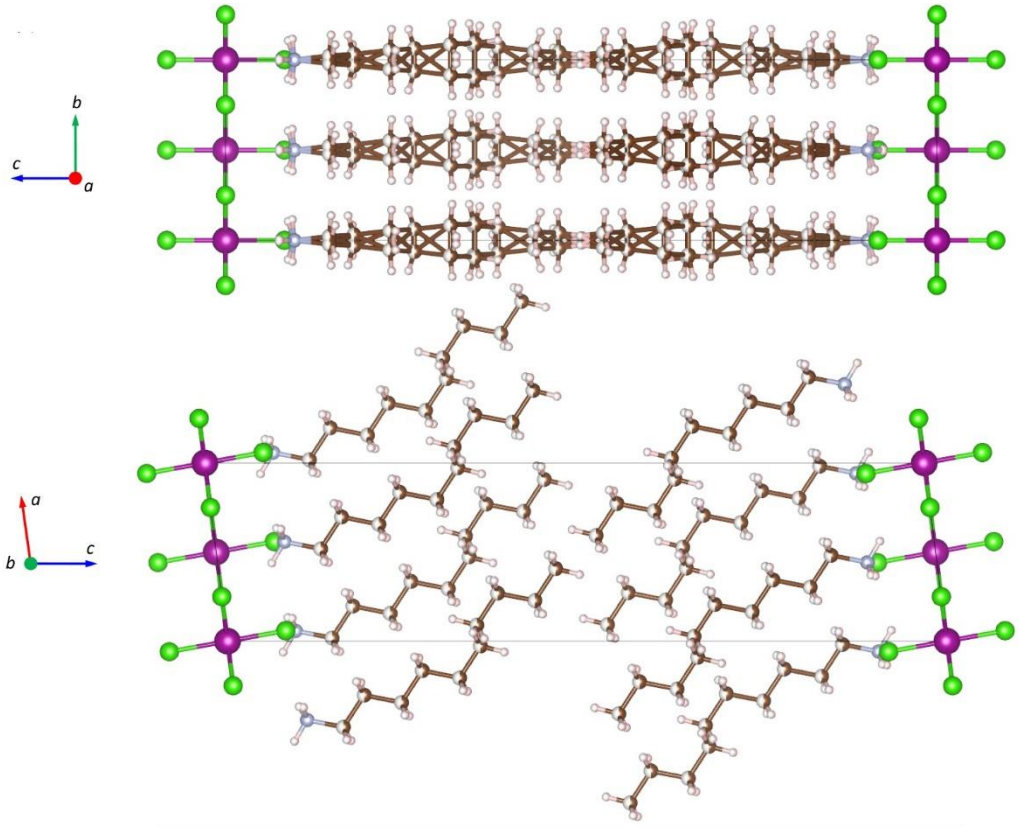

Figure A4. Unit cell structure of the high-temperature phase *C*2/*m* projected on the (100) and (010) planes. Purple, green, grey, brown and white spheres stand for Cl, Mn, N, C and H atoms. In the *C*2/*m* phase, half-filled brown spheres stand for disordered C atoms with half occupation.

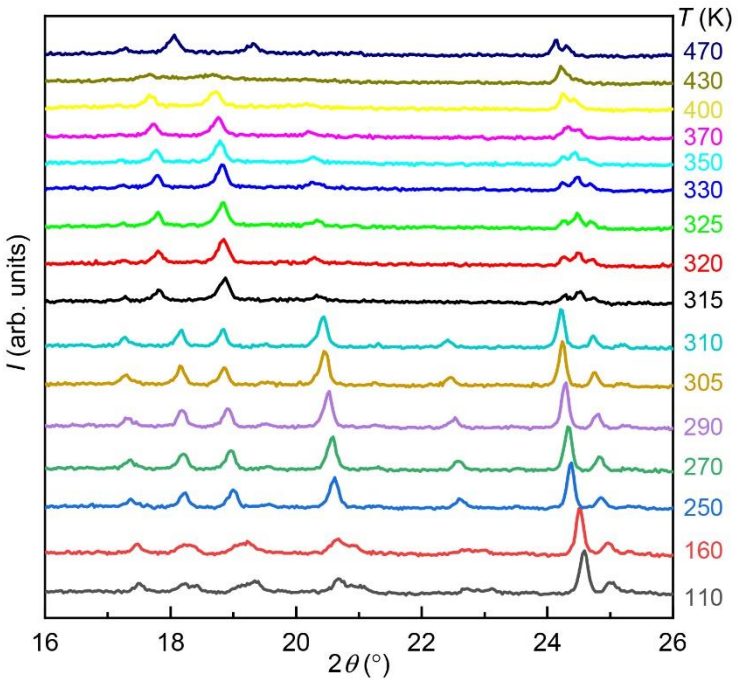

Figure A5. Temperature evolution of X-ray powder diffraction patterns recorded across the phase transition for $(C_{10}H_{21}NH_3)_2MnCl_4$.

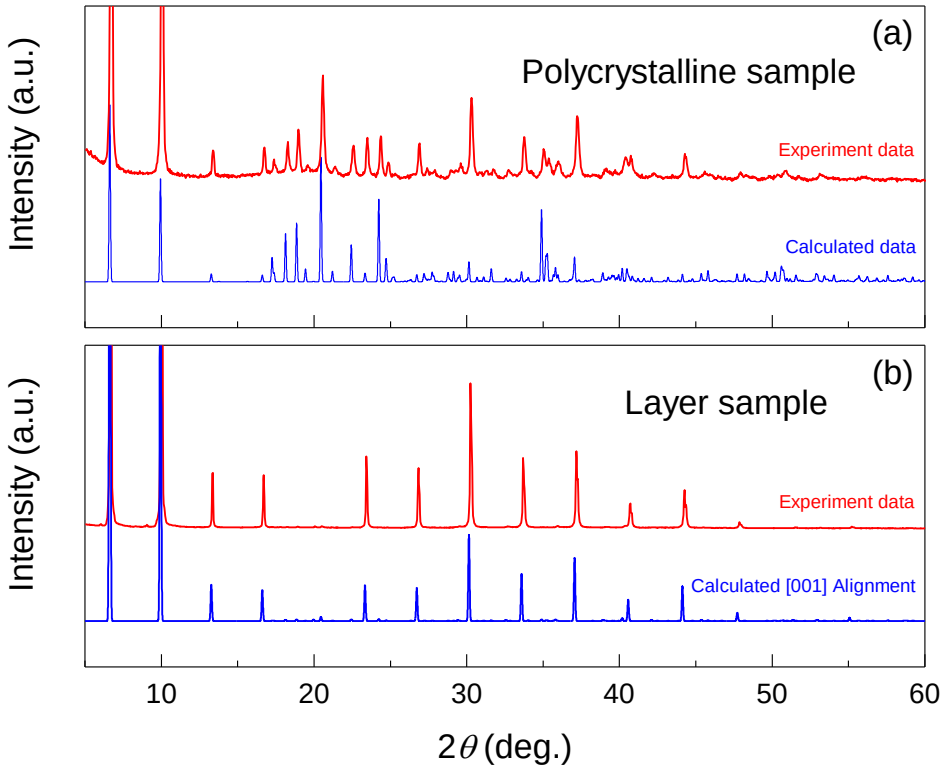

Figure A6. X-ray powder diffraction data for polycrystalline powder sample and highly layered sample. Data in blue colour are calculated data from crystal structure.

Appendix B

High-pressure calorimeters A and B signals

High-pressure experiments were performed in Departament de Física i Enginyeria Nuclear at Universitat Politècnica de Catalunya under the supervision of Dr. Pol Llovereas. I collected, analysed and plotted all the related data with the help of Dr. Pol Lloveras.

Figure B1-B2: High-pressure calorimetric signals of C_{60}.

Figure B3-B4: High-pressure calorimetric signals of $(C_{10}H_{21}NH_3)_2MnCl_4$.

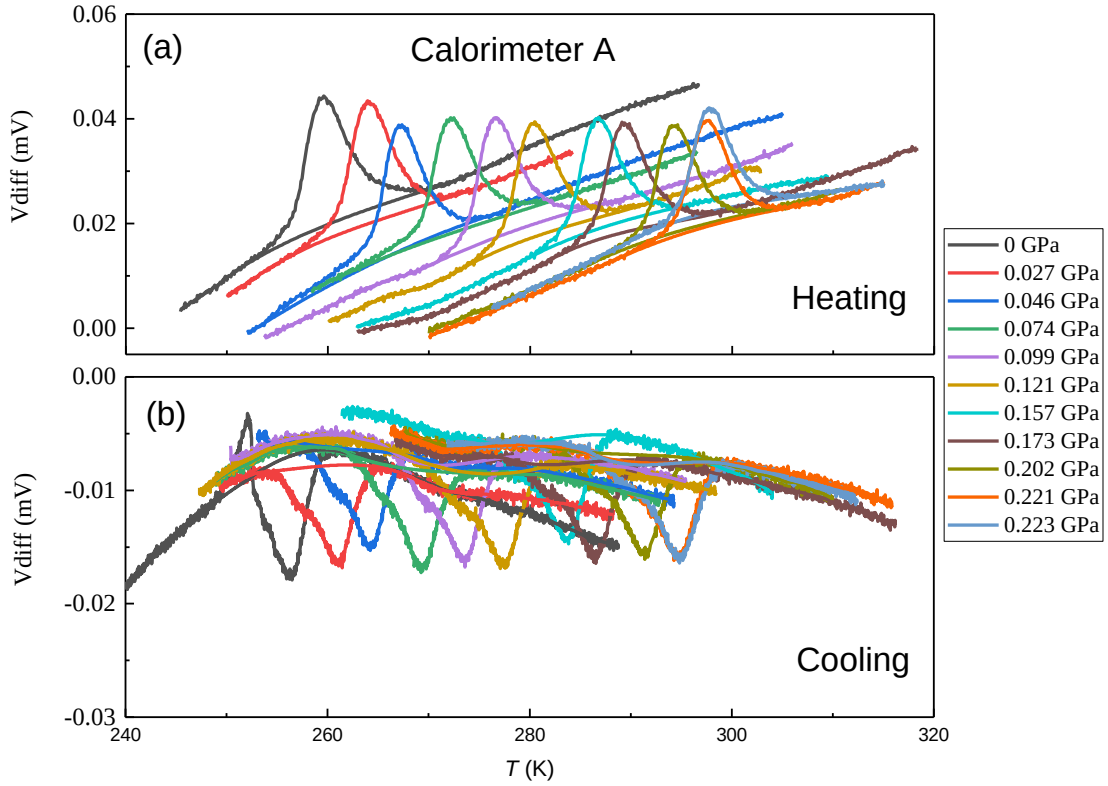

Figure B1. Heat flow data of C_{60} under pressure. Calorimeter A: The calorimetric signals, V_{diff} in temperature with baseline fitted. (a) heating and (b) cooling.

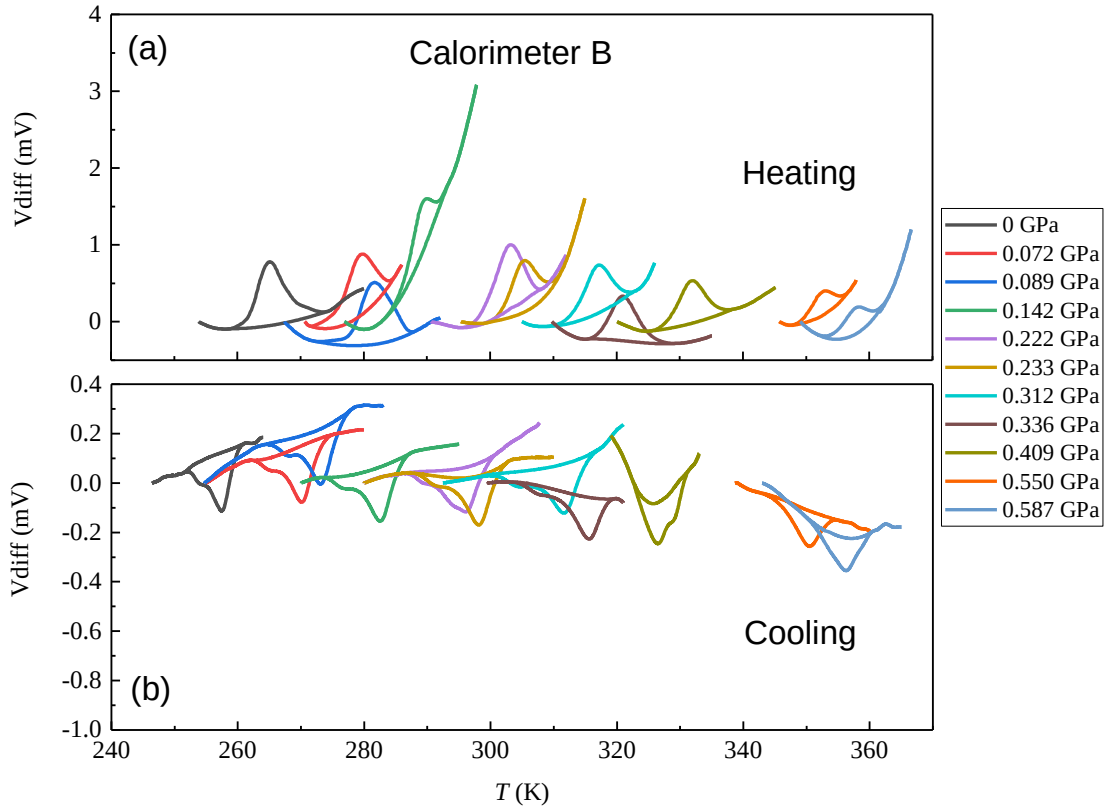

Figure B2. Heat flow data of C_{60} under pressure. Calorimeter B: The calorimetric signals, V_{diff} in temperature with baseline fitted. (a) heating and (b) cooling.

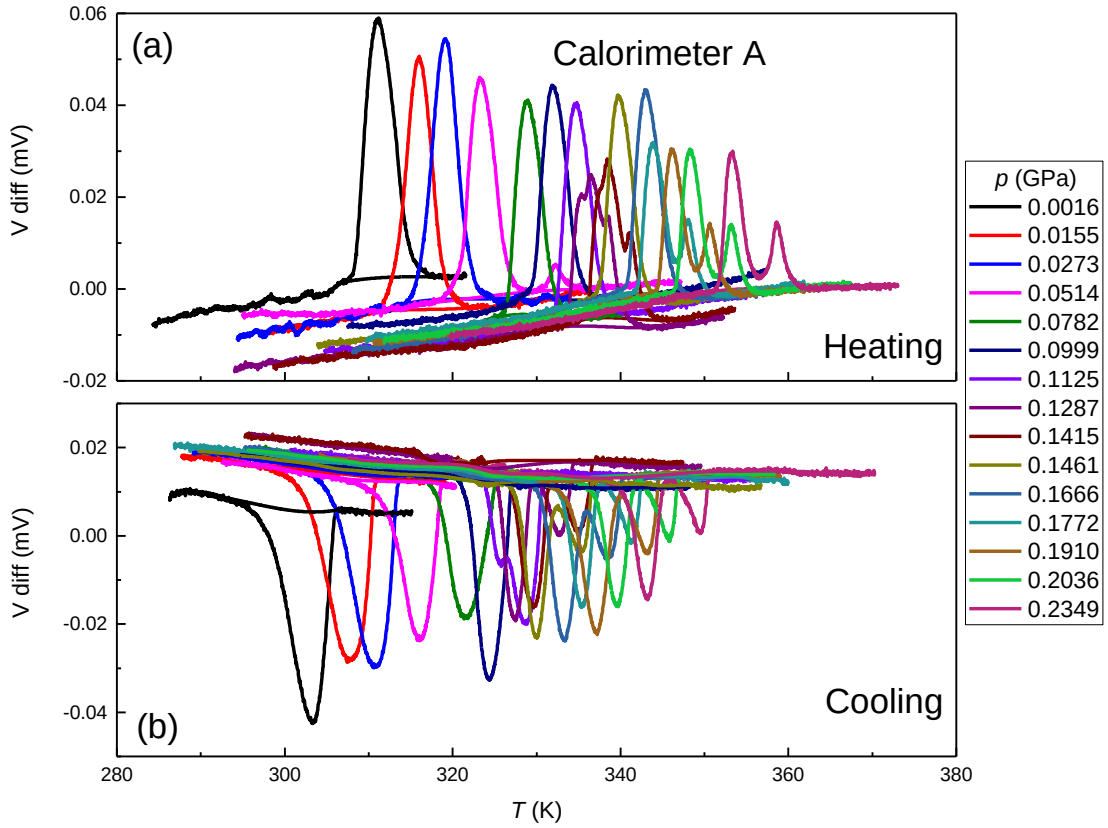

Figure B3. Heat flow data of $(C_{10}H_{21}NH_3)_2MnCl_4$ under pressure. Calorimeter A: The calorimetric signals, V_{diff} in temperature with baseline fitted. (a) heating and (b) cooling.

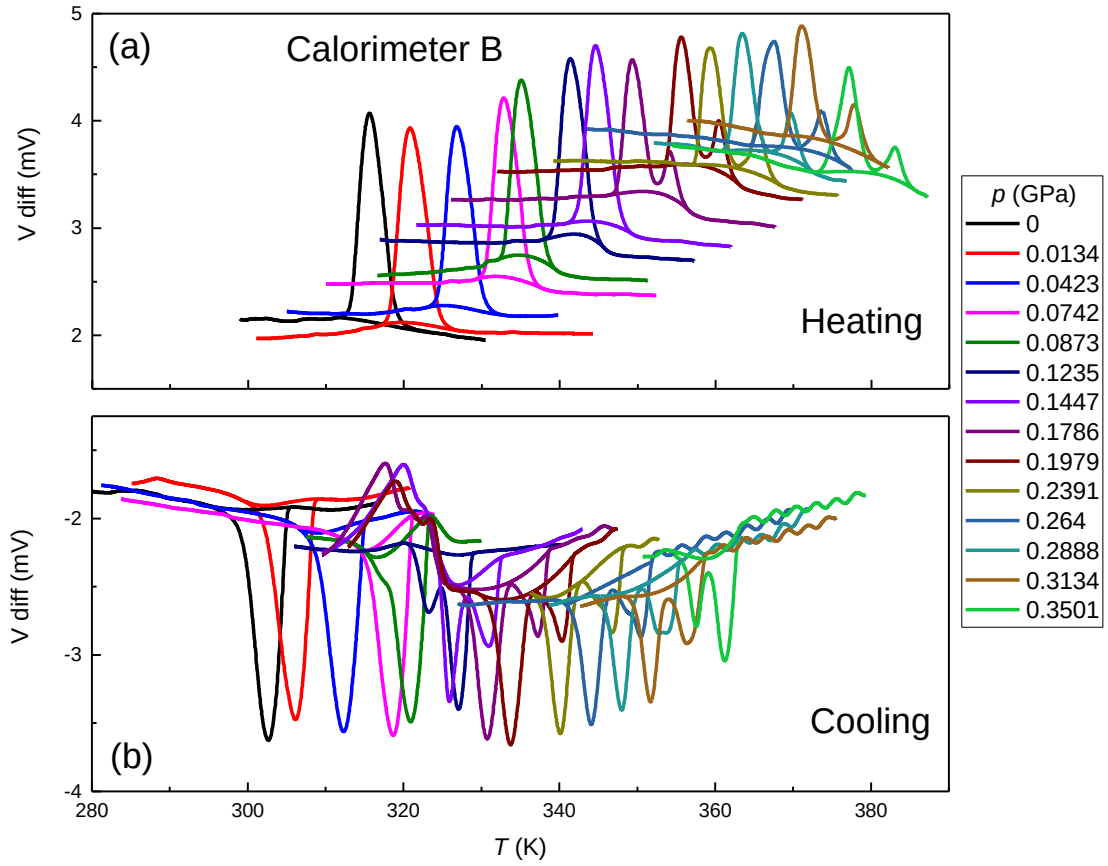

Figure B4. Heat flow data of $(C_{10}H_{21}NH_3)_2MnCl_4$ under pressure. Calorimeter B: The calorimetric signals, V_{diff} in temperature with baseline fitted. (a) heating and (b) cooling.